Doctoral Thesis

Analytic and Machine Learning Based Design of Monolithic Transistor-Antenna for Plasmonic Millimeter-Wave Detectors

Ramesh Patel

Department of Electrical Engineering

Graduate School of UNIST

2020

Analytic and Machine Learning Based Design of Monolithic Transistor-Antenna for Plasmonic Millimeter-Wave Detectors

Ramesh Patel

Department of Electrical Engineering

Graduate School of UNIST

Analytic and Machine Learning Based Design of Monolithic Transistor-Antenna for Plasmonic Millimeter-Wave Detectors

A thesis/dissertation submitted
to the Graduate School of UNIST
in partial fulfillment of the requirements
for the degree of Doctor of Philosophy

Ramesh Patel

12. 04. 2019

Approved by

Advisor

Kyung Rok Kim

Analytic and Machine Learning Based Design of Monolithic Transistor-Antenna for Plasmonic Millimeter-Wave Detectors

Ramesh Patel

This certifies that the thesis of Ramesh Patel is approved.

12. 04. 2019

signature

Advisor: Kyung Rok Kim

signature

EunMi Choi: Thesis Committee Member #1

signature

Jingook Kim: Thesis Committee Member #2

signature

Gangil Byun: Thesis Committee Member #3

signature

Ki Jin Han: Thesis Committee Member #4

Abstract

This thesis reports an advanced analysis on a monolithic transistor-antenna by designing a ring-type asymmetric FET itself as a receiving antenna element which receives millimeter-waves in a loss-less manner with a plasmonic amplification for millimeter-wave (mmW) detectors. The proposed transistor-antenna device combines the plasmonic and the electromagnetic (EM) aspects in a single place. As a result, it can absorb the incoming mmW and transfer power directly to the ring-type asymmetric channel without any feeding line and separate antenna element. Both the charge asymmetry in device channel and the antenna coupling are contributing to the enhanced photoresponse. Among the two factors, the improved antenna coupling is more dominant in the performance enhancement of our proposed design. Also, our transistor-antenna device have enhanced performance with uniformly enhanced responsivity of every pixel by characterizing its impedance exactly pursuing real-time mmW imaging. Operation principle of the proposed device is discussed, focusing on how signal transmission through the ring-type structure is available without any feeding line between the antenna and the detector. To determine the antenna geometry aiming for a desired resonant frequency, we present an efficient design procedure based on periodic bandgap analysis combined with parametric electromagnetic simulations. From a fabricated ring-type FET-based monolithic antenna device, we demonstrated the highly enhanced optical responsivity and the reduced optical noise-equivalent power, which are in comparable order with the reported state-of-the-art CMOS-based antenna integrated direct detectors.

Another part of the thesis focuses on developing machine learning models to enable fast, accurate design and verification of electromagnetic structures. We proposed a novel Bayesian learning algorithm named as Bayesian clique learning, for searching the optimal electromagnetic design parameter by using the structural property of EM simulation data set. Along with this, we also given an inverse problem approach for designing the electromagnetic structures which suggests going in the opposite direction to determine the design parameters from characteristics of the desired output.

Acknowledgements

I would like to express my gratefulness to all who contributed ideas, encouragement and support. I would like to thank, firstly Mata Rani for giving me grace and wisdom.

I would like to convey my deep sense of gratitude to my supervisors, Prof. Kyung Rok Kim, Associate Professor, School of Electrical and Computer Engineering, Ulsan National Institute of Science and Technology (UNIST), South Korea, and Prof. Ki Jin Han, Associate Professor, Division of Electronics and Electrical Engineering, Dongguk University, Seoul, Korea. Their continuous support and motivation at every stage of my research encouraged me to give my best efforts. Their vast experience on antennas and semiconductor device physics helped me to resolve practical issues and design optimized systems. Apart from knowledgeable guide they are a person with humble and kind heart. They have always encouraged me for quality research work with innovation.

It is pleasure to thank, Prof. Eunmi Choi, Prof. Jingook Kim, Prof. Gangil Byun, and Prof. Franklin Bien for their efforts to build my base of Electromagnetics and Millimeter-Wave measurements and also expand my horizon of knowledge during entire stay in UNIST. I wish to express my sincere gratitude to Prof. Kallol Roy, Assistant Professor, Institute of Computer Science, University of Tartu, Estonia, Dr. Min Woo Ryu, Dr. Jagannath Malik, and Dr. Ashwini Sawant for the immeasurable discussions on solving my Ph.D. problem and also for their valuable discussions and feedback.

I want to thank all my colleagues in Nano-Electronic Emerging Devices (NEEDs) Lab., in UNIST for their warm hospitality and providing me a very co-operative ambience, in which, completing my work was a privilege and pleasure. I would also thank Dr. Mun Seok Choe, Mr. E-San Jang, Mr. Sang Hyo Ahn, Mr. Jong Yul Park, Mr. Sung Ho Kim, Mr. Jae Won Jung, Ms. Youngeun Choi, and Mr. Woo-Seok Kim for their immense help and support during experimental work. My best thanks go to my friends Mr. Ritesh Soni, Mr. Amitosh Sharma, Mr. Abhishek Meena, Dr. Tanya Kumari, Ms. Neha Rana, and Mr. Pamul Yadav with whom I spent most of time during my Ph.D. Their valuable support and time for guidance in technical issues, which was instrumental in making this dissertation work a

success. I would also like to show gratitude to Ms. Smita Biswas and Ryan for providing a family environment for me whenever I was missing my family.

I would like to extend my deepest gratitude to Prof. M.V. Kartikeyan, IIT Roorkee, India for his belief in me and his support to understand my caliber and help me to achieve the opportunity to complete my Ph.D. program in UNIST.

My very special thanks go to my parents, grand-parents, uncle and aunts for their never losing trust and confidence on me, even in my tough time and become source of inspiration. To my sisters Mrs. Alka and Ms. Manisha, cousins Mr. Piyush, Mr. Abhishek, Mr. Vaibhav, and Mr. Sourabh, brother-in-law Mr. Akhilesh, thank you for always being there for me and bringing joy to my life.

I owe thanks to a very special person, my wife, Mrs. Shilpa Chandrol for her eternal love, and constant understanding during my pursuit of Ph.D degree. I think of myself blessed to have such a lovely and caring wife, standing beside me with her affection and unconditional support.

12.04.2019

Ramesh Patel

To my parents.

Contents

Abstract i

Acknowledgements ii

List of Tables vii

List of Figures viii

1 Introduction **1**

1.1 Problem statement 2

1.2 Motivation and scope 4

1.3 Thesis outline 6

2 Theoretical background **7**

2.1 Principle of performance enhancement 8

2.1.1 Impedance matching at interface 9

2.2 Resonance frequency 10

2.2.1 2-D periodic array model to initialize the interval of resonance frequencies 11

2.3 Influence of substrate thickness and its modes 14

2.4 Available power on transistor-antenna 17

2.4.1 Calculation of element detector pixel gain 19

3 Monolithic transistor-antenna design **21**

3.1 Monolithic circular transistor-antenna device 21

3.1.1 Structure 21

3.2 Design and characterization 22

3.2.1 Electromagnetic simulation setup 23

3.2.2 Design procedure 24
3.3 Results and discussion 30
3.3.1 Reflection and transmission results 30
3.3.2 Experimental electric field analysis 31
3.3.3 Radiation pattern and gain 35
3.3.4 Available power on element detector 36
3.3.5 Experimental results of mmW detector 38
3.3.6 Bandwidth of complete detector response 41
3.3.7 Comparison among state-of-the-art antenna integrated direct detectors 42

4 EM structure design with machine learning 44
4.1 EM structure design through Bayesian Learning 44
4.1.1 Proposed method 45
4.1.2 Computational complexity 49
4.1.3 Results and discussions 50
4.2 Inverse design of EM structure with deep learning 51
4.2.1 Prior work on inverse design 53
4.2.2 Theoretical setting of inverse problem 58
4.2.3 Artificial general intelligence as multi-tasking 60
4.2.4 Proposed method for inverse design 62
4.3 Inverse design of transistor-antenna through Deep Learning 66

5 Conclusion and future work 71
5.1 Conclusion 71
5.2 Future Work 72
5.2.1 Monolithic transistor-antenna design for real-time THz colour imaging 72
5.2.2 Inverse design for small dataset 73

References 74

List of publications 84

List of Tables

3.1 Antenna geometry parameters 30
3.2 Detector performance @ 120 GHz 41
3.3 Detector performance excluding amplifiers 43

4.1 System performance parameters for inverse design 65

List of Figures

1.1 The electromagnetic wave spectrum. 2

1.2 (a) Conventional FET and an antenna structure on separate semiconductor chips or integrated on a single chip (b) Proposed monolithic circular transistor-antenna structure. 4

2.1 Schematic of mmW detection based on FET in non-resonant regime. 8

2.2 (a) Bar-type structure [43] (b) Ring-type structure having asymmetry ratio η_a by keeping l in the asymmetric channel. 9

2.3 Equivalent circuit model of the monolithic circular transistor-antenna structure. 10

2.5 Plot of the normalized frequency $f \times a/c$ versus normalized wave number for the first three TM propagating modes in air and silicon medium when $r/a = 0.14$. The cases correspond to a wave propagation in the z-direction with $k_x = k_y = 0$ through the square lattice. 14

2.8 Free-space experiment setup with extender and horn antenna. 17

2.9 Schematic experiment setup for power estimation with horn antenna and detector. 18

3.1 Conceptual schematic of the proposed monolithic circular antenna structure based on ring-type asymmetric FET. 22

3.2 (a) Top view of ring-type FET-based monolithic circular antenna with $d_S = 30$ μm, $d_G = 98.4$ μm, $d_D = 280$ μm, and $a = 1000$ μm. (b) Side view of ring-type FET-based monolithic circular antenna. 23

3.3 Unit cell simulation setup in HFSS: Periodic boundary condition is applied for all lateral faces and Floquet port is set at top and bottom faces. 24

3.4 Simulated E-field distribution on the surface of transistor-antenna. 25
3.5 Simulated reflection coefficient with and without DC and ground lines. . . . 26
3.6 Plot of the normalized frequency $f \times a/c$ versus normalized wave number for the first three TM propagating modes in air and silicon medium when $r/a = 0.14$. The cases correspond to a wave propagation in the z-direction with $k_x = k_y = 0$ through the square lattice. 27
3.7 Parametric variation of simulated reflection coefficient with respect to $d_D/2a$ and t_{Si} to identify the dominant factors for resonance frequency of ring-type FET-based monolithic circular antenna. 28
3.8 Parametric variation of simulated reflection coefficient and absorptance with respect to different substrate material [ϵ_r = 11.9 (Si), ϵ_r=12.5 (InP), ϵ_r=16.2 (Ge)]. 29
3.9 (a) The measurement setup for obtaining the s-parameter of designed ring-type FET-based monolithic circular antenna by using quasi-optical system with Gaussian beam radius of 8 mm. (b) Sample of 20×20 array and (c) ring-type FET-based monolithic circular antenna. 31
3.10 Measurement and simulation results of (a) reflection coefficient ($|S_{11}|$), (b) transmission coefficient ($|S_{21}|$), and (c) absorptance ($1 - |S_{11}|^2 - |S_{21}|^2$). . . 32
3.11 Simulated impedance parameters. 33
3.12 Measurement setup for obtaining E-field intensity. 33
3.13 Measured 2-D intensity profile of the 120 GHz beam for $z = 0.5$ cm position in the propagation direction of the incident wave (a) Magnitude (b) Phase . 34
3.14 Measurement of normalized 1-D intensity profile of the mmW beam for $z =$ 0.25 cm position in propagation direction of the incident wave, scanned in two axes for two different incident polarizations (a) Scanning in X-axis (b) Scanning in Y-axis 35
3.15 Normalized E-field of the mmW beam measured at $z = 0.25$cm with and without the transistor-antenna device in the propagation direction of the incident wave. 36
3.17 Element detector pixel antenna gain. 37

3.18 Contour plots of (a) beam profile and (b) beam width as 2×beam radius (r_{beam} = 12.6 mm @ z= 100 mm) with analytic equation (Eq. 2.16). 38

3.19 Measurement setup for ring-type FET-based monolithic circular antenna at 120 GHz system with a chopping frequency (f_{chop}) of 2 kHz. 39

3.20 Measured data for ring-type FET-based monolithic circular antenna device and bar-type detector at 120 GHz and f_{chop}. (a) Photoresponse Δu (b) Responsivity $R_v = \Delta u/P_a$, where P_a = 42.4 nW for the ring-type FET-based monolithic circular antenna device and P_a = 25 nW for the reference bar-type detector. (c) NEP = N/R_v, where N is the total noise of the detector. The Exp. plot is made with the measured N while the Cal. plots are made with the calculated N under the thermal noise assumption. 40

3.21 Measured photoresponse Δu and normalized responsivity R_v of the detector over the operation frequency band. 42

4.1 A schematic diagram of $n \times n$ MTM prototypes with notations a = b = x_i^1, c = x_i^2, $g_x = g_y = x_i^3$, w = x_i^4 for $i = N$ number of input dataset, (a) EM structure I (b) EM structure II, x varies with a by taking fixed t value between two rings. 46

4.2 Electromagnetic design complex 48

4.3 For f_r of EM structure I (a) MSE for high f_r range (b) M.L. o/p and simulated results for topmost samples (x_i^L). 51
4.4 For f_r of EM structure I (a) MSE for mid f_r range (b) M.L. o/p and simulated results for topmost samples (x_i^L). 52
4.5 For f_r of EM structure I (a) MSE for low f_r range (b) M.L. o/p and simulated results for topmost samples (x_i^L). 52
4.6 For μ_{eff} of EM structure I (a) MSE for high μ_{eff} range (b) M.L. o/p and simulated results for topmost samples (x_i^L), $f_r = 10$ GHz. 53
4.7 For μ_{eff} of EM structure I (a) MSE for mid μ_{eff} range (b) M.L. o/p and simulated results for topmost samples (x_i^L), $f_r = 10$ GHz. 53
4.8 For μ_{eff} of EM structure I (a) MSE for low μ_{eff} range (b) M.L. o/p and simulated results for topmost samples (x_i^L), $f_r = 10$ GHz. 54
4.9 For f_r of EM structure II (a) MSE for high f_r range (b) M.L. o/p and simulated results for topmost samples (x_i^L). 54
4.10 Correlation between two EM structures. 55
4.11 Searching in high dimensional geometry space. 55
4.12 Neural ordinary differential equation (ODE). 56
4.13 Sparse neural network for inverse design. 57
4.14 Network Tikhonov. 58
4.15 Network Tikhonov encoder-decoder. 59
4.16 Generative adversarial networks (GANs) for inverse design. 59
4.17 Multitasking neural network. 60
4.18 Agent-environment framework. 61
4.19 A schematic diagram of $n \times n$ MTM prototype with notations (a) structure length $a = b$ (b) gap width c (c) substrate length $g_x = g_y$ (d) line thickness w 63
4.20 Multi-tasking neural network for inverse design. 64
4.21 Expectation-Maximisation algorithm for inverse design. 64

4.22 Histogram training geometry parameter plots of $n \times n$ metamaterial prototype structure. (a) structure length a (b) gap width c (c) substrate length g_x (d) line thickness w. 66

4.23 Experimental and predicted transmission spectra results of inverse design for $n \times n$ metamaterial prototype structure. (a) structure length a (b) gap width c (c) substrate length g_x (d) line thickness w. 67

4.24 Unit cell transistor-antenna structure (a) Top view (b) Side view. 68

4.25 Histogram training geometry parameter plots of $n \times n$ transistor-antenna structure. (a) substrate relative permittivity ϵ_r (b) dielectric thickness t_{Si} (c) drain radius r_{dr}. 69

4.26 Experimental and predicted absorptance spectra results of inverse design for $n \times n$ transistor-antenna structure. (a) substrate relative permittivity ϵ_r (b) dielectric thickness t_{Si} (c) drain radius r_{dr}. 70

Chapter 1

Introduction

Millimeter wave (mmW) frequency range, located from 30 GHz to 300 GHz in the electromagnetic (EM) spectrum as shown in Fig. 1.1, has become of large interest over the last years since nonionizing mmW rays provide considerable advantages compared to infrared radiation and microwaves in imaging applications, mainly with the capability of better permeability, less scattering in air, and the availability of higher power devices [1–3]. Technology in this frequency range is extremely attractive research field in semiconductor security inspection, biomedical, and atmosphere limb sounding applications [4–11]. However, due to its non-ionizing nature unlike that for X-rays, it has much of interest in biosensing and security imaging applications. Recently, a lot of works have been reported on the THz imaging, which is being commercialized in the near future. In particular, interstellar dusts and molecular line emissions from non-metallic materials, radiated energy in the form of mmW range wavelength, thus there is a need to explore detectors in mmW range [1]. To facilitate the mmW imaging technology in upcoming applications, development of a breakthrough solid-state technology for fast and room-temperature detectors integrated in high-speed multi-pixel arrays is highly desired. While traditional approaches such as superconducting hot-electron bolometric systems [12], [13], pyroelectric detectors [14], and pneumatic sensors [15], are limited in their applications due to cost and speed issues, solid-state devices such as high-electron-mobility transistors (HEMT) [16], hetrojunction bipolar transistors (HBT) [17–21], field effect transistors (FET) [22], and CMOS architectures [23–32], have

exhibited record detectivities in gigahertz range. These solid-state-based technologies are also advantageous when being scaled to a large array.

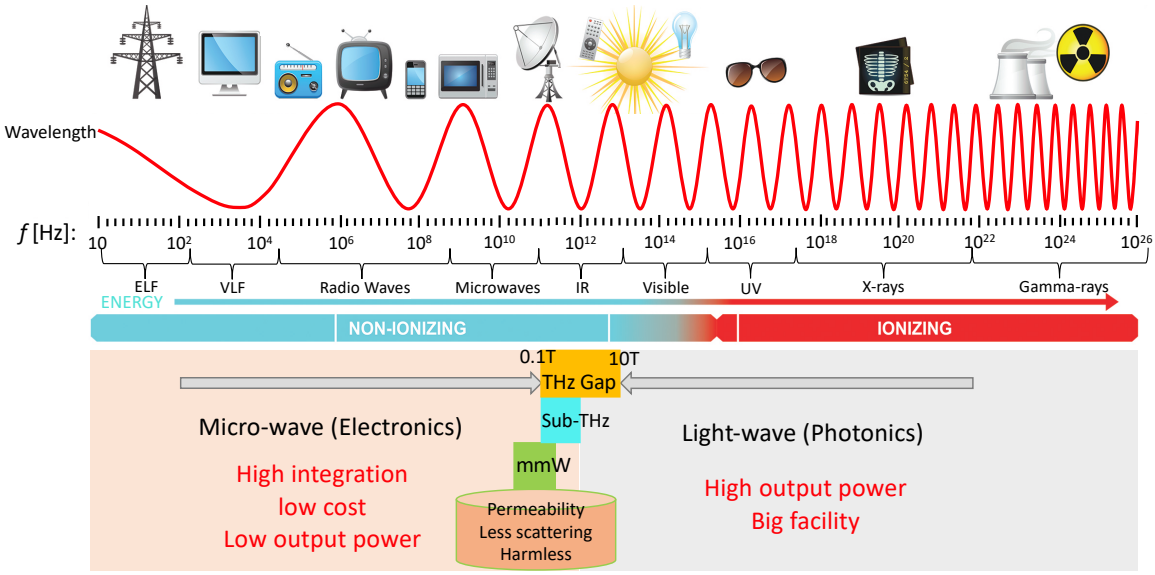

Figure 1.1: The electromagnetic wave spectrum.

1.1 Problem statement

Recently, a number of studies have been reported on the antenna integrated direct detectors based on plasmonic power detection mechanism, which is not limited by the cut-off frequency as in the transit mode. It exhibits enhanced responsivity according to the increase of mmW frequency [33], and robustness to high input mmW power [34]. For conventional CMOS-based devices to detect millimeter-waves, all the reported plasmonic detectors inevitably have been integrated with relatively large-size antennas considering quarter- or half-wavelength of mmW range [23–26, 35–39]. In the absence of an antenna, the amount of mmW radiation coupled to the device channel is probably very small therefore enhanced photoresponse (Δu) can be obtained by adding proper antenna. Moreover, smaller CMOS-based device is preferable because of its high input impedance for better photoresponse [30], which needs device size to be optimally chosen in view of feasible antenna design. And, the width of feeding line should become smaller for higher impedance, which results in performance variation by narrow margin of process tolerance. This causes significant power

loss during transmission through feeding line, depending on the antenna design [30, 40, 41]. This is an important observation that tells us that despite the enhanced responsivity (R_v), the overall detector performance may be degraded because of difficulties in matching the antenna and feeding line impedance. Also, the antenna pattern and gain dependence on the detector position on the finite substrate varies the individual pixel R_v and noise-equivalent power (NEP) values of multi-pixel detectors [42].

In addition, every MOSFET device in detector array has different input impedance because it is difficult to realize same channel doping concentration in every MOSFET pixel on same wafer. Therefore, it is difficult to design antenna and feeding line with the input impedance corresponding to every MOSFET device pixel. Hence, the conversion of incident mmW power through antenna and feeding line have different detector performance for every pixel which results reduced overall performance of multi-pixel detector [43, 44].

For a 'camera-chip-level' imaging systems based on unit and multi-pixel operation, a number of works have been reported. A plasma mode sub-THz detector based on asymmetric FET design with integrated antenna for unit-pixel operation [44, 45] and a broadband imager for multipixel operation have been proposed [36, 46]. With different detection mechanism such as transit-mode, a schottky barrier diode (SBD) imager with raster scan measurement [25, 26] and InGaAs SBD imager as a real-time 1-D line scanner [35], were demonstrated. In terms of the circuit design approach, a resistive mixer-based THz detector has been proposed [36]. By utilizing distributed resistive self-mixing in the FET channel, a focal plane array detector integrated with differential amplifiers was reported [39], and recently, a 1 k-pixel video camera with antenna and amplifier for a real-time high-resolution imaging has been reported [23, 25, 29].

However, the relatively low detection performance by power loss in transistor and antenna requires high-gain amplifiers, which constraints the number of pixels. Furthermore, high-gain amplifiers, which are widely adopted due to their small output signal by input power loss, can also increase the total detector noise by additional circuitry and constraints the number of pixels for multi-pixel operation. Therefore, a careful MOSFET device design considering its input impedance and matching of the antenna is one of the most impor-

tance issues in high-performance plasmonic mmW detectors based on antenna integrated MOSFET [43].

1.2 Motivation and scope

To increase the response of plasmonic mmW detectors, antenna element design is important to maintain the required response level under any situation. For example, polarization-sensitive characteristic is not desirable for mmW detection applications. Although the polarization-sensitive antennas enable a highly efficient photoresponse, they should be carefully controlled under the variation of incident angle and fabrication variability [47–49]. In addition, careful design of feeding lines between the antenna and the FET is important since impedance mismatch and loss through the interconnection should be minimized [50–53]. To reduce the mismatching and losses, antennas and detectors can be integrated into a

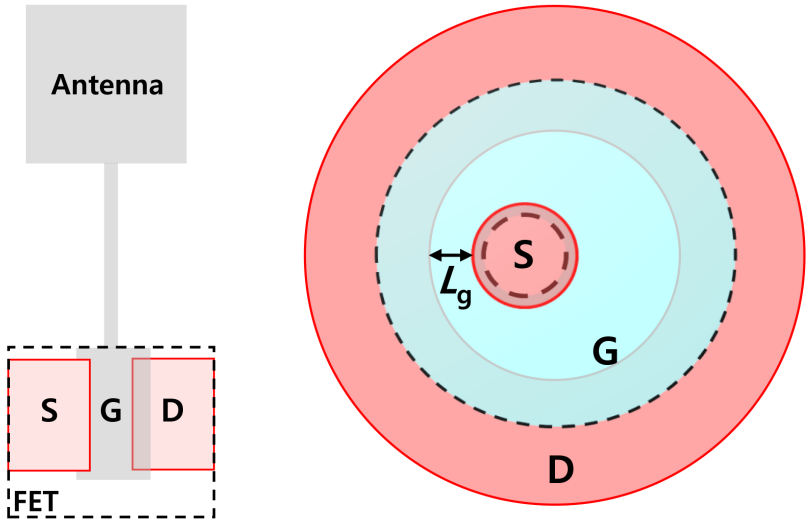

Figure 1.2: (a) Conventional FET and an antenna structure on separate semiconductor chips or integrated on a single chip (b) Proposed monolithic circular transistor-antenna structure.

single semiconductor chip, which facilitates the design of highly compact systems utilizing several antenna elements [37, 38, 45, 54–58]. By placing the antennas adjacent to the radio front-end on a single chip or packaging, the integrated system offers improved per-

formances [29, 30], [40, 59]. In the recent trend of integrated designs, we have developed plasmonic mmW detectors based on the asymmetric FETs [43], presented a non-self-aligned structure and low-impedance FET design considering impedance matching with an in-plane integrated antenna. In [44], a self-aligned poly-Si gate structure with a vertically integrated patch antenna on top metal layer have been presented. Although the asymmetric boundary condition contributed to the improved photoresponse, the entire performance of the asymmetric FET-based detectors was limited by imperfect matching between the device and the antenna through high-impedance feeding lines.

To resolve the limitations in the previous asymmetric FET based designs and realize a high-performance multi-pixel plasmonic mmW detector, we propose a novel monolithic circular transistor-antenna in this thesis. By designing the ring-type asymmetric FET itself as a circular patch antenna as shown in Fig. 1.2(b), we can extract ac power from impinging millimeter waves without extra feeding and interconnect network [60]. As compared with a conventional bar-type approach (in Fig. 1.2(a)), our monolithic circular antenna device combines plasmonic and electromagnetic aspects within the same structure. As a result, it can absorb the incoming mmW and transfer power directly to the ring-type asymmetric channel without any feeding line and separate antenna element. Our proposed structure is compact and provides broad bandwidth and high data rate by reduced feeding losses. When designing integrated multi-pixel detectors, the proposed transistor-antenna relieves the difficulty of matching under the impedance variation of many devices. In the antenna aspect, the proposed circular antenna structure is not selective for the polarization state of incident wave. Also, the radiation pattern and gain variations of the individual pixel by the detector positions on the finite substrate can be eliminated [42].

Therefore it can be a promising candidate for multi-pixel detector with uniformly enhanced responsivity by characterizing its impedance exactly pursuing real-time THz imaging.

1.3 Thesis outline

In this chapter, the thesis introduces mmW technology focused on mmW imaging technology and then describes the issues of antennas and its integrated direct detectors.

Chapter. 2 describes the theoretical background of transistor-antenna and plasmonic mmW antenna integrated direct detectors. It also gives a numerical approach to calculate the antenna resonance frequency, gain and available power on the surface of transistor-antenna structure, which are the important parameters for determining the optical R_v and optical NEP values.

Chapter. 3 explains the details of the electromagnetic design, characterization and experimental results of transistor-antenna structure.

Chapter. 4 presents the generative and inverse design of metamaterial structures through machine learning techniques and its possible future application on designing the monolithic transistor-antenna structure.

Conclusions are presented in Chapter. 5.

Chapter 2

Theoretical background

The use of metallic structures as an antenna on a semiconductor material can enhance the photoresponse of a device, mainly from the strong electric field within the near field, around the metallic structures to further increase the absorption of mmW in the device channel. The concept of using transistor-antenna itself as mmW detector to directly rectify the current induced by antenna structures for mmW detection has been reported. The novel concept is to combine the functions of a plasmonic mmW detection and an antenna within the same structure. Furthermore, with consideration of a practical mmW detection technology, the antennas must meet the requirements of high responsivity and detectivity, simple fabrication, identical photoresponse toward different polarization angles, and the capability of mmW detection over a broad bandwidth.

The operation of plasmonic mmW detectors based on silicon (Si) MOSFETs [22], [24], [61], can be explained by the Dyakonov-Shur plasma wave theory [33], where the plasmonic detectors use nonlinear properties of plasma wave excitations in nano-scale FET channels. A FET can operate as a plasmonic detector in a non-resonant mode by the overdamped plasma wave ($\omega\tau<1$), where ω is the angular frequency of the incoming mmW and τ is the momentum relaxation time in the FET channel. In comparison with compound semiconductors, silicon has less electron mobility in device channel, therefore detectors based on Si are insensitive of incoming radiation of frequency toward 1 THz.

When mmW radiation is coupled to the FET, the ac voltage modulates simultaneously the carrier density and the carrier drift velocity. As a result, the mmW signal is rectified to

a dc signal Δu between the source and the drain (in Fig. 2.1), which is proportional to the received power. Responsivity is mainly determined by the ac voltage, which is generated by coupling a portion of incident wave to FET through an antenna.

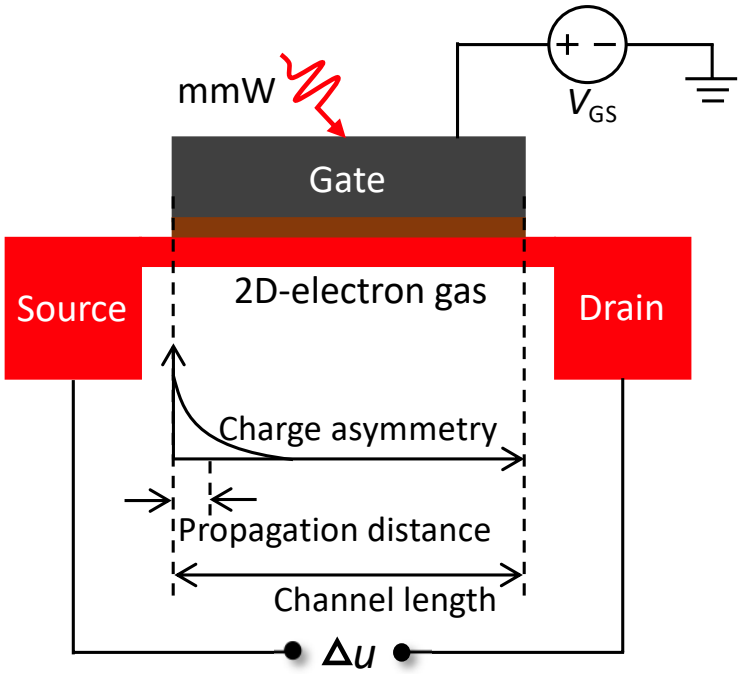

Figure 2.1: Schematic of mmW detection based on FET in non-resonant regime.

2.1 Principle of performance enhancement

The proposed monolithic transistor-antenna device combines the plasmonic and the electromagnetic (EM) aspects. In a single structure, both the increased charge asymmetry and the improved antenna coupling contribute to the enhanced responsivity (R_v) and the noise equivalent power (NEP), which are defined as follows:

$$R_v = \Delta u / P_a, \tag{2.1}$$

$$NEP = N / R_v, \tag{2.2}$$

where Δu is the measured dc output voltage or photoresponse, P_a is the available incident power, and N is the noise spectral density in the FET channel. For FET-based non-resonant

mode plasmonic detectors, we can assume that thermal noise is dominant since drain current is negligible by the dc-open drain configuration [24], [39, 62]. Under the thermal noise assumption, $N \approx (4kTR_{ch})^{0.5}$, where k is Boltzmann's constant, T is temperature in K, and R_{ch} is the channel resistance.

The circular source and the ring-type drain of the proposed structure can increase the charge asymmetry. Under the same asymmetry ratio ($\eta_a = W_D/W_S$) and the source-to-drain top edge distance (l) (in Fig. 2.2), the ring-type channel has a higher electron density than the bar-type channel near the source side since the source curvature in the ring-type structure enables a more confined channel. By extracting the gradient of channel 2-dimensional electron gas (2-DEG) density, the increased charge asymmetry in the ring-type channel is clearly observed, which leads to the enhanced Δu as dc offset voltage [60].

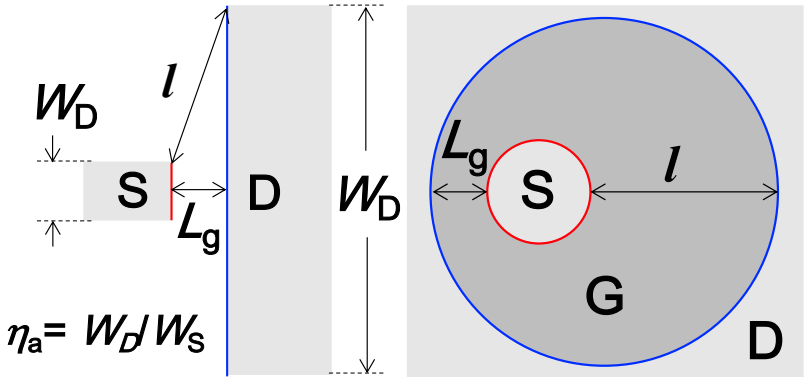

(a) (b)

Figure 2.2: (a) Bar-type structure [43] (b) Ring-type structure having asymmetry ratio η_a by keeping l in the asymmetric channel.

2.1.1 Impedance matching at interface

By proper matching design at the interface between the antenna and the device, the improved antenna coupling can maximize the input power P_{in} to the device. From the equivalent circuit model shown in Fig. 2.3, P_{in} contributes to Δu by the following relation:

$$\Delta u \propto V_{in} \approx V_a \frac{|Z_{in}|}{|Z_a + Z_{in}|} = \sqrt{P_{in} \frac{|Z_{in}|^2}{R_{in}}}, \tag{2.3}$$

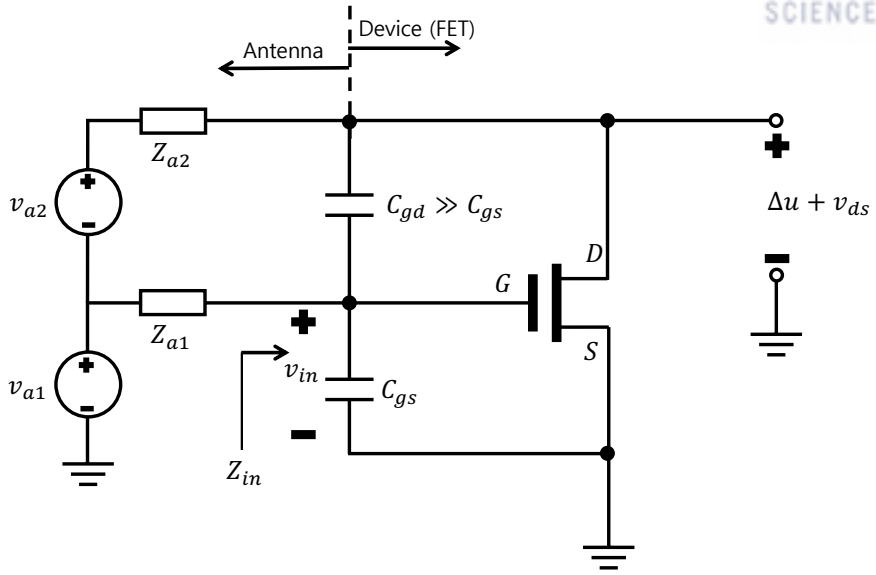

Figure 2.3: Equivalent circuit model of the monolithic circular transistor-antenna structure.

where $V_a = |Z_a(V_{a1}/Z_{a1} + (V_{a1} + V_{a2})/Z_{a2})|$, $Z_a = Z_{a1} \,||\, Z_{a2}$ is the antenna impedance, and Z_{in} is the device input impedance. Although the complete matching design considering Z_a and Z_{in} is desirable, we separately determine Z_{in} to emphasize the charge asymmetry as discussed in the previous paragraph. Matching with Z_a is indirectly considered by determining the diameter of the drain ring, which can maximize the absorptance.

2.2 Resonance frequency

To estimate the resonance frequency (f_r) of transistor-antenna structure, we have followed the following two step process. In first step of calculations, we presented the numerical and theoretical investigation of the wave propagation in 2D periodic array of circular metal patch (in Fig. 2.6) with zero substrate thickness, while in second step as explained in Sec. 2.3, we have optimized the substrate thickness according to resonance frequency through EM simulations.

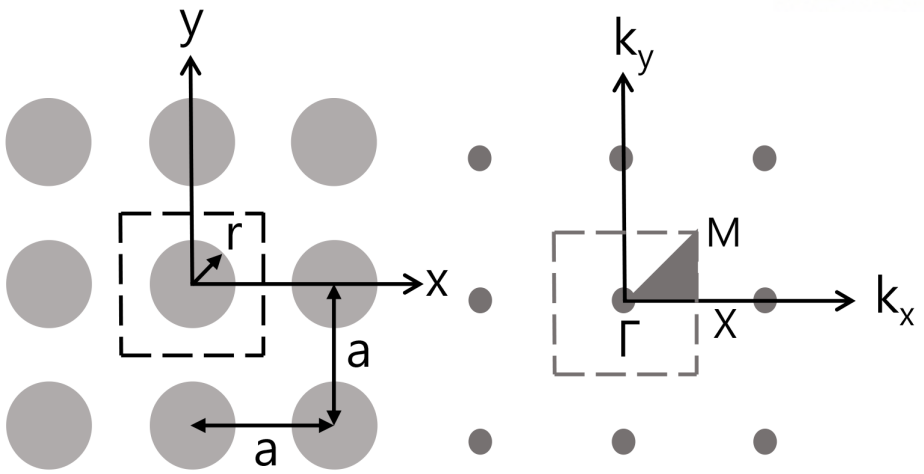

(a) (b)

Figure 2.4: (a) Scheme of 2-D periodic array of metal circle patch with a. (b) Reciprocal lattice and Brillouin zones for square lattice.

2.2.1 2-D periodic array model to initialize the interval of resonance frequencies

The system of a 2-D periodic array of circular metal patch can be described by the periodic conductivity profile shown in Fig. 2.6(a), which for the case of square lattice [63] is

$$\sigma(x) = \sigma(x_\perp) = \begin{cases} \infty, & (x - ma)^2 + (y - na)^2 < r^2 \\ 0, & \text{otherwise} \end{cases}, \tag{2.4}$$

where $x_\perp = x\hat{e}_x + y\hat{e}_y$ is the transverse displacement, r is the radius of the conducting cylinder, a is the lattice spacing, and m, n are integers. The conductivity profile satisfies the following periodic condition:

$$\sigma(x_\perp + T_{mn}) = \sigma(x_\perp) \tag{2.5}$$

with the set of periodicity vectors T_{mn} defined as

$$T_{mn} = ma\hat{e}_x + na\hat{e}_y. \tag{2.6}$$

From Maxwell's equations, the field in the 2-D periodic array of circular metal patches can be decomposed into TE and TM modes. Among the modes on the circular patch, the first four modes are TM, so we calculate wave fields for TM modes only [64]. We can write the following equation [65]:

$$\psi(x_\perp, k_z, \omega) = \int\int \psi(x_\perp, z, t) e^{i(k_z z - \omega t)} dz\ dt \tag{2.7}$$

Assuming that frequency ω and longitudinal wave number k_z are fixed, the Helmholtz equation for $\psi(x_\perp)$ follows the Maxwell's equations.

$$\nabla_\perp^2 \psi(x_\perp) = (k_z^2 - \frac{\omega^2}{c^2})\psi(x_\perp) \tag{2.8}$$

The boundary condition on the surfaces S of the conducting posts for TM mode is

$$\psi\ |_S = 0 \tag{2.9}$$

We can write the fundamental solution of the Helmholtz equation in Bloch form

$$\psi(x_\perp + T) = \psi(x_\perp) e^{ik_\perp . T}, \tag{2.10}$$

where T is any vector of T_{mn}, $k_\perp = k_x \hat{e_x} + k_y \hat{e_y}$. Thus we solve (2.8) inside the fundamental unit cell defined by

$$\left|x\right| \leq \frac{a}{2}, \left|y\right| \leq \frac{a}{2} \tag{2.11}$$

The following periodic boundary condition are deduced from (2.10):

$$\psi(\frac{a}{2}, y) = e^{ik_x a}\psi(-\frac{a}{2}, y), \psi(x, \frac{a}{2}) = e^{ik_x a}\psi(x, -\frac{a}{2}) \tag{2.12}$$

Equation (2.8) together with boundary conditions (2.9) and (2.12) on the surface of the conducting posts for TM mode, defines the eigenvalue problem of finding

$$\gamma^2 = \frac{\omega^2}{c^2} - {k_z}^2 \tag{2.13}$$

as a function of $k_\perp$. The numerical scheme given in [63] can be used to compute eigenvalue problem. In Fig. 2.6 (b), the three special points Γ, X, and M, correspond to $k_\perp = 0$, $k_\perp = (\pi/a)\hat{e}_x$, and $k_\perp = (\pi/a)(\hat{e}_x + \hat{e}_y)$, respectively, where a is lattice constant. Fig. 3.6 shows the resultant dispersion characteristics for the TM modes as the wave vector $k_\perp$ varies from the center of the Brillouin zone (point Γ), to the nearest edge of the Brillouin zone (point X), to the far edge of Brillouin zone (point M). The E-field in the wave is parallel to the metal patches and excites longitudinal currents in them. The alternating current radiates and so a reflection appears. The reflection from different rows with proper phases can generate the total reflection of the wave from the metal patch array, and that is how the band gap forms.

Fig. 2.5 shows the dispersion diagram for the first three TM modes in air and silicon medium. A dispersion diagram is a plot of propagation constant vs frequency. In a 2D periodic structure, where wave travels in two-dimensions, its propagation constant can be written as a vector quantity, $k = \hat{x}k_x + \hat{y}k_y$. The Brillouin zone is the most fundamental region for defining the propagation vector for a unit-cell; basically, if one can define all the propagation vectors in the Brillouin zone, one obtains the entire characteristic of the entire periodic structure. Therefore, the dispersion diagram will start at Γ then to X then to M and back to Γ as indicated by the path depicted in Fig. 2.6.

$$\Gamma\text{: } (k_x r = k_y r = 0),$$
$$\text{X: } (k_x r = \pi, k_y r = 0),$$
$$\text{M: } (k_x r = k_y r = \pi).$$

These dispersion curves demonstrate the propagating bands in square lattice for different modes of operation. Fig. 2.6 and Fig. 2.7 show the simulated electric field distribution on surface of circular metal patch for the first three TM modes, in air and silicon medium. A unit cell eigen mode solver with periodic boundary condition for all lateral faces is used to get dispersion and field characteristics on surface of metal patch. In this setup, the metal patches are assumed to be perfect conductors so as below plasma frequency, metals are able to reflect or bend most of the electromagnetic radiations, and very little fields could sustain inside and on surface. In comparison with Fig. 2.7, the field distributions of Fig. 2.6

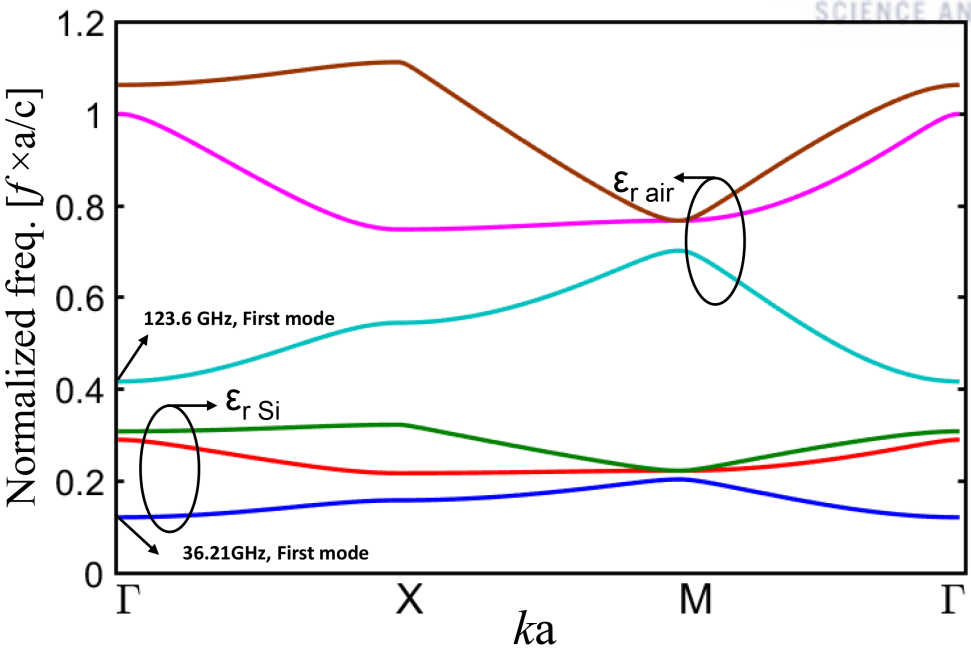

Figure 2.5: Plot of the normalized frequency $f \times a/c$ versus normalized wave number for the first three TM propagating modes in air and silicon medium when $r/a = 0.14$. The cases correspond to a wave propagation in the z-direction with $k_x = k_y = 0$ through the square lattice.

are almost identical except the difference in field magnitude. The field distribution of first mode is TM_{11} kind with maxima and minima of electric field at corners and center of edges respectively.

Using an in-house Matlab code to plot dispersion characteristics of 2D periodic array in air ($\epsilon_r = 1$) and silicon ($\epsilon_r = 11.9$) medium, we can determine the value of r/a that initializes the resonance frequency at Γ point (cutoff frequency) of the first dispersion curve (air, $t_{Si} = 0$ μm). Under the constraint of r/a value, we can determined the value of r so that it is close to $\lambda_{eff}/2$ for a lower reflection coefficient. At the same time, we had to consider fabrication limits given by the device manufacturer when determining the value of a.

2.3 Influence of substrate thickness and its modes

We would like to explain the influence of substrate modes on antenna and device performance. The effective coupling of the FET channel with an incident wave is achieved by

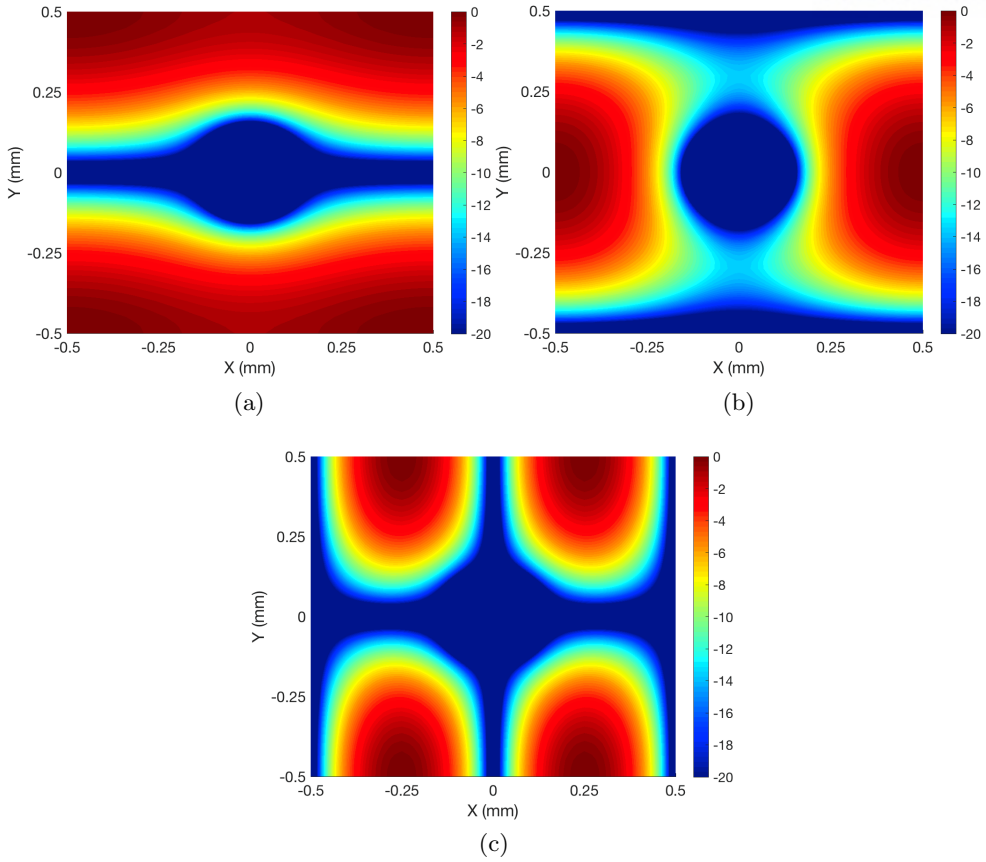

Figure 2.6: Electric field distribution (in dB) plot in x-y plane for first three modes in air medium.

antennas delivering mmW power on channel. A significant portion of incoming radiation, instead of being coupled to the transistors, is coupled to a low resistivity (10 Ω.cm) antenna substrate, which may be lost and/or may be re-directed to same or other detectors [66]. This results in the excitation of substrate modes which plays determinative role in the frequency characteristics of the antenna system and contribute to energy losses. The thicker substrate (t_{Si}>$0.1\lambda_d$) generate more number of substrate modes and have more influence on antenna. Each mode has its cut-off frequency, below which it cannot exist. And the cut-off frequency depends on dielectric thickness and its dielectric constant, defined with the following formula:

$$f_n^{TM,TE} = \frac{nc}{4t_{si}\sqrt{\epsilon_r - 1}}; \tag{2.14}$$

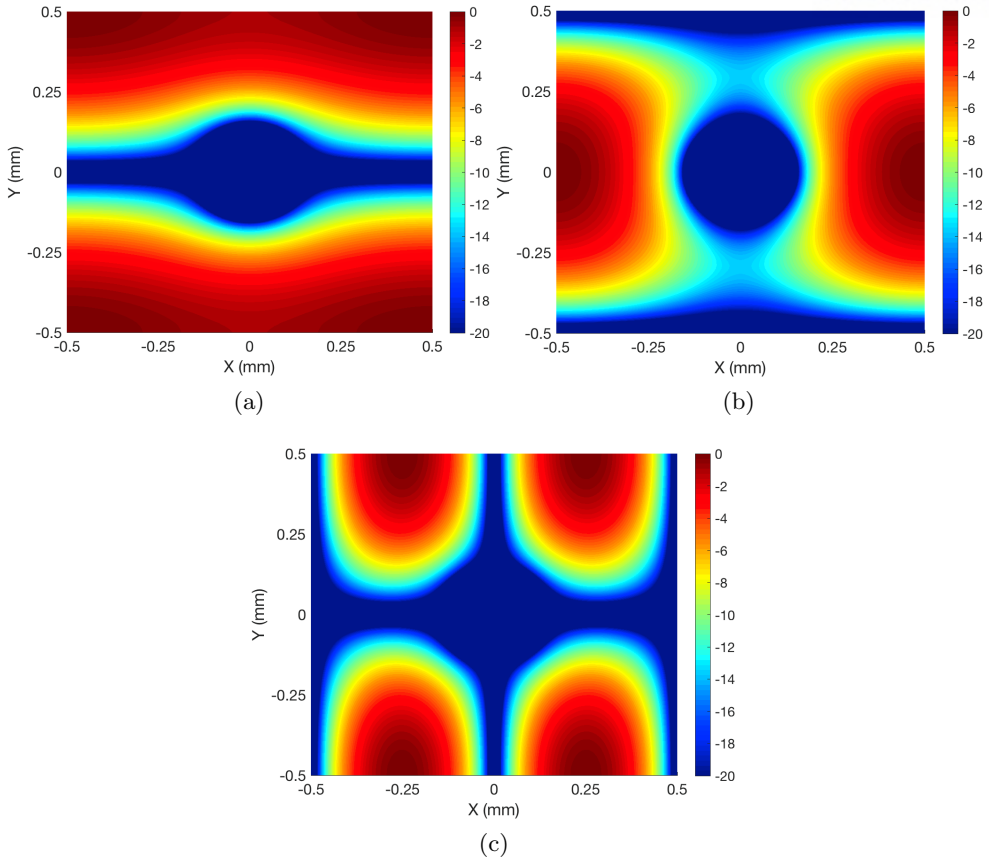

Figure 2.7: (a) Electric field distribution (in dB) plot in x-y plane for first three modes in silicon medium.

where n = 0,2,....or 1,3,....is the mode number for the TM and TE modes, respectively. Therefore, it is needed to determine the optimized substrate thickness through EM simulations to achieve the target resonance frequency by considering possible minimum substrate modes, since the finalized resonance frequency depends on the substrate thickness. Although the thinner substrate is better to suppress substrate modes, it makes the resonance frequency deviate from our target value. Also, the substrate modes influence on the detector performance, we could not consider the effects in the actual design process due limitations of cleanroom fabrication facilities.

2.4 Available power on transistor-antenna

The incident available power is the power captured by the effective area of transistor-antenna structure and it is needed to compute the optical R_v and optical NEP values of device. Neither the air-silicon reflection and absorption nor the mismatch on the way to the FET device should be de-embedded from the responsivity calculation. The detector element antenna pixel gain (G_{det}) is required to consider the effective aperture of receiver antenna for incident power calculation. Since the effective aperture of element antenna pixel is smaller than the physical area of each pixel and also the electrical areas of neighbor pixels doesn't overlap therefore effective aperture of element antenna pixel is used to calculate the available free space incident power. To avoid the issues of near-field region, we could investigate far-field free-space measurement by considering the extender and corrugated horn antenna setup as shown in Fig. 2.8. In the setup shown in Fig. 2.8, we focus on a well-shaped Gaussian output beam from a horn antenna to formulate the available power on the element detector pixel. According to the normalized electric field distribution at any distance along the z axis of propagation, gaussian wave form equation with beam waist and beam radius is expressed as in Eq. 2.15.

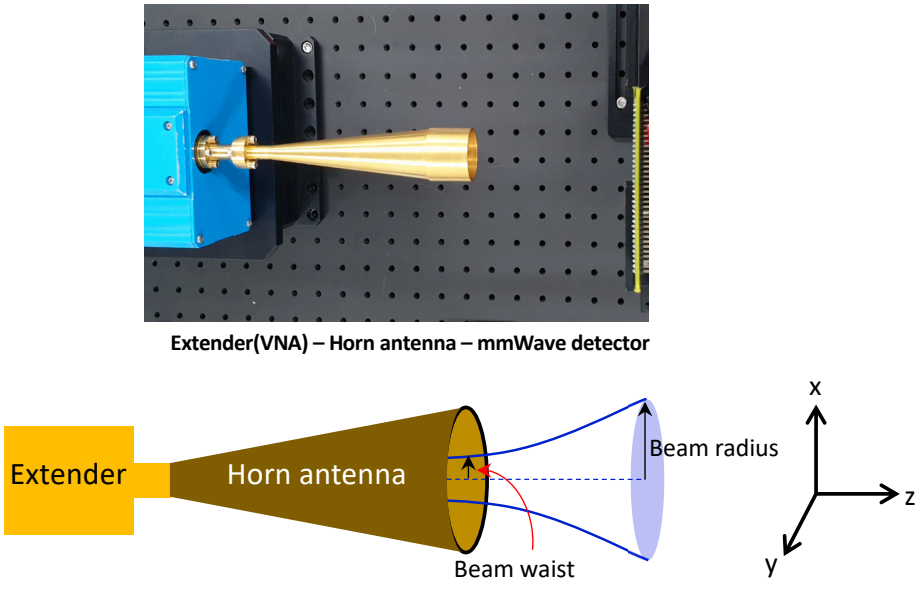

Figure 2.8: Free-space experiment setup with extender and horn antenna.

$$E(x,y,z) = \left(\frac{2}{\pi\omega_x\omega_y}\right)^{0.5}.exp\left(-\frac{x^2}{\omega_x^2} - \frac{y^2}{\omega_y^2} - \frac{j\pi x^2}{\lambda R_x} - \frac{j\pi y^2}{\lambda R_y} - \frac{j\phi_{0x}}{2} - \frac{j\phi_{0y}}{2}\right) \tag{2.15}$$

Where,

$$\omega_x = \omega_{0x}\left[1 + \left(\frac{\lambda z}{\pi\omega_{0x}^2}\right)^2\right]^{0.5}, \omega_y = \omega_{0y}\left[1 + \left(\frac{\lambda z}{\pi\omega_{0y}^2}\right)^2\right]^{0.5} \tag{2.16}$$

$\omega_{0(x\ or\ y)}$ is beam waist radius, and $\omega_{(x\ or\ y)}(z)$ is beam radius [67]. Gaussian beams diverge in the axis of propagation direction (z) and in the paraxial limit, the beam radius as a function of position along the direction is defined as in Eq. 2.16. The available power to the detector element antenna pixel was estimated by the following path-loss formula:

$$P_a = P_t \times \alpha \times G_{det} \tag{2.17}$$

where P_t is the source power fed to the horn antenna, α is power ratio. The power ratio α is the ratio of beam power in detector active area to total beam power at the detector plane, or it indicates how much of the total power is captured by the detector active area. α can be calculated based on Gaussian field distribution of the paraxial Gaussian beam. As shown in Fig. 2.9, the Gaussian beam power density at detector plane will be defined as,

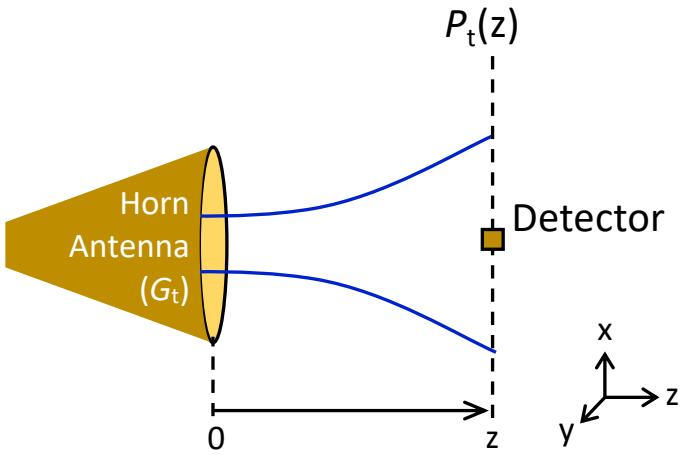

Figure 2.9: Schematic experiment setup for power estimation with horn antenna and detector.

$$P(x,y,z) = P_0(z)\left(exp\left(-\frac{x^2}{\omega_x^2} - \frac{y^2}{\omega_y^2}\right)\right)^2 \tag{2.18}$$

So, beam power arrived at detector active area will be

$$P_0(z) \quad \iint_A \left(exp\left(-\frac{x^2}{\omega_x^2} - \frac{y^2}{\omega_y^2}\right)\right)^2 dxdy\Big|_{z=farfield\ distance} \tag{2.19}$$

where P_0(z) is the maximum power density on propagation axis. The above term can also be written as:

$$P_t \times \frac{\iint_A \left(exp\left(-\frac{x^2}{\omega_x^2} - \frac{y^2}{\omega_y^2}\right)\right)^2 dxdy}{\iint_{-\infty}^{\infty} \left(exp\left(-\frac{x^2}{\omega_x^2} - \frac{y^2}{\omega_y^2}\right)\right)^2 dxdy}\Bigg|_{z=farfield\ distance} \tag{2.20}$$

Where we assume that the source power P_t is equal to the total beam power at detector plane ($z = farfield\ distance$) by neglecting the atmospheric losses. Thus, the beam power received by the detector active area is $P_t \times \alpha$ by defining

$$\alpha = \frac{\iint_A \left(exp\left(-\frac{x^2}{\omega_x^2} - \frac{y^2}{\omega_y^2}\right)\right)^2 dxdy}{\iint_{-\infty}^{\infty} \left(exp\left(-\frac{x^2}{\omega_x^2} - \frac{y^2}{\omega_y^2}\right)\right)^2 dxdy}\Bigg|_{z=farfield\ distance} \tag{2.21}$$

As found in the above expression, the power ratio inherently considers the free space losses and the gain of the transmitting horn antenna. According to Friis transmission formula [32], the receiver detector gain should be included explicitly to determine the total available power on element detector pixel as shown in Eq. 2.17.

2.4.1 Calculation of element detector pixel gain

The element antenna gain can be defined as the ratio of the intensity, in a given direction ($U_{rad}(\theta,\phi)$), to the radiation intensity that would be obtained if the power accepted by the antenna were radiated isotropically [64]. The radiation intensity corresponding to the isotropically radiated power is equal to the input power (P_{in}) given to the antenna divided by 4π. In terms of the equation antenna gain can be expressed as:

$$Gain(\theta, \phi) = 4\pi \frac{U(\theta, \phi)}{P_{in}} \tag{2.22}$$

While, the radiation intensity in (θ, ϕ) direction can also be represented as:

$$U(\theta, \phi) \cong \frac{1}{2Z_0} \left(|E_H|^2 + |E_V|^2 \right) \tag{2.23}$$

Where Z_0 is the free space impedance and we took E_H and E_V values from simulated element radiation patterns to calculate the receiver antenna gain G_{det} in the propagation direction of incident mmW.

Chapter 3

Monolithic transistor-antenna design

In this chapter, we introduce the design and characterization of a circular transistor-antenna structure focusing on its effect on enhanced detector performance results in terms of the plasmonic and the electromagnetic aspects.

3.1 Monolithic circular transistor-antenna device

3.1.1 Structure

Fig. 3.1 shows the conceptual schematic of the proposed monolithic circular transistor-antenna structure mounted on a silicon substrate having the resistivity of 10 Ω.cm. Ring-shape drain and source regions are made from N+ silicon having conductivity in the range of $\sim 10^7$ S/m. The aluminium ring-type gate has the oxide thickness of 50 nm. At mmW frequencies, the total overlapped effective capacitive reactance between gate-drain and gate-source is less than $\sim 3\ \Omega$. Although the effective capacitance may modify the antenna characteristics, its effect is negligible compared to the overall radius of the drain ring. Thus, we can simplify the design procedure by using an approximate model, where the drain, gate, and source jointly behave as a single circular patch. On the other hand, the

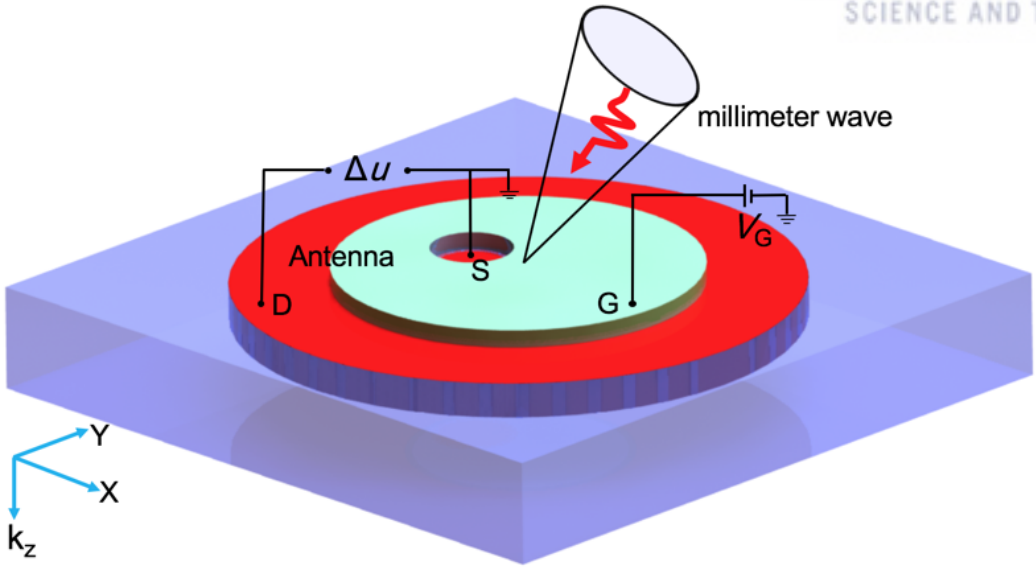

Figure 3.1: Conceptual schematic of the proposed monolithic circular antenna structure based on ring-type asymmetric FET.

increased charge asymmetry between gate-drain and gate-source makes possible to extract dc power at a terminal between the drain and the source, as discussed in Sec. 3.2.1.

Due to a fabrication limit, the substrate thickness t_{Si} of the transistor-antenna structure should be larger than $0.1\lambda_d$, where λ_d is the wavelength inside the dielectric substrate. The electrically thick substrate can excite a significant amount of substrate modes, which can radiate on substrate edges leading to antenna pattern degradation [62]. Since we design the antenna on a thick and conductive silicon substrate, the estimation of the resonance frequency requires a parametric study aided by EM simulation data, to be discussed in Sec. 3.2.2.

3.2 Design and characterization

With the understanding of the basic behavior, we discuss the electromagnetic simulation setup considering pixel array effect. The simulation setup will be used with a proposed method to estimate the resonance frequency and finalize the other design variables.

3.2.1 Electromagnetic simulation setup

A simplified layout of one pixel of the ring-type FET-based monolithic circular antenna is shown in Fig. 3.2. In this work, the FET-based detector includes 20 × 20 antenna pixels, so the entire focal plane array (FPA) structure is large enough to apply periodic boundary conditions without encountering artifacts due to diffraction at device borders. As presented in Fig. 3.3, the structure of a single pixel is embedded into an air box, whose four lateral (or in-plane) walls are set as periodic (master/slave) boundaries. A Floquet port is applied at the top and the bottom of the air box to simulate the incident plane wave. We used High Frequency Structure Simulator (HFSS) [68] to simulate the electromagnetic responses of the circular antenna.

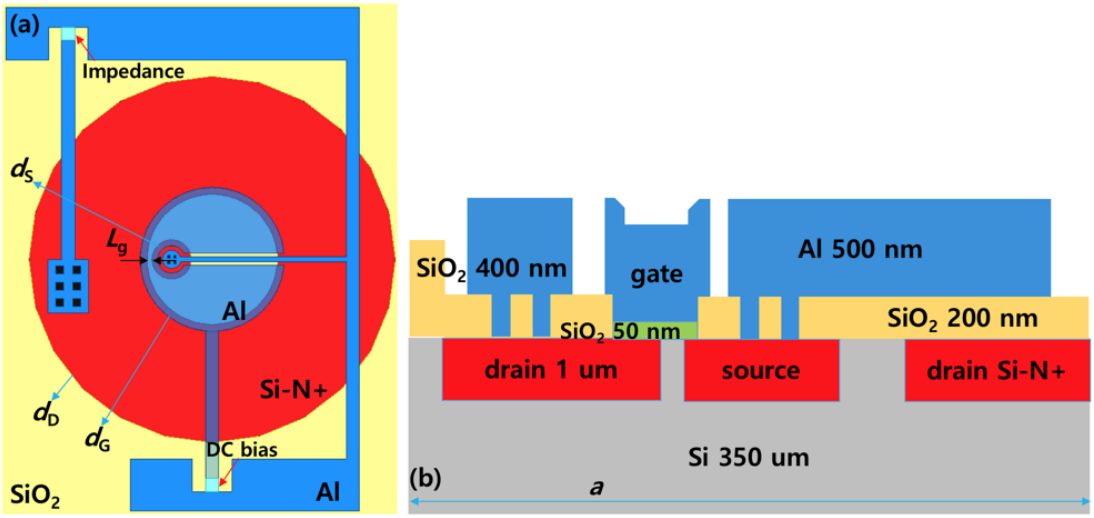

Figure 3.2: (a) Top view of ring-type FET-based monolithic circular antenna with d_S = 30 μm, d_G = 98.4 μm, d_D = 280 μm, and a = 1000 μm. (b) Side view of ring-type FET-based monolithic circular antenna.

Electric field distribution

Fig. 3.4 shows an example of simulated E-field distribution on the surface of a transistor-antenna device. The incoming mmW radiation excites the unit cell as a whole and generates the electric dipole moment around the drain ring of the transistor-antenna device. From the field vector plot, we can observe that the perpendicular E-field on the transistor-antenna surface ensures the excitation of TM kind mode at 120 GHz. Also, maximum power coupling

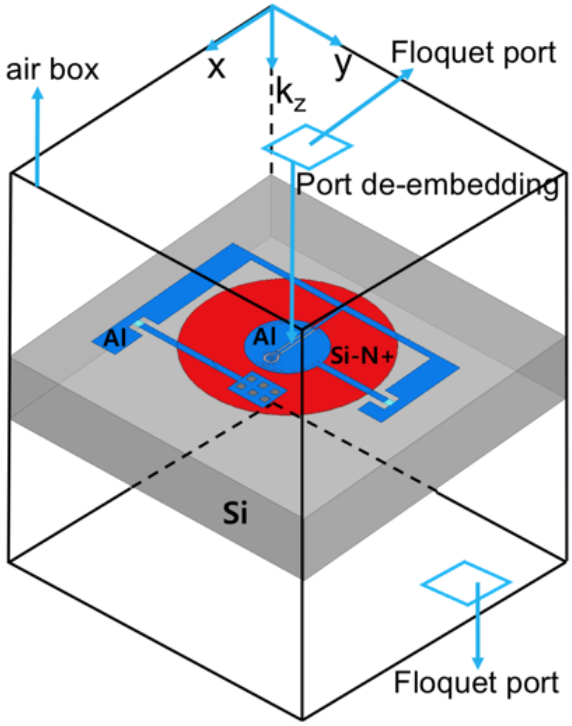

Figure 3.3: Unit cell simulation setup in HFSS: Periodic boundary condition is applied for all lateral faces and Floquet port is set at top and bottom faces.

to the device channel is happening through gate as it is evident from Fig. 3.4 that maxima of electric field amplitude (at resonance) is concentrated around these regions. The effect of dc feed and ground lines should be considered since they carry some currents that modify the frequency response and the resonance as shown in Fig. 3.5. Nevertheless, we can construct a simplified model without the dc feed lines and then tune the design parameters to meet the design target in the final stage.

3.2.2 Design procedure

Aided by the EM simulations, the combination of design variables can be found to maximize the absorption at a given target frequency. However, searching for the desired performance by testing all possible combinations is time-consuming, we present an efficient design procedure that uses an approximate array model and parametric analysis.

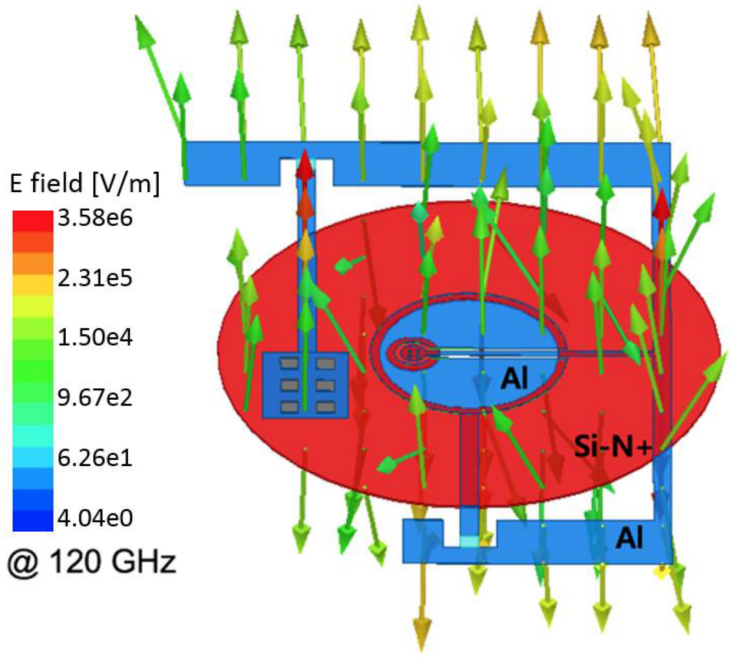

(a) Vector plot

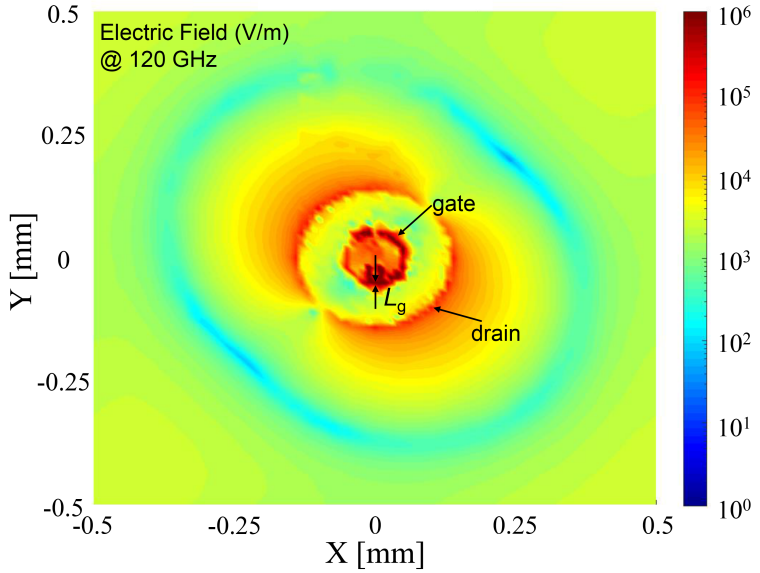

(b) Magnitude plot (@$z = 0$ μm)

Figure 3.4: Simulated E-field distribution on the surface of transistor-antenna.

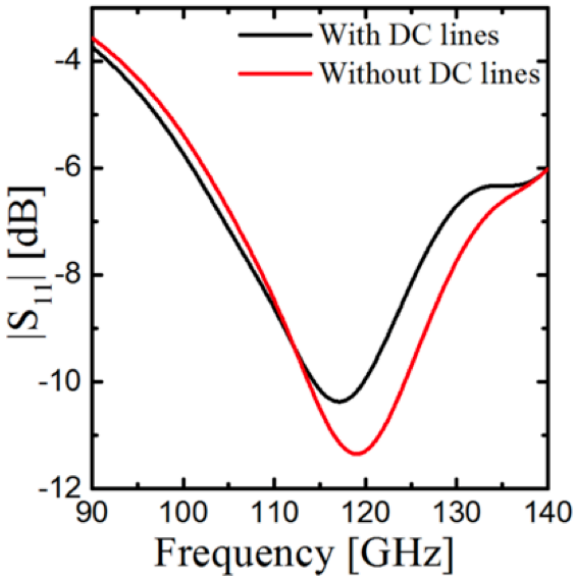

Figure 3.5: Simulated reflection coefficient with and without DC and ground lines.

Initial design under zero-thickness assumption

Absorption of energy of the impinging wave by antenna pixels strongly depends on the geometry of each antenna pixel and its resonance frequency. The resonance frequency relies on pixel size, dielectric thickness t_{Si}, as well as the electric permittivity ϵ_r of the substrate. Although the mathematical description of relations between the performance and the design variables is difficult, we can simplify the problem by considering the 2-D periodic array of circular metal patches with the zero substrate thickness for the first-step estimation of the resonance frequency.

For the system of the 2-D periodic array of circular metal patches with $k_z = 0$, we can obtain band gap diagrams as discussed in Sec. 2.2.1 for a certain value of r/a, where a is the lattice constant and r is the patch radius. By adjusting r/a, we can locate the minimum propagation frequency close to the target resonance frequency. To find the upper and the lower bounds of the resonance frequency, we evaluate two cases, where the background medium is air and silicon, respectively. Since the actual substrate is composed of a finite silicon layer surrounded by air, the resonance frequency will be located in the interval formed by the two cases.

Fig. 3.6 shows the dispersion characteristics for the first three TM modes as the wave vector $k_\perp$ varies from the center (point Γ), through the nearest edge (point X), to the far edge (point M) of Brillouin zone. Fig. 3.6 is plotted at the confirmed value of $r/a = 0.14$, which initializes the resonance frequency at Γ point to be close to the target frequency. Under the constraint of $r/a = 0.14$, we determined the value of r so that it is close to $\lambda_{eff}/2$ for a lower reflection coefficient. At the same time, we had to consider fabrication limits given by the device manufacturer when determining the value of the lattice constant a. The finalized values $r = 140\ \mu$m, $a = 1,000\ \mu$m satisfy all the design requirements. Therefore, the calculated resonance frequency for the above geometry parameters is 123.6 GHz. The estimation of the range and the initial finding of the resonance frequency enables the reduction of design effort before determining the other design parameters.

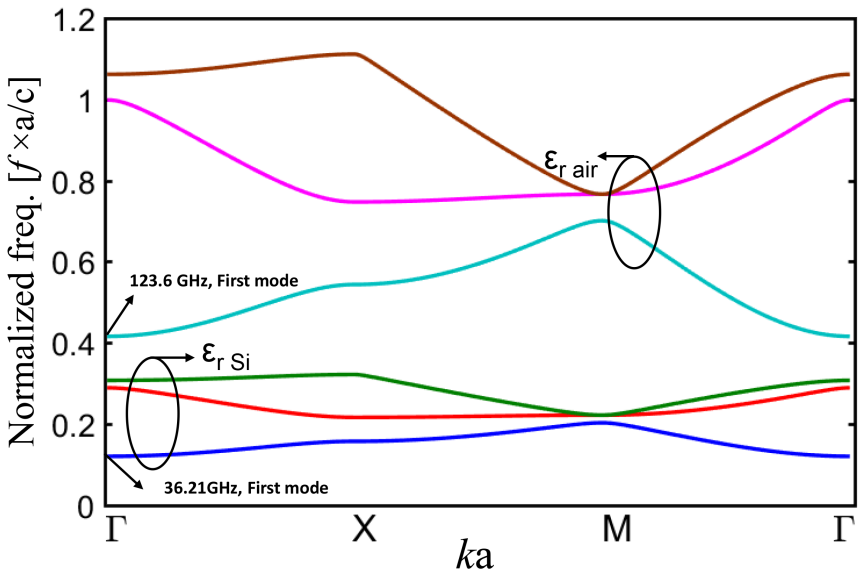

Figure 3.6: Plot of the normalized frequency $f \times a/c$ versus normalized wave number for the first three TM propagating modes in air and silicon medium when $r/a = 0.14$. The cases correspond to a wave propagation in the z-direction with $k_x = k_y = 0$ through the square lattice.

Determination of resonance frequency with a finite substrate thickness

Previously we determined the value of r/a that initializes the design frequency, but assumed the zero thickness. By parametric analysis considering the finite substrate thickness, the resonance frequency can be finalized. A unit cell setup in Sec. 3.2.1 can be used for the

parametric simulation of the monolithic circular antenna. As shown in the parametric simulation results in Fig. 3.7, dominant factors for the variation of f_r are $d_D/2a$ and t_{Si}. The data values obtained from the parametric study of t_{Si} is used in regression algorithm, to get the following relations:

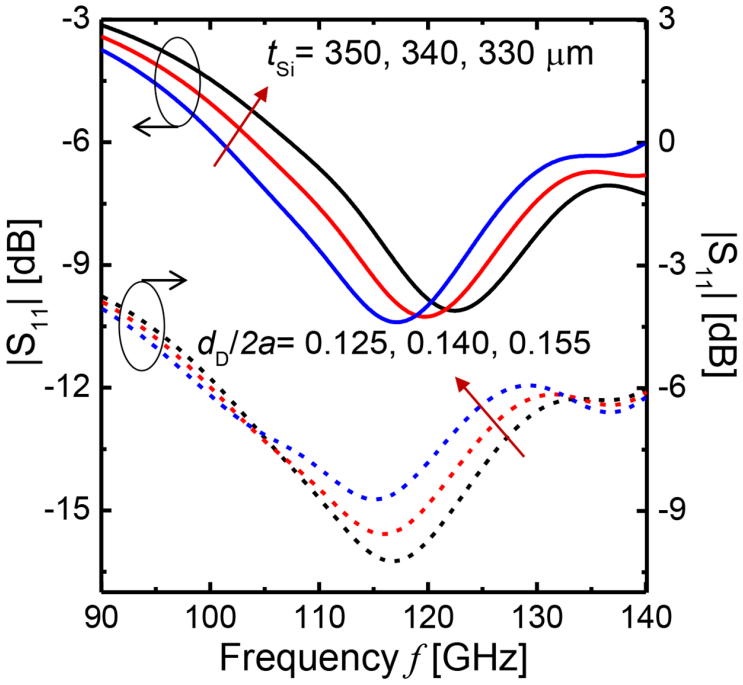

Figure 3.7: Parametric variation of simulated reflection coefficient with respect to $d_D/2a$ and t_{Si} to identify the dominant factors for resonance frequency of ring-type FET-based monolithic circular antenna.

$$k_z \propto \pi\sqrt{\epsilon_r}/t_{Si}$$
$$f_r \propto 1/t_{Si} \tag{3.1}$$

Equation (2.13) in Sec. 2.2.1 is used to model approximate k_z parameter value to modify the resonant frequency calculation to the finalized value i.e. 118 GHz. Fig. 3.7 also shows the data values obtained from the parametric study with the variation of $d_D/2a$. Although the obtained S_{11} is not the best one, we selected $d_D/2a = 0.140$ for our final design since the absorption efficiency (@ 120 GHz) is 2.1 % higher than the case when $d_D/2a = 0.125$. Fig. 3.8 shows the effect of permittivity (ϵ_r) variation of the substrate material [ϵ_r=12.5 (InP), ϵ_r=16.2 (Ge)] on antenna resonance frequency and absorption. With

the permittivity variation in our case, the antenna resonance frequency varies inversely, while the absorption remains similar.

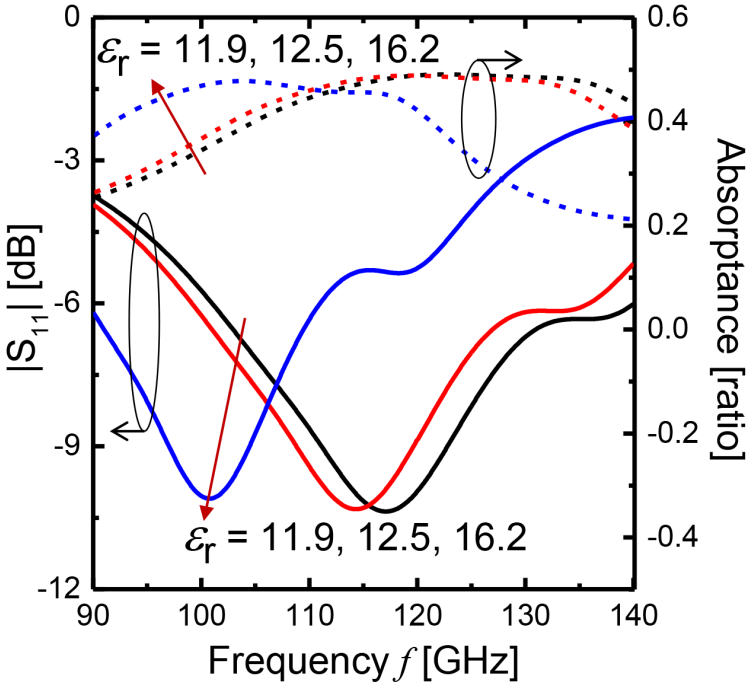

Figure 3.8: Parametric variation of simulated reflection coefficient and absorptance with respect to different substrate material [ϵ_r = 11.9 (Si), ϵ_r=12.5 (InP), ϵ_r=16.2 (Ge)].

Substrate effect

The electrically thick silicon substrate generates TM and TE substrate modes, which are responsible for the increased energy loss and the resultant degradation of device performance [66]. For a thicker substrate ($t_{Si} > 0.1\lambda_d$), a significant portion of incoming radiation, instead of being coupled to the transistors, can be coupled to a low resistivity antenna substrate, where the signal is dissipated or reflected back to nearby detectors. To suppress the generation of substrate modes, employing a thinner substrate is the only solution [66], but minimizing the thickness is not available due to the fabrication limit and the requirement of targeting the resonance frequency.

Table 3.1: Antenna geometry parameters

Parameter	Description	Value (μm)
a	patch-to-patch distance	1,000
r	patch radius	140
d_S	source diameter	30
d_D	drain diameter	280
d_G	gate diameter	98.4
L_g	source-to-drain distance	2
t_{Si}	substrate thickness	350

3.3 Results and discussion

In this section, we present the experimental results from the fabricated device, including scattering parameters, E-field distributions, and performance measures such as photoresponse, responsivity, and NEP. For the fabrication of the monolithic circular transistor-antenna device on the 1×10^{15} cm^{-3} p-doped silicon wafer, the geometry parameters for the design frequency calculated in the previous section were used, as summarized in Table 3.1.

3.3.1 Reflection and transmission results

Fig. 3.9(a) shows a quasi-optical system setup for the measurement of reflection ($|S_{11}|$) and transmission ($|S_{21}|$) coefficients of the fabricated ring-type FET-based monolithic circular antenna array shown in Fig. 3.9(b). Radiation at $f = 120$ GHz was generated by VNA through a Gaussian horn antenna, and off-axis ellipsoidal (OAE) mirror was used to focus the millimeter wave on the circular antenna sample shown in Fig. 3.9(c). The measured reflection, transmission, and absorptance profiles are fairly correlated to simulation results, as shown in Fig. 3.10. The discrepancies between measured and simulated results originate from possible fabrication and measurement errors. About 5 % discrepancy in measured and simulated absorption magnitude is due to the negligence of possible dielectric and metal losses when modeling the device during measurement. There is also a peak shift in absorptance profile due to possible human errors that limits the perfect incident of mmW on

the device. In Fig. 3.10(c), power absorption is obtained with about 50.9 % of total power at 120 GHz. In addition, due to a mismatch loss at the antenna-to-FET interface, about 72.9 % out of the total absorbed power excites two-dimensional electron gas in the channel. Fig. 3.11 shows the impedance parameters of the monolithic circular antenna. The reactive component of impedance is around zero at the resonance frequency, where the power loss of the monolithic circular antenna becomes negligible.

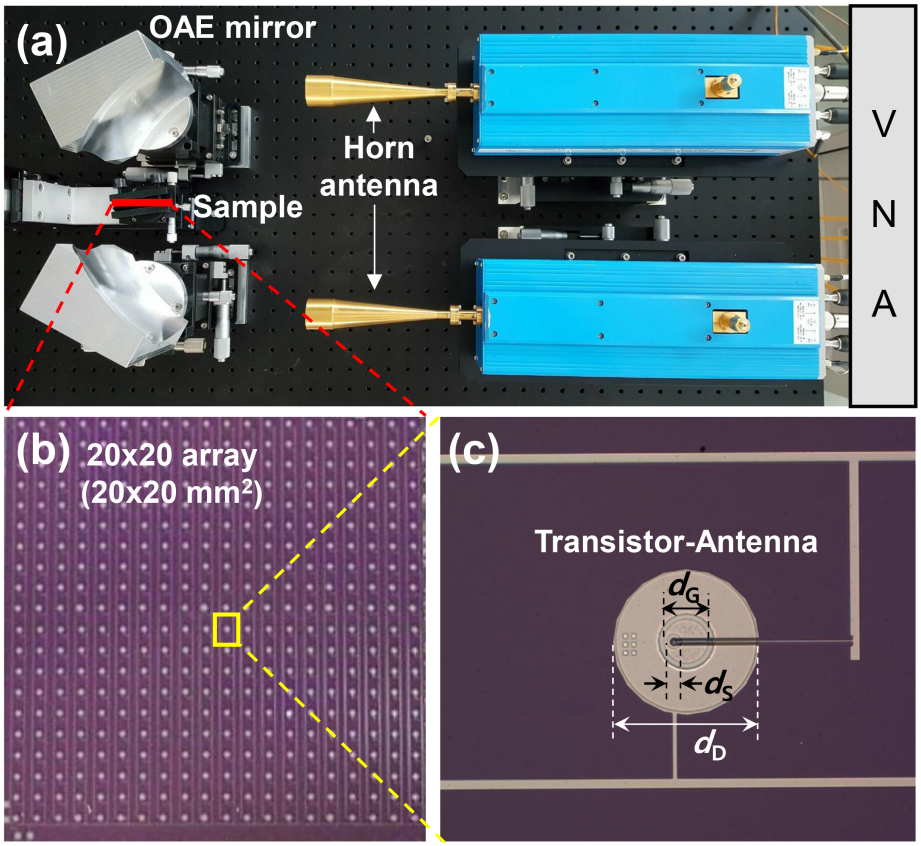

Figure 3.9: (a) The measurement setup for obtaining the s-parameter of designed ring-type FET-based monolithic circular antenna by using quasi-optical system with Gaussian beam radius of 8 mm. (b) Sample of 20×20 array and (c) ring-type FET-based monolithic circular antenna.

3.3.2 Experimental electric field analysis

As illustrated in Fig. 3.12, E-field intensity is measured on the antenna plane (20×20 mm^2) separated by 0.5 cm with a scanning resolution of 0.2 mm (10,000 scanning points). A 120 GHz TE_{10} mode signal generated from a WR08 VNA extender was fed to a W-band

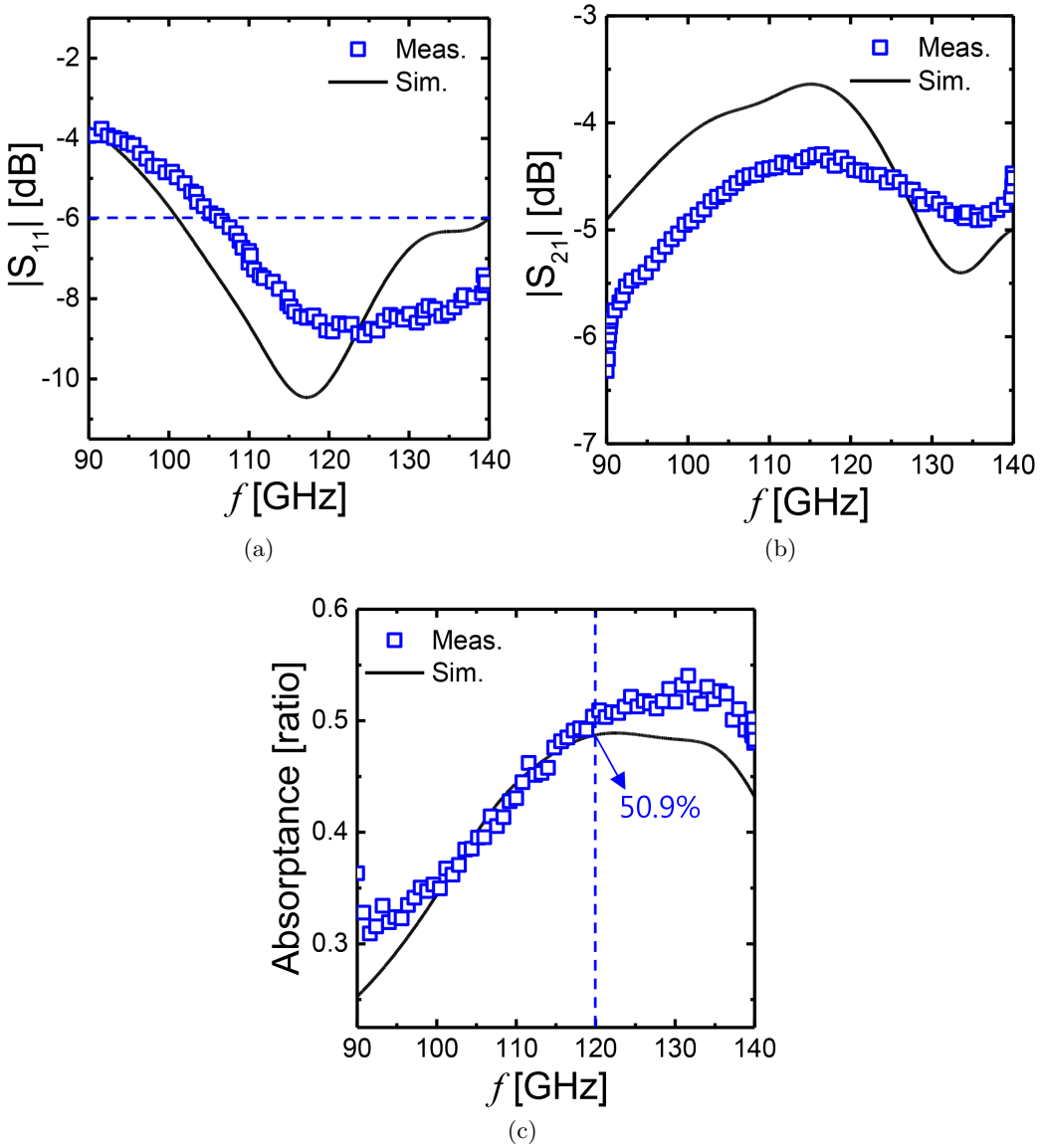

Figure 3.10: Measurement and simulation results of (a) reflection coefficient ($|S_{11}|$), (b) transmission coefficient ($|S_{21}|$), and (c) absorptance ($1-|S_{11}|^2-|S_{21}|^2$).

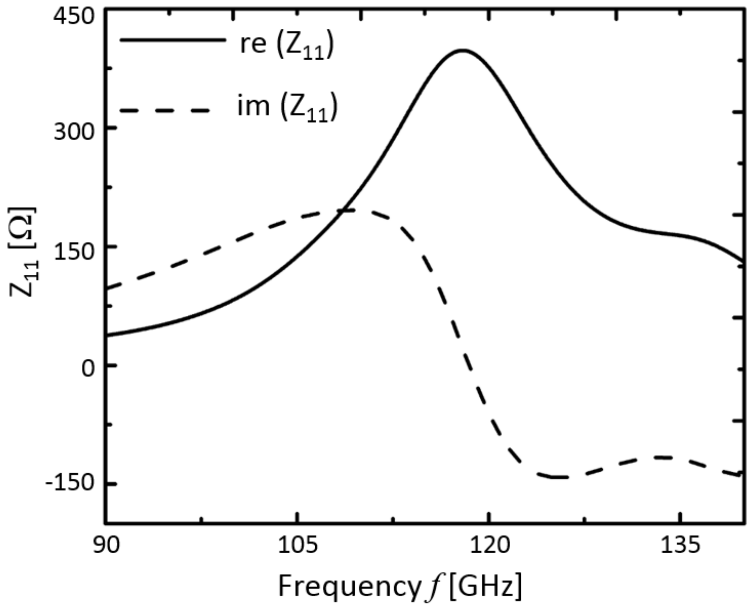

Figure 3.11: Simulated impedance parameters.

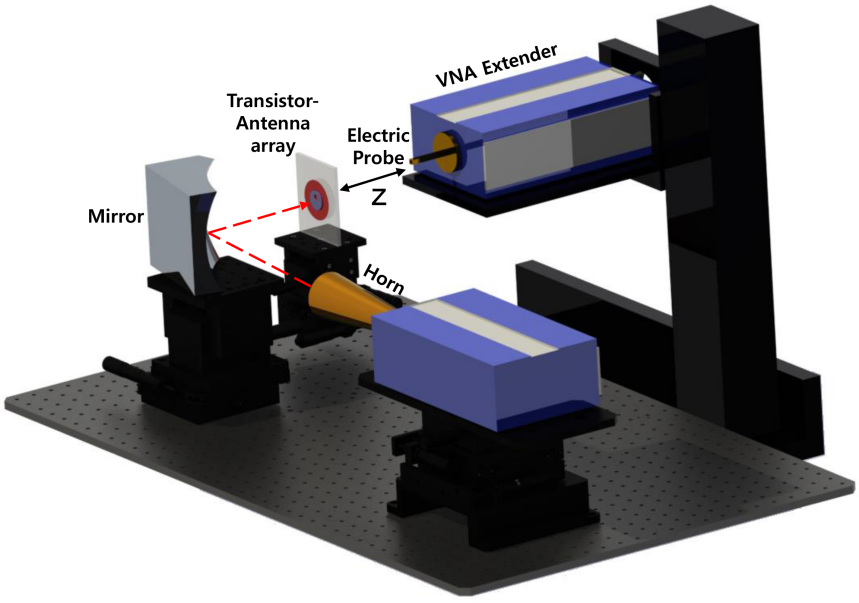

Figure 3.12: Measurement setup for obtaining E-field intensity.

Gaussian horn antenna, which converts the TE_{10} mode into a Gaussian beam propagating in free space. The Gaussian beam was then incident on a monolithic circular antenna focal X-Y plane. The measured E-field intensity at antenna X-Y plane is shown in Fig. 3.13. The measured intensity distribution has the circular shape with the maximum intensity at the center along with nearly uniform phase distribution for the normal incidence. The

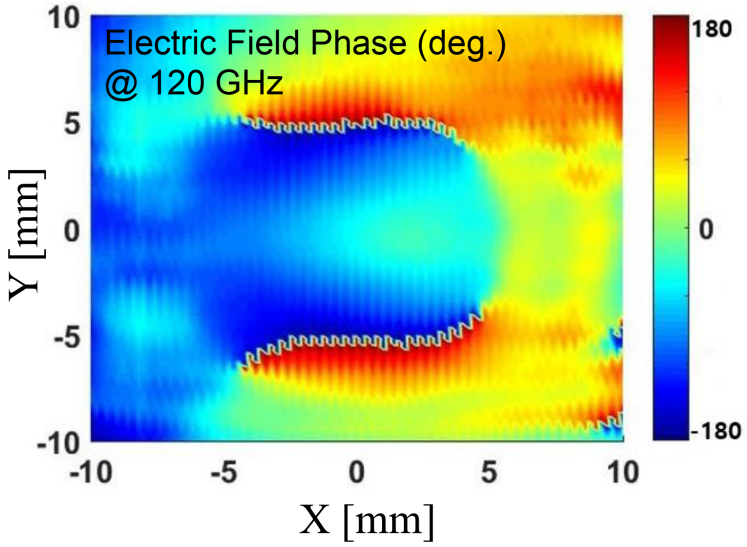

(a)

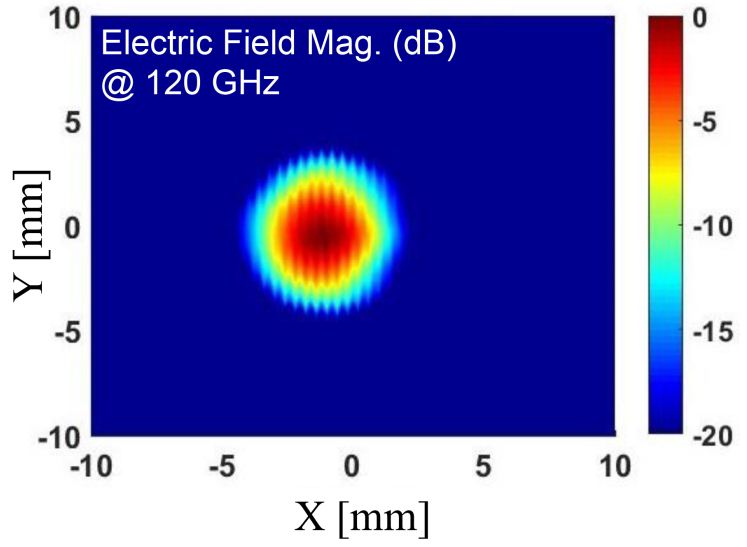

(b)

Figure 3.13: Measured 2-D intensity profile of the 120 GHz beam for $z = 0.5$ cm position in the propagation direction of the incident wave (a) Magnitude (b) Phase

intensity profiles were obtained by extracting the intensity values along the 1-D cross section

line of the 2-D transversal X-Y intensity profiles. The z-position was measured relative to the focal plane, as shown in Fig. 3.14. From the figure, we can observe that 1-D intensity profiles of the mmW beam for z-position in propagation direction of the incident wave for perpendicular and parallel polarization are almost identical, indicating that field profiles on the circular antenna is polarization insensitive. To confirm whether the circular transistor-

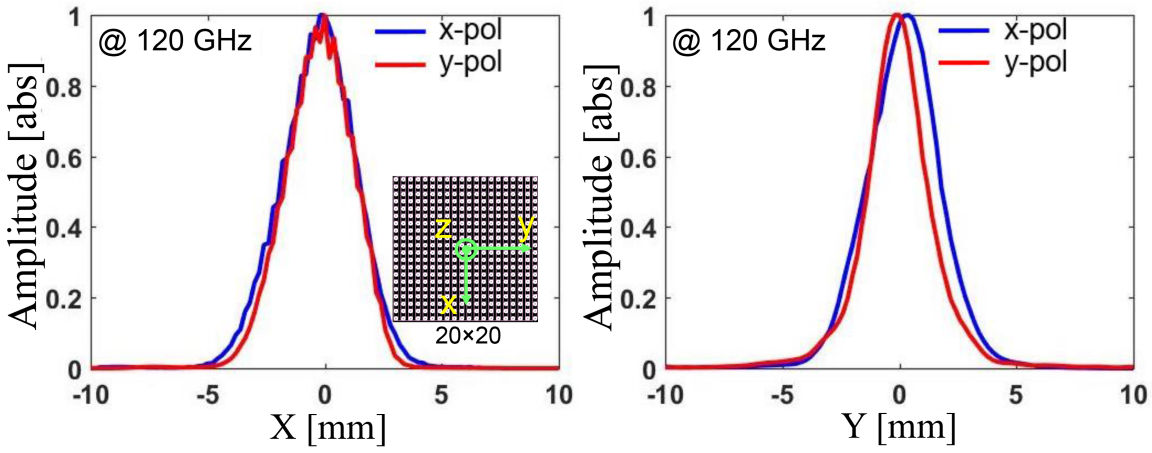

(a) (b)

Figure 3.14: Measurement of normalized 1-D intensity profile of the mmW beam for $z = 0.25$ cm position in propagation direction of the incident wave, scanned in two axes for two different incident polarizations (a) Scanning in X-axis (b) Scanning in Y-axis

antenna can absorb E-fields and transfer them to dc output, we also measured the E-fields on the plane at $z = 0.25$ cm with and without the antenna for difference frequency values, as shown in Fig. 3.15. The significant absorption of E-field (-16.72 dB @ 120 GHz) on the surface of the antenna guarantees the improved dc output voltage, resulting in the enhanced responsivity.

3.3.3 Radiation pattern and gain

The simulated radiation patterns of transistor-antenna array are given in Fig. 3.16. In Fig. 3.16(a), the XZ-plane element pattern is wide in shape and its 3-dB bandwidth is around 157.9°, while YZ-plane element pattern is fairly directional over the band. The effect of the element pattern appears in the total radiation pattern in Fig. 3.16(b), the 3-dB bandwidth of which is about 13.0°. The gain of the proposed antenna element over the

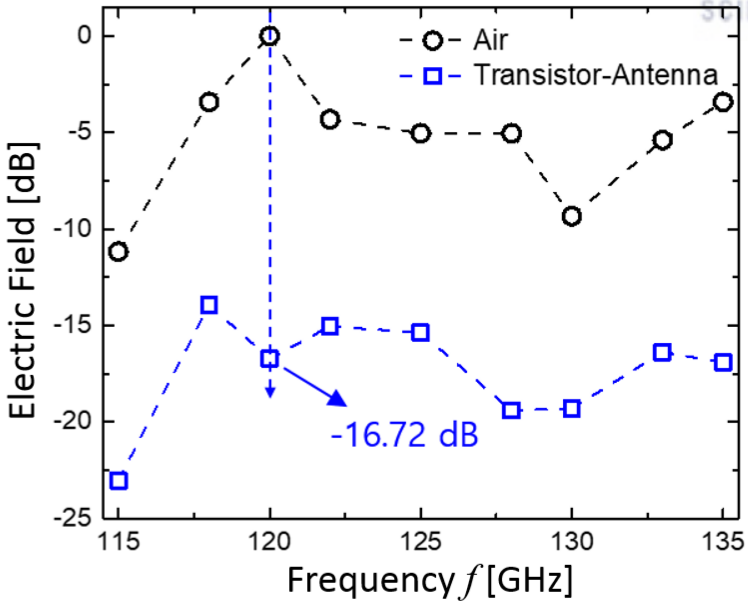

Figure 3.15: Normalized E-field of the mmW beam measured at $z = 0.25$cm with and without the transistor-antenna device in the propagation direction of the incident wave.

frequency range is given in Fig. 3.17, which is derived from the method given in Sec.2.4.1, while the simulated antenna radiation efficiency is observed to be ∼52.75 %.

3.3.4 Available power on element detector

Fig. 3.19 shows the measurement setup for mmW signal detection at 120 GHz. By connecting a corrugated horn antenna to the extender and maintaining 100 mm distance between the end of the horn and the detector, we confirmed the far-field condition so that the following path-loss formula can be applied:

$$P_a = P_t \times \alpha \times G_{det} \tag{3.2}$$

where P_a is the available power on the element detector pixel, P_t is the total source power, α is the ratio of the beam power on the detector active area to the total beam power on the entire receiving plane, and G_{det} is the gain of the element detector pixel antenna. Before placing the detector sample, we measured P_t to be fed to the horn antenna, by using a power meter at the waveguide port of the VNA extender. α, which includes the gain of the transmitting antenna and the free space losses, can be calculated based

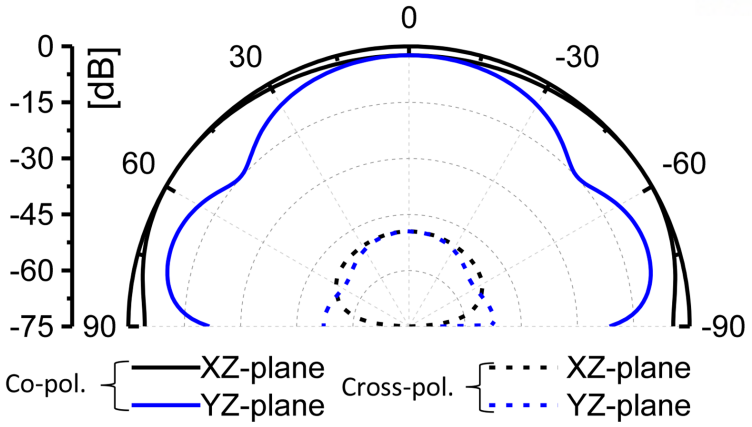

(a) Element pattern

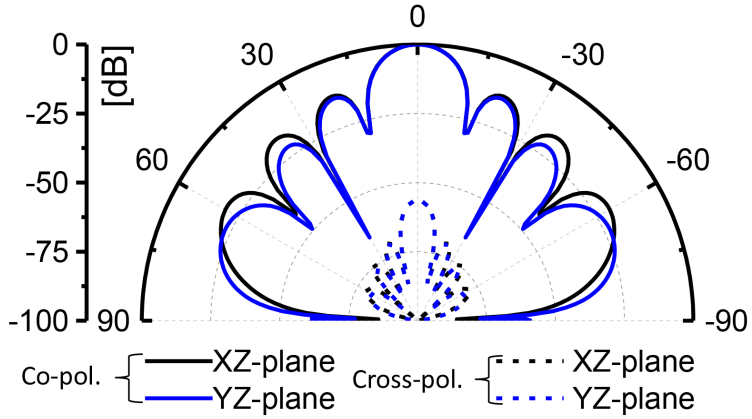

(b) Total pattern

Figure 3.16: Simulated antenna radiation patterns at 120 GHz.

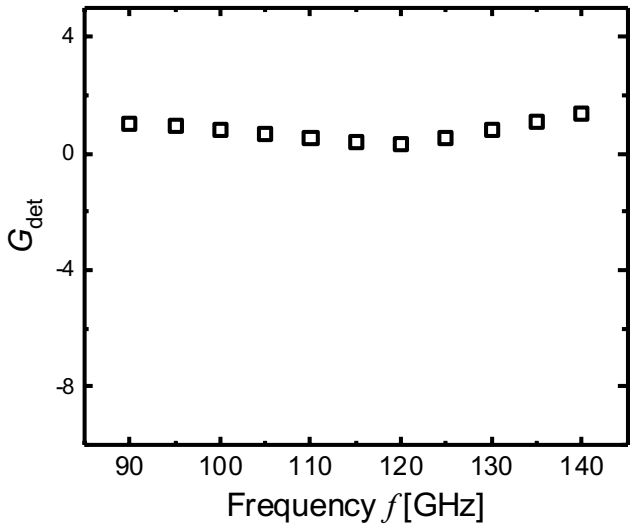

Figure 3.17: Element detector pixel antenna gain.

on the field distribution of the paraxial Gaussian beam [67] as discussed in Sec.2.4. At farfield distance of z=100 mm, Fig. 3.18 shows the experimentally obtained beam profile at 120 GHz as normalized Δu with unit of decibel (dB). If the normalized Δu=-8.7 dB as $1/e^2$ [67], the width of beam profile is defined as beam diameter. With beam radius of r_{beam} = 12.6 mm @ z= 10 mm, from Eq.2.21 the α is 2.466 $\times$ 10^{-4}, which is used to calculate the effective available power of 42.39 nW on the detector active area at 120 GHz.

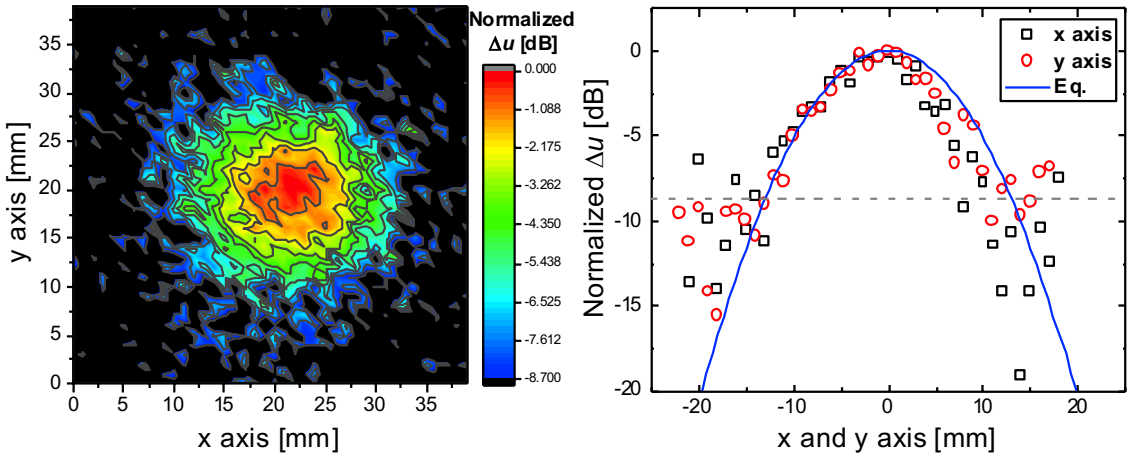

(a) Element pattern (b) Total pattern

Figure 3.18: Contour plots of (a) beam profile and (b) beam width as 2×beam radius (r_{beam} = 12.6 mm @ z= 100 mm) with analytic equation (Eq. 2.16).

Since P_a is calculated from the path-loss formula (3.2) without any loss correction due to reflection, absorption, and mismatch, we can obtain optical responsivity and optical NEP values through (2.1) and (2.2), respectively.

3.3.5 Experimental results of mmW detector

When measuring the fabricated transistor-antenna detector, dc gate bias was applied through the source meter. The output signal at the drain of ring-type FET-based monolithic circular antenna is delivered into a lock-in amplifier with a 10-MΩ load, which provides a trigger signal with a chopping frequency (f_{chop}) of 2 kHz to modulate the mmW signal.

For the quantitative verification of the performance of the fabricated circular antenna, we fabricated a patch antenna-integrated bar-type FET with feeding lines as a reference

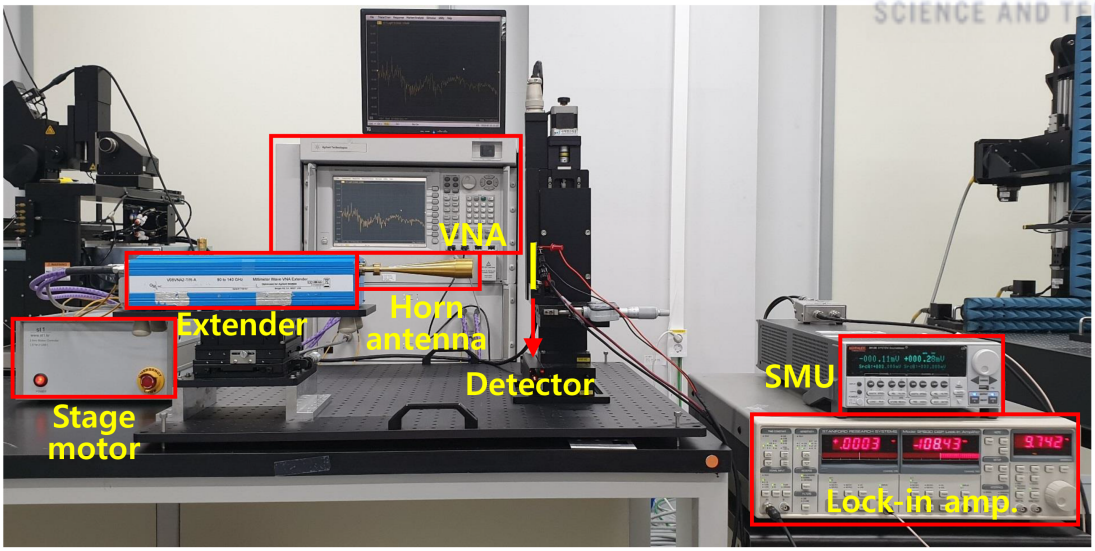

Figure 3.19: Measurement setup for ring-type FET-based monolithic circular antenna at 120 GHz system with a chopping frequency (f_{chop}) of 2 kHz.

device [43]. The patch antenna with the feeding line has been monolithically integrated as the electrode metal layers of the gate (signal) and source (ground) terminal of FET operating in low-impedance regime. The antenna was fabricated on p-type Si(100) wafer at a doping concentration of 1×10^{15} cm^{-3} and a thickness of 200 μm. Feeding line width is determined from the characteristic impedance (Z_0), and all the other dimensions are designed at 120 GHz. For plasmonic detection of FET, gate-to-source complex impedance (Z_{gs}) is matched with antenna characteristic impedance $Z_a = Z_0$ (real) for smaller reflection and higher photoresponse (Δu) of drain (output) dc voltage [43].

Measurement results of the ring-type FET-based monolithic circular antenna and the reference in-plane patch antenna with feeding lines are plotted in Fig. 3.20, where the full measurement protocol is used for determining the responsivity (R_v) and the noise-equivalent power (NEP). For the both devices, responses were measured under the excitation at 120 GHz. The dc output $\Delta u = 46.9$ μV is highly enhanced from 5 μV of the reference patch antenna sample on the same η_a= 10, as shown in Fig. 3.20(a). After the estimation of actual power (P_a) and cold-FET thermal noise by standard procedure [43], we demonstrated the enhanced $R_v \sim 1.1$ kV/W ($\times$ 5.5) [60]. In this enhancement, we can find that the increased charge asymmetry achieves 1.89 times the R_v of the bar-type detector by on-chip probing

measurement. Therefore, the estimated contribution of the improved antenna coupling is 2.9 times the R_v of the bar-type detector.

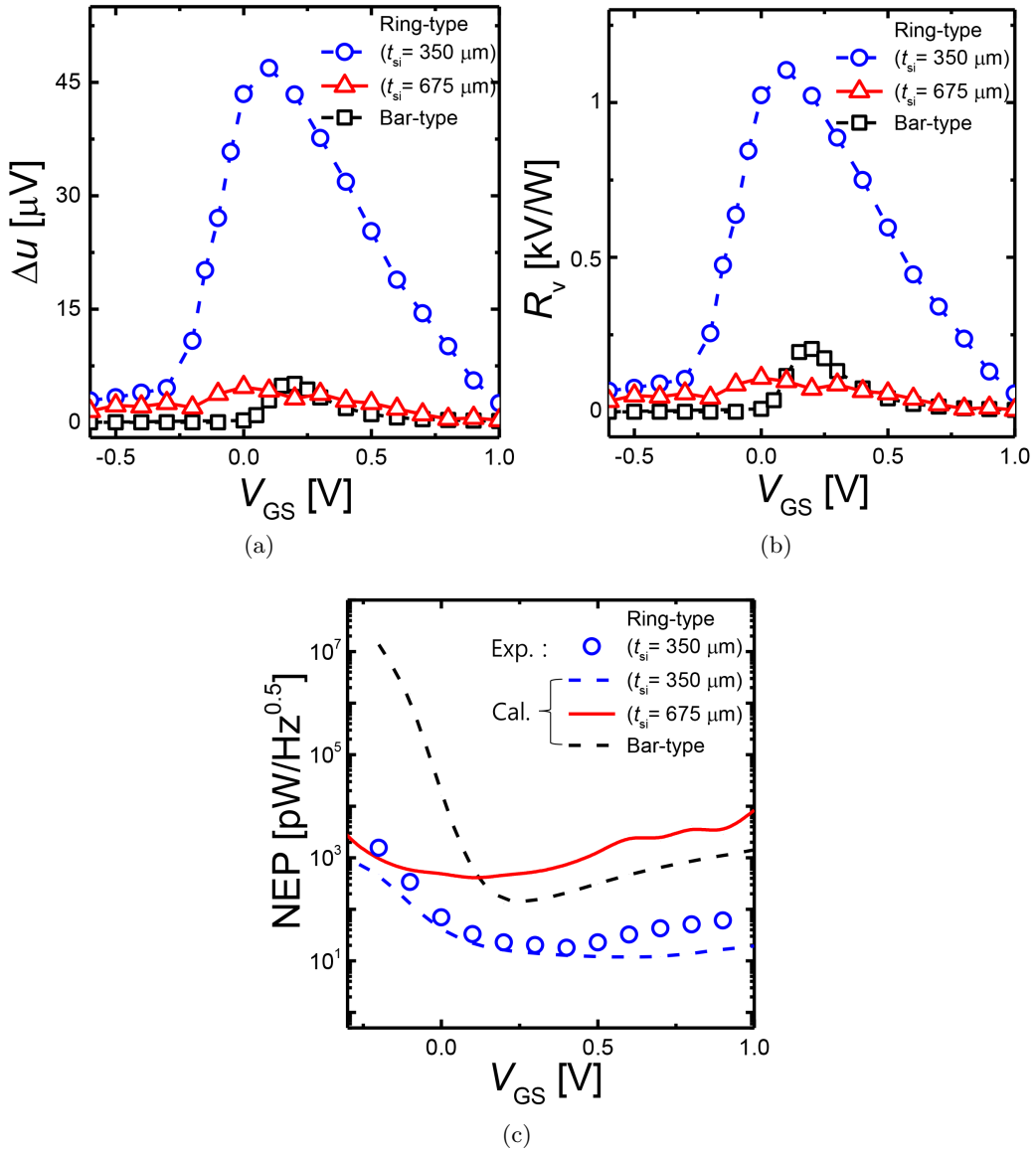

Figure 3.20: Measured data for ring-type FET-based monolithic circular antenna device and bar-type detector at 120 GHz and f_{chop}. (a) Photoresponse Δu (b) Responsivity $R_v = \Delta u/P_a$, where P_a = 42.4 nW for the ring-type FET-based monolithic circular antenna device and P_a = 25 nW for the reference bar-type detector. (c) NEP = N/R_v, where N is the total noise of the detector. The Exp. plot is made with the measured N while the Cal. plots are made with the calculated N under the thermal noise assumption.

For the ring-type FET-based circular antenna, we obtained the NEP based on the noise spectral density (N) from a power spectrum measurement method. As shown in

Table 3.2: Detector performance @ 120 GHz

Detector device	DC output voltage Δu (μV)	Optical responsivity $R_{v,\mathrm{MAX}}$ (V/W)	Optical noise equivalent power $\mathrm{NEP}_{\mathrm{MIN}}$ (W/$\sqrt{\mathrm{Hz}}$)
ring-type ($t_{Si} = 350\mu$m)	46.9	1,105 @ $V_{GS} = 0.1$ V	1.78×10^{-11}
ring-type ($t_{Si} = 675\mu$m)	4.67	110.2 @ $V_{GS} = 0$ V	2.96×10^{-10}
bar-type [43]	5	204 @ $V_{GS} = 0.2$ V	1.313×10^{-10}

Fig. 3.20(c), the measured NEP values are properly correlated with the NEPs calculated under the thermal noise assumption. Although the measured N includes a small amount of shot noise caused by leakage currents, we can find that thermal noise is dominant since N clearly depends on V_{GS}. Finally, we demonstrated the reduced NEP $\sim$ 18 pW/Hz$^{0.5}$ ($\times$1/7.4).

To verify our design approach, we also measured and compared the performance values of the ring-type FET based monolithic circular antenna for two silicon substrate thicknesses. The increase in the thickness of silicon substrate degrades the performance of the ring-type FET detector since additional substrate modes are generated. Compared to the ring-type FET detector with $t_{Si} = 675$ μm, our finalized design with $t_{Si} = 350$ μm exhibits higher R_v value ($\times$ 10) and improved NEP ($\times$ 1/16). The measured performance parameters at 120 GHz are summarized in Table 3.2.

3.3.6 Bandwidth of complete detector response

Fig. 3.21 shows the measured frequency response of the photoresponse and the responsivity, from which the full width at half maximum (FWHM) is about 23 GHz. The measured bandwidth of the entire detector response covers more than half of antenna bandwidth characteristics in Fig. 3.10, where high absorptance values of the antenna are observed around

at the same frequencies of the detector response. We have followed the identical procedure as described in above section for each frequency to calculate the detector response over operational frequency band. Since the conventional non-resonant plasmonic FET devices have almost a constant frequency response, we can find that the FWHM of the detector is mainly determined by the matching performance of the circular antenna.

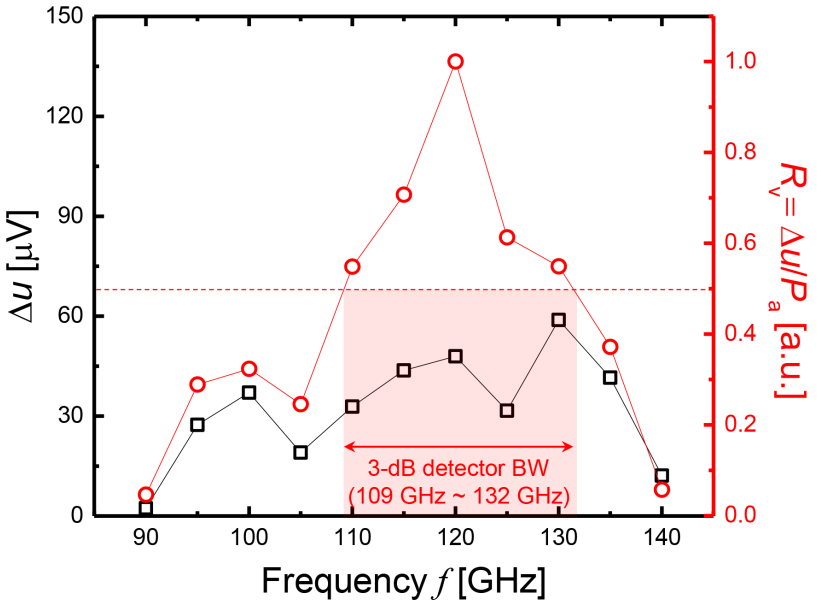

Figure 3.21: Measured photoresponse Δu and normalized responsivity R_v of the detector over the operation frequency band.

3.3.7 Comparison among state-of-the-art antenna integrated direct detectors

As summarized in Table 3.3, the results obtained in this work are in comparable order with the lowest NEP and the highest R_v values of a reported current-state-of-the-art CMOS-based antenna integrated direct detectors by excluding amplifiers [40]. Therefore, our ring-type FET based transistor-antenna can compete with other commercial detectors by taking advantages of low-cost and high integration density CMOS technology for real-time mmW imaging application.

Table 3.3: Detector performance excluding amplifiers

Technology	f [GHz]	Responsivity R_v (V/W)	Noise equivalent power NEP (pW/$\sqrt{\text{Hz}}$)	Ref.
250 nm CMOS	645	566	300	[39]
2 μm CMOS	200	222	120	[69]
120-300 nm CMOS	700	200	100	[62]
65 nm CMOS	856	250	100	[23]
150 nm CMOS	595	350	20	[70]
65 nm CMOS	200	1.5k	15	[44]
65 nm CMOS	724	2.2k	14	[40]
130 nm CMOS	823	†3.46k	12.6	[31]
22 nm CMOS FD-SOI	855	1.51k	12	[32]
130 nm SiGe HBT	260	†2,600k	7.9	[19]
130 nm SiGe HBT	430-476	5±0.6k	2.7-3.4	[20]
130 nm SiGe HBT	400-500	‡3.1k	N/A	[21]
2 μm CMOS	120	1.1k	17.8	This work

†: Including an on-chip amplifier
‡: Current Responsivity R_i (A/W)

Chapter 4

EM structure design with machine learning

4.1 EM structure design through Bayesian Learning

Multi-dimensional electromagnetic (EM) structures are variously applicable because they can smartly manipulate EM waves and reduce circuit sizes [71]. However, increased density of the EM structures results in narrower system margins with a larger number of design variables to be optimized. Consideration of the overall dimensions with the design variables requires a substantial computational burden and a longer design cycle. Although analytical methods through equivalent circuit models can be used, they are only efficient for limited cases of EM structure design. In practice, the modeling of EM structures should be accompanied by a series of costly full-wave EM simulations for any design update since the parameter relationship for most of the design is highly nonlinear. As a solution to the design complexity, machine learning algorithms are being considered recently [72, 73]. However, the application of machine learning to practical EM design problems is available only when noisy and high-dimensional data are handled properly.

For the efficient adaptation of realistic high-dimensional EM dataset to machine learning algorithms, we propose a new relational hypergraph (simplicial complex), termed as Electromagnetic Design Complex to capture relations between input geometric parameters

for EM structure and output performance parameters. We then design a bayesian inference engine, called Bayesian Clique Learning, to search high-dimensional cliques (clique simplicial complex) that provide the functional relations between the input and output parameters. Our Bayesian Clique Learning converges faster on searching the optimum design parameters, by exploiting the regular structures of clique simplicial complex embedded in our EM simulation data. We classify our data set into high, mid, and low ranges and run the learning algorithm to search optimum design on these individual ranges. We have given the computational complexity order of our algorithm and showed its advantage over the traditional methods of EM design. For verification, the proposed algorithm is applied to dataset from two different metamaterial (MTM) structures, achieving the reduction of computational complexity by 21.87 % and 86.79 %, respectively.

4.1.1 Proposed method

The metamaterial (MTM) EM structures of Fig. 4.1 is used to test the effectiveness of our proposed method. The macroscopic properties of MTMs are harnessed by engineering the geometric dimension of MTM structures, which are required to generate the desired magnetic and/or electric responses to externally applied fields. The present structure (zero-index MTM) was developed by designing subwavelength elements working within a frequency range where either the effective permittivity or the permeability of the structure is close to zero [71]. The training dataset has been generated through Finite Element Method (FEM) based EM simulation tool for an $n \times n$ metamaterial structure. The MTM unit cell consists of a set of metallic lines printed on Rogers 4003 substrate with thickness of 0.8 mm and relative permittivity $\epsilon_r = 3.55$. A set of design parameters (a, b, c, w, g_x and g_y) of the unit cell allow us to design a metamaterial with a very small loss in the desired frequency region. A floquet port unit cell setup with periodic boundaries to its four lateral (or in-plane) walls are set to simulate the incident plane. The scattering parameters are calculated with simulation tool and the effective material parameter at certain frequency are extracted with the procedure presented in [74].

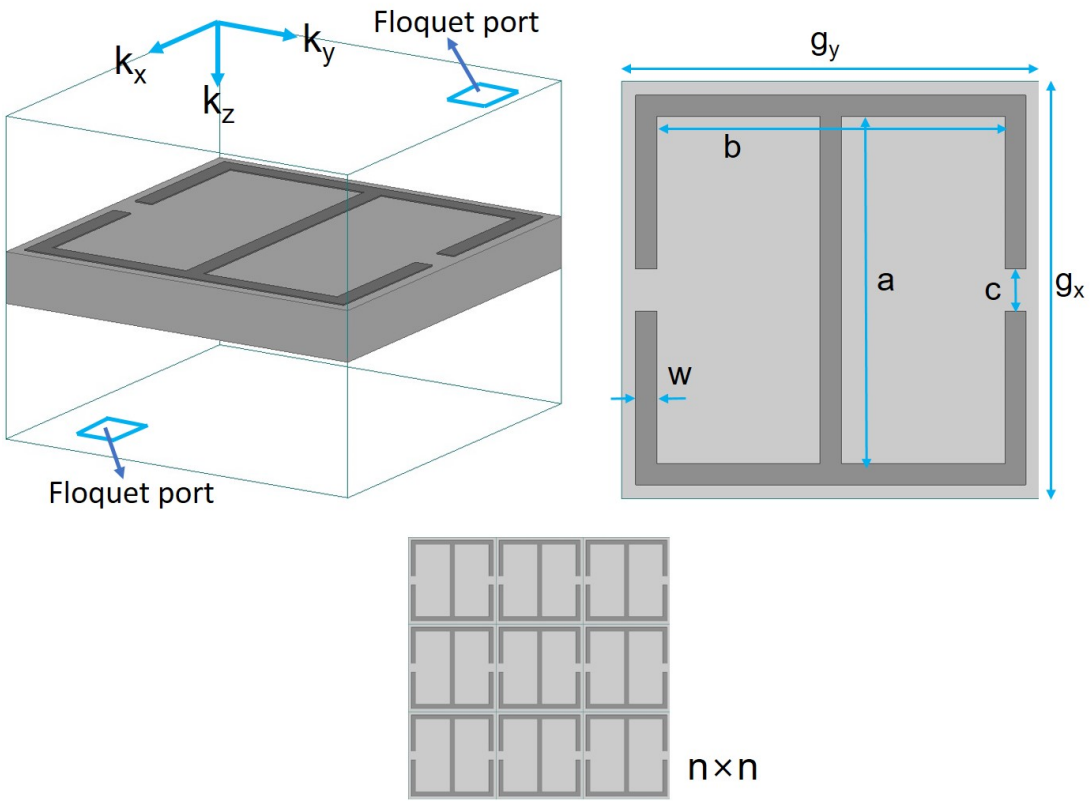

(a)

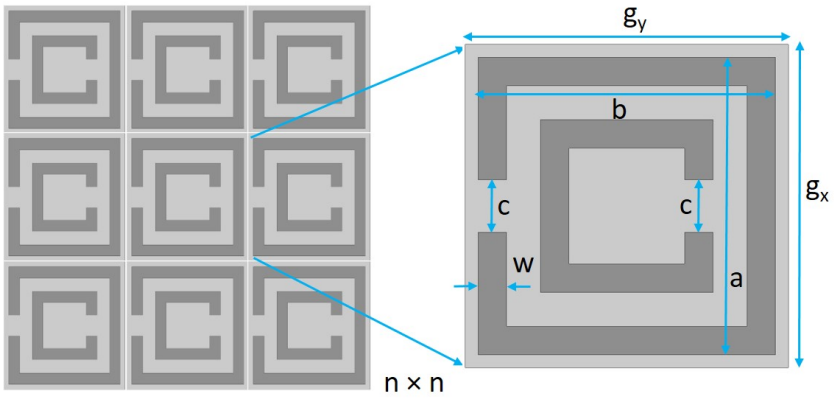

(b)

Figure 4.1: A schematic diagram of $n \times n$ MTM prototypes with notations a = b = x_i^1, c = x_i^2, $g_x = g_y = x_i^3$, w = x_i^4 for $i = N$ number of input dataset, (a) EM structure I (b) EM structure II, x varies with a by taking fixed t value between two rings.

Electromagnetic design complex

We randomly sample some rows from our simulation dataset as shown in Fig. 4.2. The data rows are then encoded as fully statistical simplicial complex called Statistical Clique which we call as Electromagnetic Design Complex $EDgn$. We define the statistical clique as a collection of data points, that lies within a ball of radius of ϵ, such that the probability of euclidean distance (ED) less than $2\epsilon \sin(\frac{\pi}{n})$, is sufficiently large [75]. Here n is the dimension of the clique and the global shape of the data points is a clique. The simulation dataset is a two dimensional matrix and each data row (from simulation) is encoded as a vertex in our $EDgn$, as shown in Fig. 4.2. Our proposed $EDgn$ captures structural and statistical correlations between our input geometric data (a, b, c, w, g_x, and g_y) with output f_r = frequency and μ_{eff} = effective permeability.

Bayesian clique learning

The hypothesis space which encodes the functional relationships between input-output solely based on EM data, is an infinite dimensional space. Our proposed BCL uses statistical clique embedded in the data for searching optimum design parameters [76–79]. We build our statistical clique purely based on the ED, though other forms of information theoretic metric are also used [80]. The uncertainty of the noise model in the simulation data is not inhibitive to BCL, though we have used gaussian noise in our model for computing optimum hypothesis h_{ML}. The mean-squared error MSE, is used as a metric to search the h_{ML} in the space of hypotheses. Formally the hypothesis space is defined as:

$$H = \{(a, c, g_x, w) \quad | \quad (a, c, g_x, w) \in R^4\} \tag{4.1}$$

where the $4-$tuple (a, c, g_x, w) is the input geometric parameters for the EM structure. The optimum hypothesis h_{ML} by our BCL is given by:

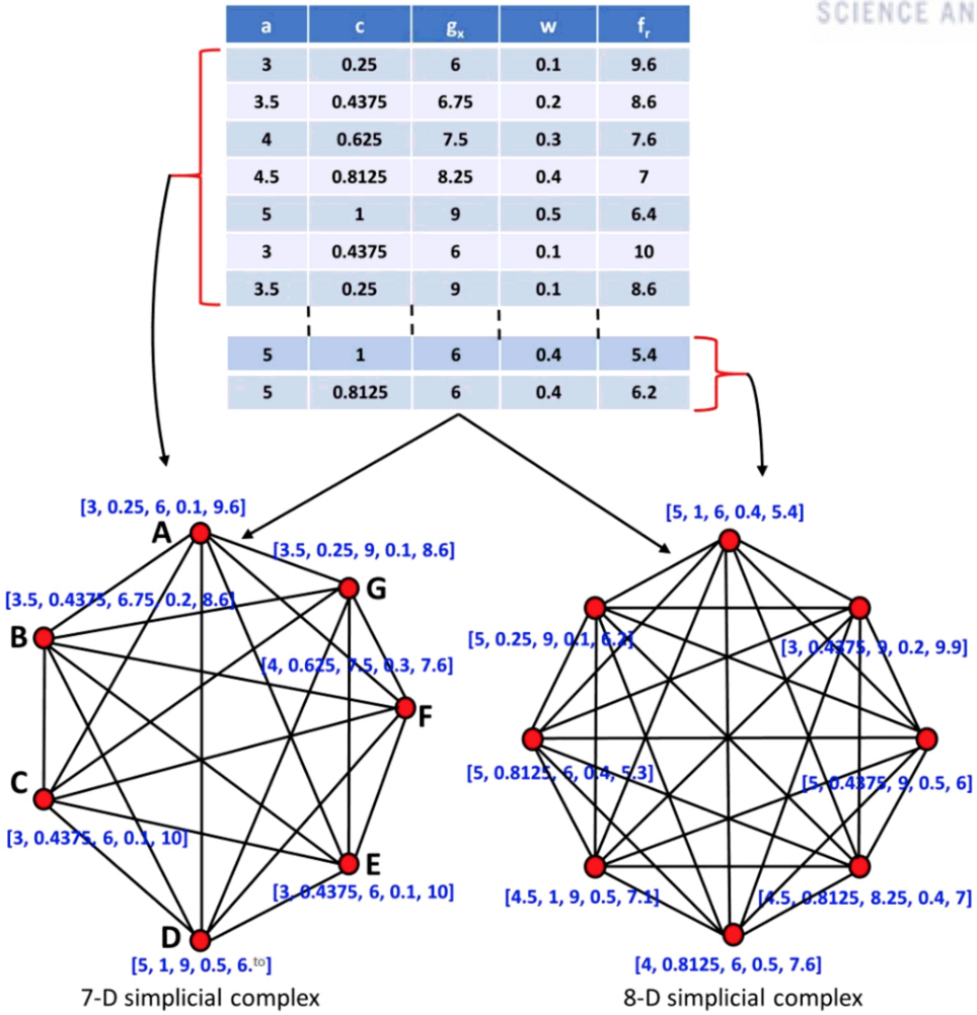

Figure 4.2: Electromagnetic design complex

$$
\begin{aligned}
h_{ML} &= \text{argmax } P(D, C \mid h) \\
&= \text{argmax } \prod_{i=1}^{N} \frac{1}{\sqrt{2\pi\sigma^2}} e^{-\frac{1}{2}\frac{(d_i - h(x_i^L))^2}{\sigma^2}} \\
&\approx \text{argmin } \sum_{i=1}^{N} (d_i - h(x_i^L))^2
\end{aligned}
\tag{4.2}
$$

where D is data set, σ is standard noise, C is the embedded statistical clique, N is the number of samples data, d_i is i^{th} frequency or permeability, $h(x_i^L)$ is the kernel function on the input geometric data x_i^L. The EM dataset clustered into two groups (with centroids 0 and 1) by $K-$means and we chose the densest cluster. We check, whether the conditions

of formation of statistical clique satisfies in the densest cluster, else we move to the other cluster and choose the best statistical clique. This cut downs our searching space though it incurs some information loss as given by Eq. 4.2.

4.1.2 Computational complexity

The simulation run by our EM simulation tool use finite element method (FEM). The input data for full-wave EM simulation tool includes formation of finite element mesh. The computation complexity increases dramatically with mesh size and the number of input state variables, which is tackled by mesh refinement [81]. Our algorithm reduces the mesh generation complexity by dividing in K clusters and building the statistical clique. The statistical clique can be dynamically changed by setting the euclidean distance threshold appropriately. We denote banded stiffness matrix with bandwidth W, number of nodes N, and the number of elements E, M is the mesh input [82, 83]. The FEM is basically solved in three stages: (i) formation of global matrices (ii) matrix modification to include nodal values (iii) solving system of equations. The asymptotic complexity for FEM algorithm is computed as the sum of all complexities of the above three stages along with the mesh generations. The computational speed-up by our algorithm approximately is $\mathcal{O}(\frac{M}{K \times s \times t_{dist})})$, where $\mathcal{O}(E)$ is mesh generation complexity, K is the number of clusters, s is the sample size, t_{dist} is the time to compute pairwise distance. Our algorithm reduces the simulation time of EM simulator and computational complexity C given by:

$$\begin{aligned} C = \mathcal{O}(E) + \mathcal{O}(NW) + \mathcal{O} + (NW^2) + \mathcal{O}(NW) \\ + \mathcal{O}(\frac{M}{K \times s \times t_{dist})}) \end{aligned} \tag{4.3}$$

The reduction of computational complexity comes at the expense of increasing the uncertainty. The upper bound in uncertainty is

$$\begin{aligned} \delta^2 &= \frac{1}{N} \sum_{i=1}^{N} \left\{ d_i - h(x_i^L) \right\}^2 \\ &\leq \lambda \sum ||x_i^L - \mu_i||^2 \end{aligned} \tag{4.4}$$

where λ is the constant that depends on geometry of data, number of clusters and entropy. The algorithm we have used in our paper is :

Algorithm 1 Bayesian Clique Learning

1: **Input:** Random Sample Rows
2: **Output:** Optimum Design Parameter
3: Divide Data Set in (i) High Frequency/High Permeability (ii) Mid Frequency/Mid Permeability (iii) Low Frequency/Low Permeability
4: Set the Euclidean threshold ϵ_{th}
5: Clustering each data using K-Means (2-cluster) using ϵ_{th}
6: Take the majority cluster
7: Build the statistical clique with threshold $\epsilon_{th} \leq \epsilon$
8: Compute the maximum likelihood hypothesis h_{ML} by Bayesian method

4.1.3 Results and discussions

The data set from EM simulation tool is a two-dimensional array of 619−rows and 5−columns. We find our optimum design hypothesis h_{ML} by using automatic statistician of various non-normalized kernel functions (Linear (Lin), Rational Quadratic (RQ), Cosine, Sine, Periodic (PER) and Squared Error (SE) etc.) and comparing the MSE. Fig. [4.3, 4.4, 4.5] and Fig. [4.6, 4.7, 4.8] show the MSE values and our bayesian clique learning BCL, output results for three ranges (high, mid, low) of frequency f_r, and permeability μ_{eff}, for 20 input samples of EM structure I. The h_{ML} for all three ranges of frequency and permeability comes out to be periodic (PER) non-normalized kernel function. The minimum MSE values for high, mid and low range of frequencies are 0.02, 0.03 and 0.05 respectively, and for permeability the MSE values are 0.0008, 0.0007, 0.005. The real EM simulation data is matching well with our BCL output. The largest error for three ranges of frequency and permeability values are 0.02 and 0.009 respectively, as shown in Fig. [4.3-4.8]. In Fig. [4.7, 4.8] (b), the BCL output (o/p) of permeability for 20^{th} training sample data set, exceeds from our usual range. This anomalous behavior shows our bayesian clique learning are not tuned properly for some dataset. This is because of the unusual behavior of our 5−dimensional noise. Fig. [4.9] show the MSE value (0.05) and our BCL, output result for high range of frequency f_r for EM structure II. The permissible range of error values justifies the convergence of our learning algorithm. We compare and

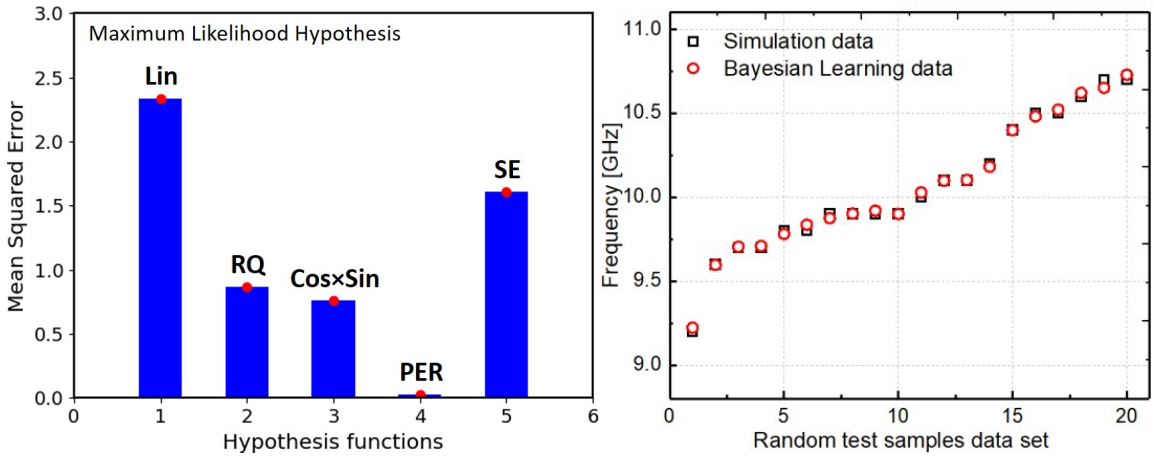

Figure 4.3: For f_r of EM structure I (a) MSE for high f_r range (b) M.L. o/p and simulated results for topmost samples (x_i^L).

study the dataset of two different EM structures that are weakly negatively correlated as shown Fig. 4.10. The $x-$axis is the distance ϵ between any two neighboring nodes of our statistical clique and $y-$axis is the number of neighboring nodes. The normalized mutual information, adjusted mutual information, correlation coefficient between the datasets are 0.820328868986, 0.214608185067 and -0.09756498 respectively as shown in Fig. 4.10. As the distribution of two datasets are different, the euclidean distance threshold (0.3 for EM structure I, 0.5 for EM structure II approximately), for these datasets are different. The euclidean threshold is the maximum cutoff, in the $x-$axis, beyond which the probability of getting statistical cliques are low. The added complexity advantage for the second EM structure comes at the expense of information loss.

4.2 Inverse design of EM structure with deep learning

Design of electromagnetic metamaterial structures have relied on expert circuit designers by doing numerous electromagnetic simulations, which can be prohibitively time consuming. Inverse problem proceeds in the opposite direction of designing metamaterial geometry parameters from the characteristics of the desired output. We have proposed a novel machine learning method that bypasses the conventional design method for given output by

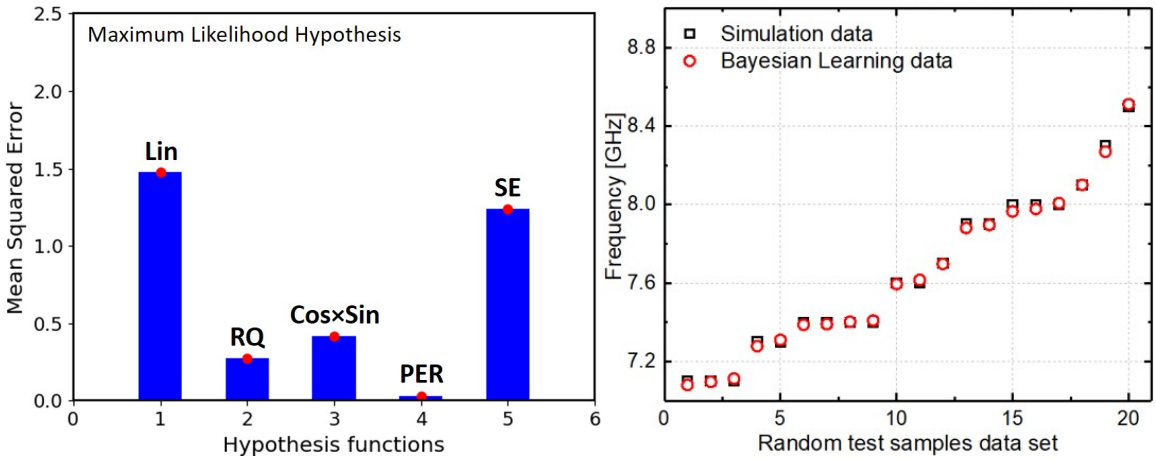

Figure 4.4: For f_r of EM structure I (a) MSE for mid f_r range (b) M.L. o/p and simulated results for topmost samples (x_i^L).

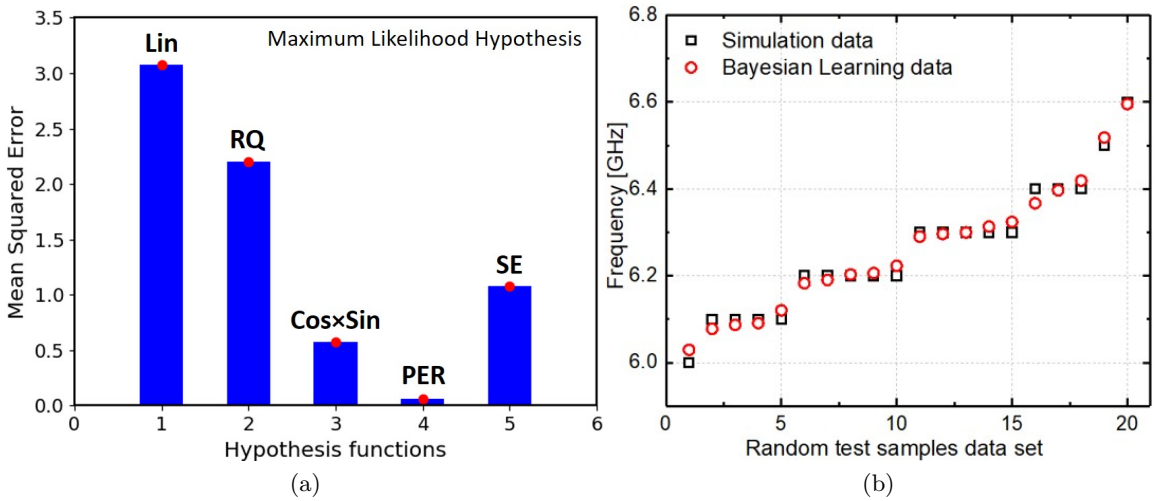

Figure 4.5: For f_r of EM structure I (a) MSE for low f_r range (b) M.L. o/p and simulated results for topmost samples (x_i^L).

means of a Lifelong Learning Architecture (LLA). LLA learning architecture is basically a large-scale coupled training architecture, in which multiple predictions and classifications are done simultaneously. LLA model is trained in a supervised manner by using higher order logic. The higher order logic is derived from intra-tasks results, common Knowledge Base (KB), and coupling constraints.

The search space of geometry parameters is highly irregular and not amenable to exact optimization techniques and random search procedures are employed as shown in Fig. 4.11.

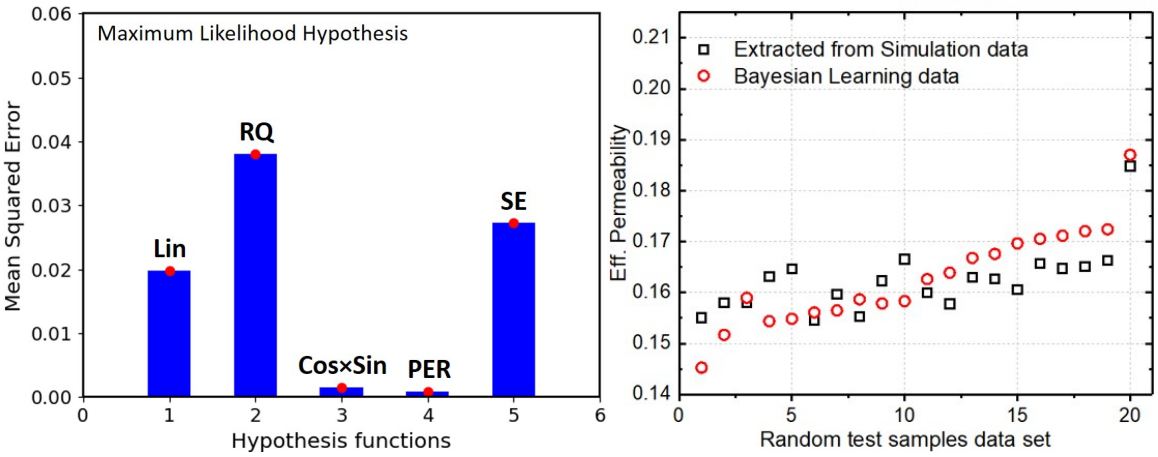

(a) (b)

Figure 4.6: For μ_{eff} of EM structure I (a) MSE for high μ_{eff} range (b) M.L. o/p and simulated results for topmost samples (x_i^L), $f_r = 10$ GHz.

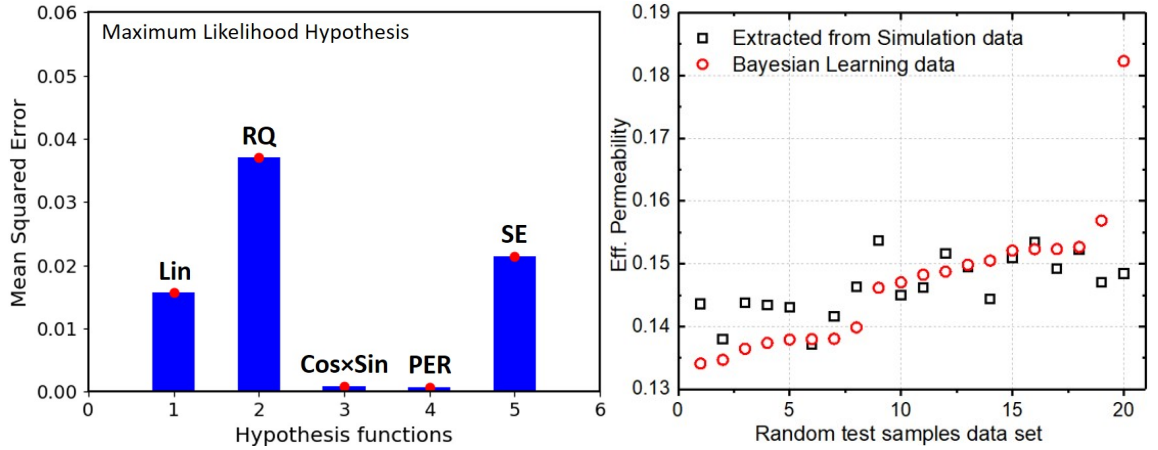

(a) (b)

Figure 4.7: For μ_{eff} of EM structure I (a) MSE for mid μ_{eff} range (b) M.L. o/p and simulated results for topmost samples (x_i^L), $f_r = 10$ GHz.

Most random search procedures are agnostic with respect to transformation kernel and require only that it to be ergodic. One possible way of attacking this irregular space is to use Markov Chain Monte Carlo (MCMC) sampling.

4.2.1 Prior work on inverse design

The classical method to solve inverse problems starts with an analytical description $F : X \to Y$ of the forward operator in some Banach spaces X and Y. The primary target in

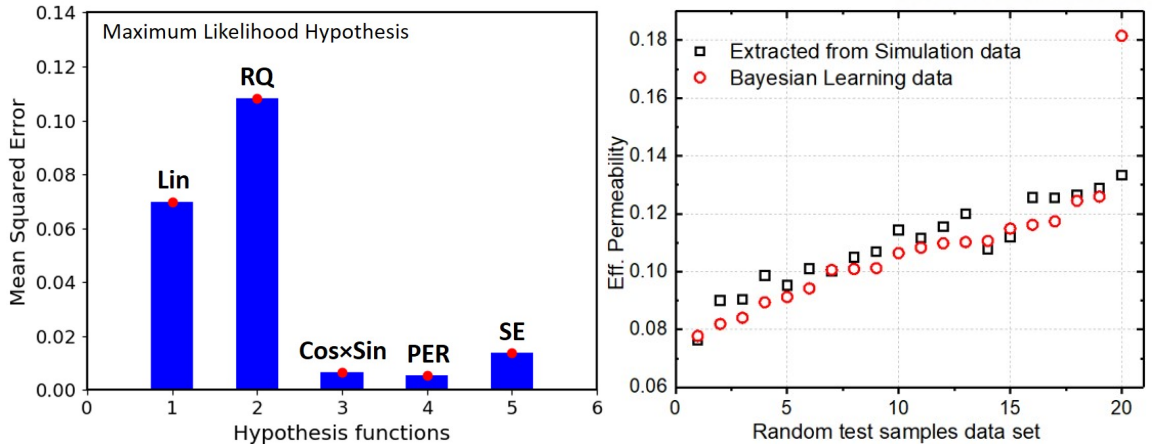

(a) (b)

Figure 4.8: For μ_{eff} of EM structure I (a) MSE for low μ_{eff} range (b) M.L. o/p and simulated results for topmost samples (x_i^L), $f_r = 10$ GHz.

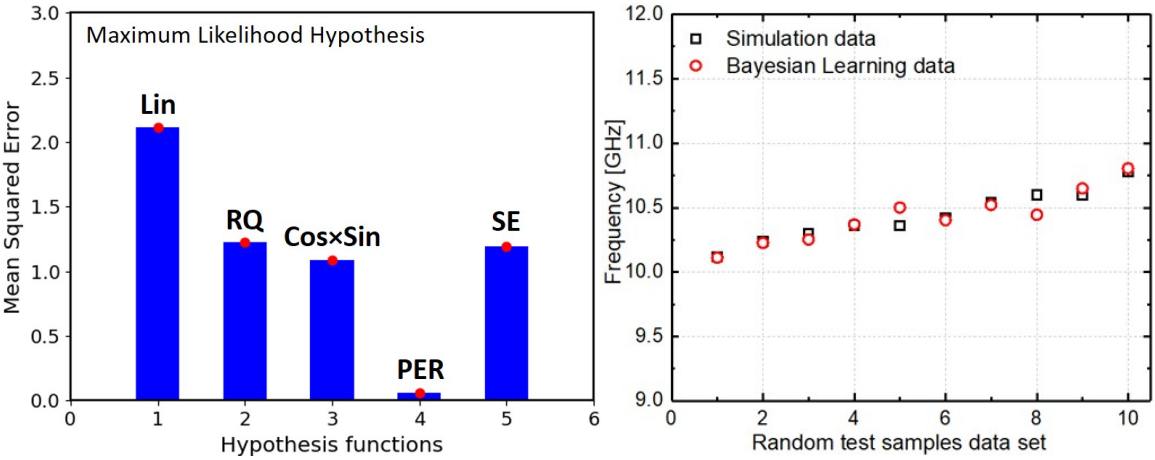

(a) (b)

Figure 4.9: For f_r of EM structure II (a) MSE for high f_r range (b) M.L. o/p and simulated results for topmost samples (x_i^L).

inverse problems is to reconstruct an unknown x from given noisy data $y^\dagger$ $F(x)$, where the generalized inverse F^1 is unbounded. Analytic models are typically just an crude approximation to the real application and their extension are often restricted due to the high degree of complexity or an only partial window to understand the underlying physical processes. Also, the input space of many real applications like microwave circuit design will be just a subspace of the whole function space X and follows an unknown stochastic distribution. Machine learning provides data-driven approaches to tackle these hard problems by using

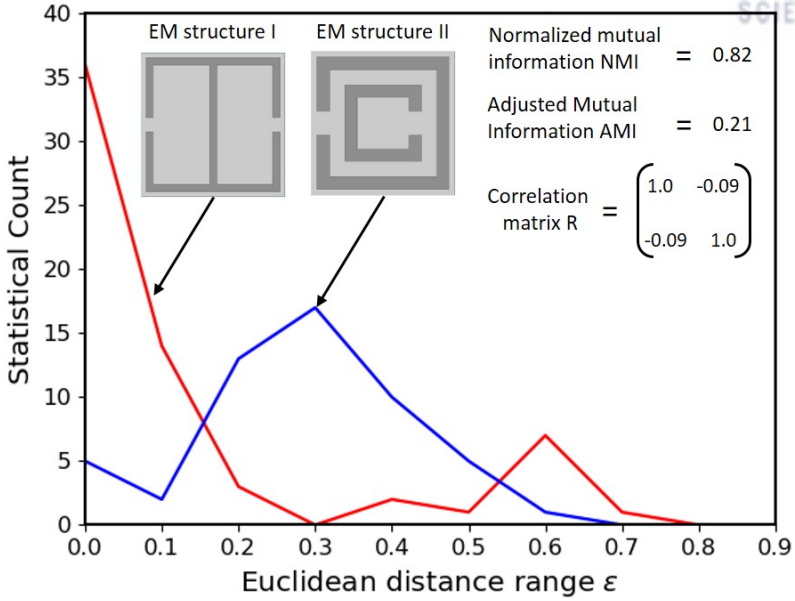

Figure 4.10: Correlation between two EM structures.

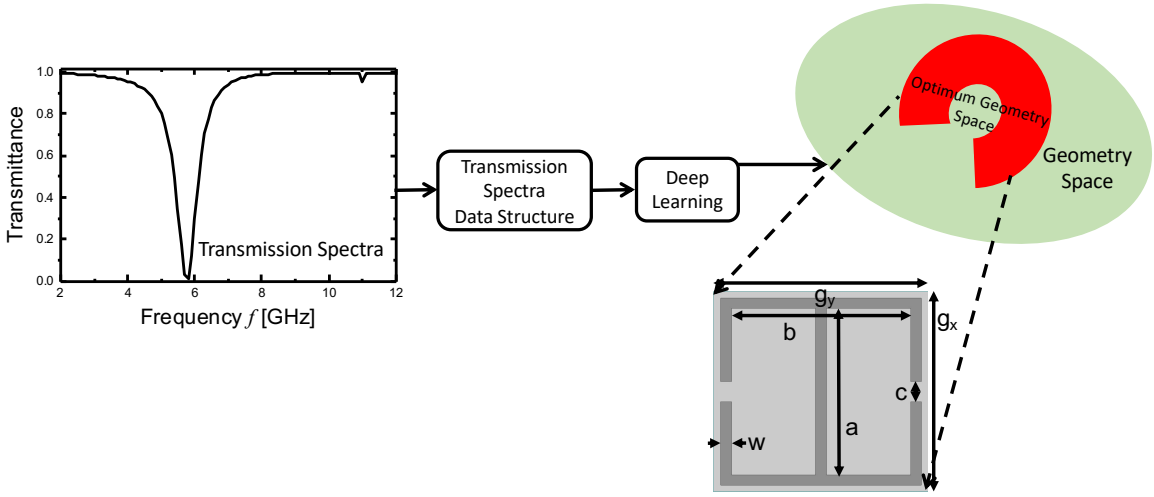

Figure 4.11: Searching in high dimensional geometry space.

training data sets to either construct a problem adapted forward operator and use an established inversion method or to solve the inverse problem directly. Particularly deep learning approaches using neural networks with multiple hidden layers have become popular recently. However, no consistent theoretical framework on deep neural networks for inverse problems has been developed yet besides the breakthrough results, which have been published so far for many different types of applications to inverse problems. The recent research thrust is the interpretation of the different layers of a neural network as discretization of continuous

systems like ordinary differential equations (ODEs), partial differential equations (PDEs) and integro-differential equations.

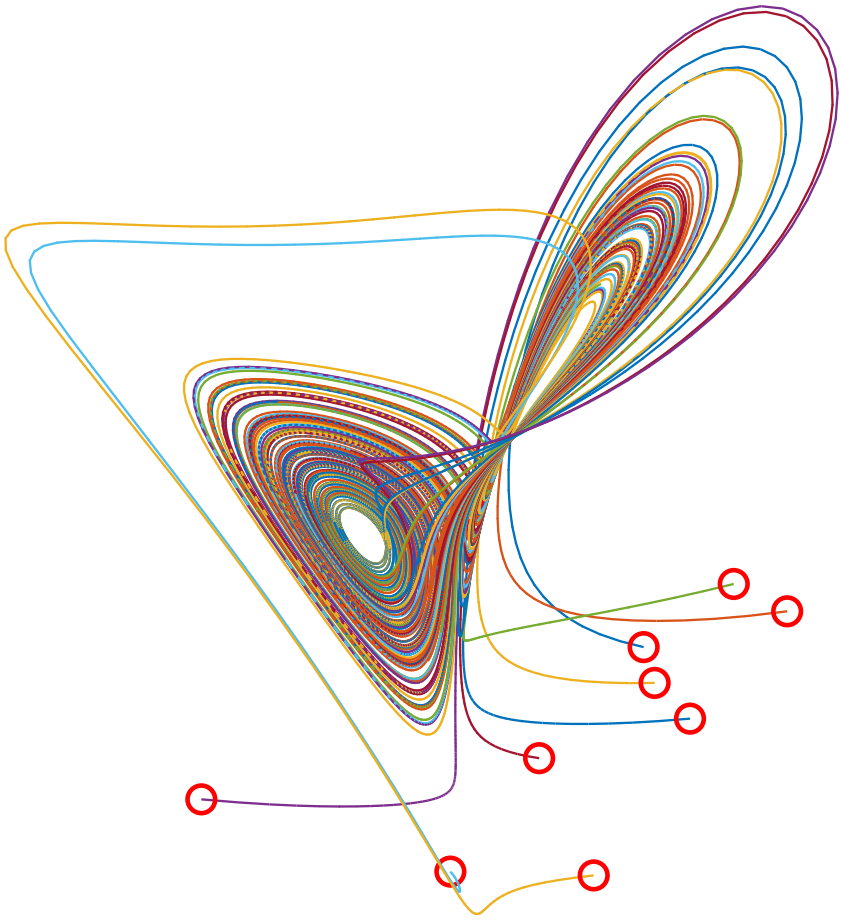

Figure 4.12: Neural ordinary differential equation (ODE).

These innovative approaches allow us to address the stability of neural networks and it allows us to develop novel network designs based on classical discretization schemes for inverse problems. The continuous framework results in a new understanding of the concepts of layers as time discretization points. The conjecture is that the PDE-motivated networks after suitable discretization - help enforce stability as shown in Fig. 4.12. Optimization of neural networks by using a functional analytical network for e.g. optimizing activation functions or regularization scheme is another active of research. The interpretation of Tikhonov regularization for inverse problems can be interpreted as by the design of the neural network. Another source for tackling deep neural networks is through harmonic analysis as a concept for detecting invariants in large data sets and for interpretation on

neural network behaviour in general. Inverse problem falls in the category of ill-posed problem. Inverse problem solvers minimize a cost function along with with a regularizer, that reflects prior knowledge. Recent trends in machine learning have shown the possibility to learn a regularizer from training data. Regularization is a classical technique for dealing with ill-posed inverse problems; it has been used successfully for wide range of applications. The other important direction to solve the inverse problem of designing neural network inspired by a Neumann series, called Neumann network. Instead of unrolling an iterative optimization algorithm, Neumann series is truncated, which then directly solves inverse problem with a data-driven nonlinear regularizer. Neumann network approximates the optimal oracle estimator for the inverse problem. The theoretical area of interest is the expressibility of sparsely connected deep neural networks for inverse design. The empirical belief is: more neurons, edges, and layers are available, the more the approximation power a.k.a expressiblity. Hence it is of interest to consider this for a restricted number of edges or layers (sparse deep neural networks) for solving the inverse problem as shown in Fig. 4.13. Such sparse neural networks are of extreme interest from the point of view of computational efficiency and memory requirements.

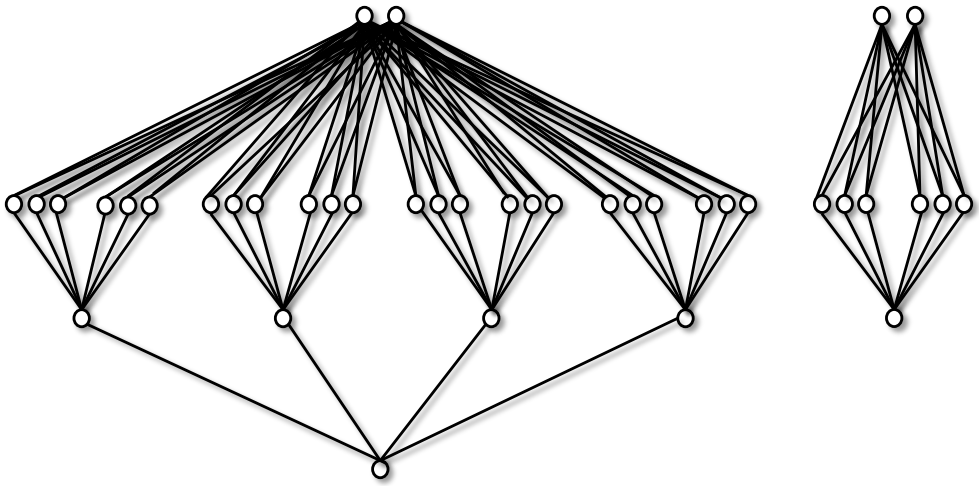

Figure 4.13: Sparse neural network for inverse design.

Recently Network Tikhonov (NETT) (in Fig. 4.14) is proposed to solve inverse problems. NETT considers regularized solutions of small value of a regularizer computed by a trained

neural network. NETT regularization enforces data consistency for the unknown to be recovered.

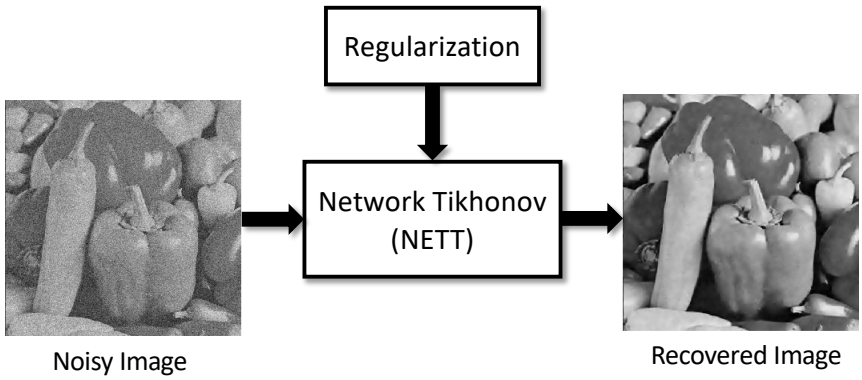

Figure 4.14: Network Tikhonov.

This method is of great use in case the unknown to be recovered is not sufficiently similar to available training data as shown in Fig. 4.15. The network has the form of an auto-encoder, with an encoder, a decoder and atleast one hidden layer [88]. On the practical note, generative adversarial networks (GANs) are used for the inverse design of metamaterial structure as shown in Fig. 4.16. The metasurface design process is innately complex and requires human expertise. Also the initial design realized is based on physics knowledge and intuitive reasoning, whereas geometric and material parameters are achieved by means of trial-and-error. Thus the design of metasurface requires an expert knowledge base of optics with iterative simulations for searching multidimensional parameter spaces. This work uses deep neural networks to approximate the spectra of a metasurface and generate metasurface patterns using GANs. The metasurface patterns is the goal of inverse optical design. By doing so, the need for extensive parameter search or trial-and-error procedures are avoided. Multiple solutions of metasurface design may exist for the same target spectrum as this is an ill-posed problem [89].

4.2.2 Theoretical setting of inverse problem

Let X and Y be Banach spaces over R or C and let $F : X \supseteq \mathbb{D}(F) \to Y$ be a mapping between them with domain $\mathbb{D}(F)$. We solve equations as:

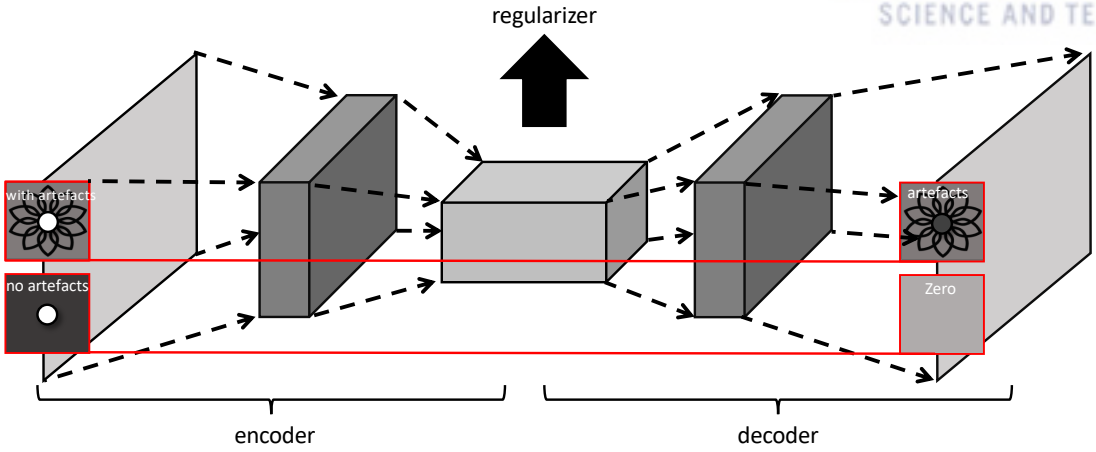

Figure 4.15: Network Tikhonov encoder-decoder.

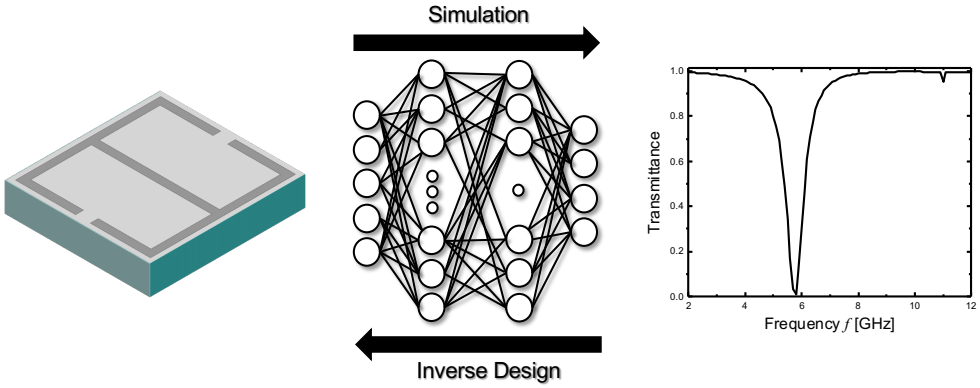

Figure 4.16: Generative adversarial networks (GANs) for inverse design.

$$F(x) = y^{\dagger}, \quad x \in \mathbb{D}(F) \tag{4.5}$$

with precise and attainable data $y^{\dagger}$ in Y. Solving the above equation requires, intuitively, inversion of F. Generally, an equation is called ill-posed if the inversion process is very sensitive to perturbations in the right-hand side $y^{\dagger}$. Such perturbations are difficult avoid in practice because$y^{\dagger}$ represents some measured quantity and measurements always are corrupted by noise. Ill-posed inverse problems are frequently divided into two categories: linear and nonlinear. They are classified as linear inverse problem if there is a closed theory of regularization and nonlinear if weak theoretical regularization results are available.

4.2.3 Artificial general intelligence as multi-tasking

The measure of intelligence is the ability of an agent to perform in many different environments as shown in Fig. 4.17. As there are an infinite number of environments, we take a weighted sum of these environments. From the agent's perspective there exists a probability measure that describes the true environment, but this measure is not known to the agent. The information the agent gathers are some its past observations of the environment. Then the agent constructs a list of probability measures that are aligned with its observations. This is potential explanations of the actual environment, hypotheses. The basic agent-environment framework consists of: (i) an agent (ii) environments (iii) goals as shown in Fig. 4.18.

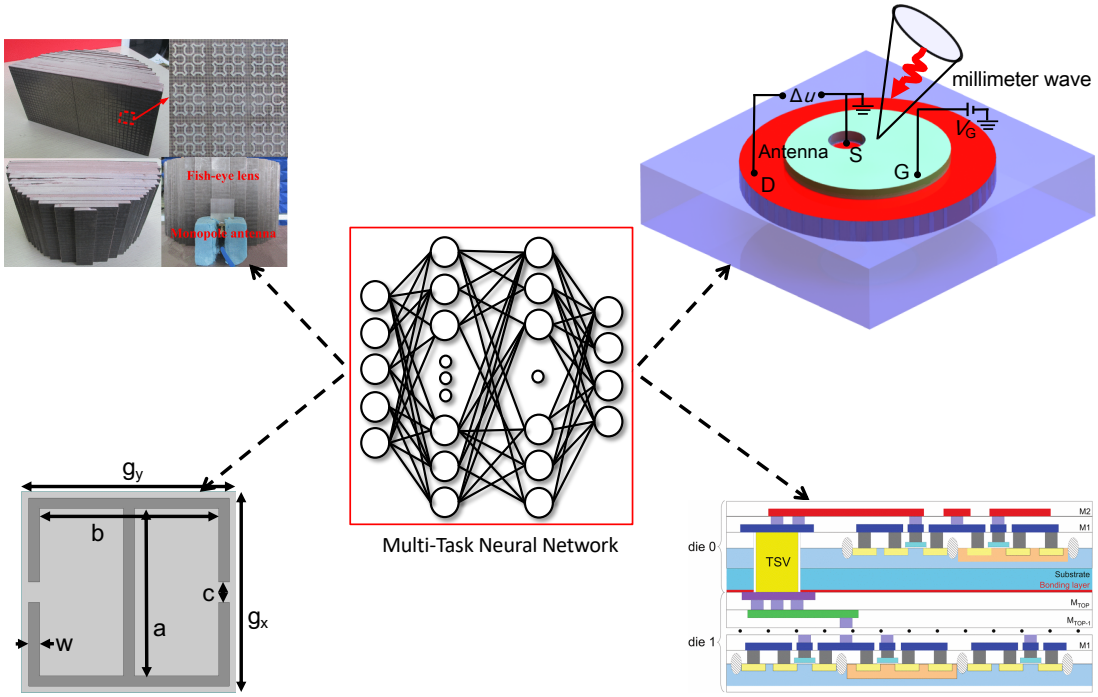

Figure 4.17: Multitasking neural network.

The agent and the environment interact with each other and the agent send signals to the environment and also receive signals from the environment. The agent's intelligence is thus measured as some kind of goal it tries to achieve. Formally agent sends information to the environment by sending symbols from some finite alphabet as:

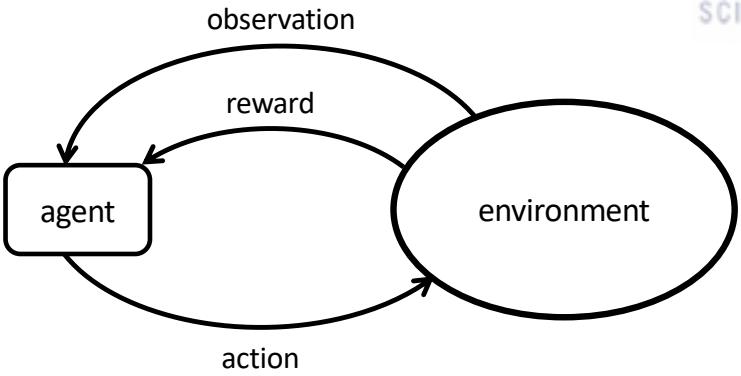

Figure 4.18: Agent-environment framework.

$$A := \{\text{left}, \text{right}, \text{up}, \text{down}\} \tag{4.6}$$

We called A action space and similarly environment sends signals to the agent with symbols from the perception space P. The reward space, denoted by R, denoted as:

$$R := [0, 1] \cap \mathbb{Q} \tag{4.7}$$

The agent is a function, that takes the current history as input and chooses the next action as output. The expected future value for an agent and environment interacting, by taking the sum of these discounted rewards into the infinite future as:

$$V_{\mu}^{\pi}(\gamma) = \frac{1}{\Gamma} E\left(\sum_{i=1}^{\infty} \gamma^i r_i\right) \tag{4.8}$$

where r_i is the reward in cycle i of a given history γ is the discount rate, γ^i is the discount applied to the i^{th} reward into the future, the normalising constant is:

$$\Gamma = \sum_{i}^{\infty} \gamma^i \tag{4.9}$$

and the expected value is taken over all possible interaction sequences between the agent π and the environment μ.

4.2.4 Proposed method for inverse design

We formalize our inverse learning problem as a multi-tasking learning problem as explained in the previous section. We have exploited redundantly predictive features of frequency data by coupled training [84–87,91]. For each inverse prediction task i we learn the function $f^i(x)$ that maps from the 101-dimensional frequency characteristics $\chi^i \subseteq \mathbb{R}^{101}$ to 4-dimensional geometry $Y^i \subseteq \mathbb{R}^4 (y^i \in Y^i)$. The multi-task loss functions $\mathcal{L}$ (e.g., mean squared error, categorical cross entropy), are minimized as [87]:

$$\sum \sum \mathcal{L}(f^i(x), y^i). \tag{4.10}$$

In our learning framework the agent faces an environment consists of a collection of learning tasks, and constraints that couple their solutions. We define our learning problem as an ordered pair consisting of: (i) a set $L = \{L_i\}$ of learning tasks (ii) i^{th} learning task $L_i =< T_i, P_i, E_i > P_i$ performance metric, T_i task, E_i experience (iii) a set of coupling constraints $C = \{< \phi_k, V_k >\}$ where ϕ_k is a real-valued function over two or more learning tasks, and V_k is a vector of indices over learning tasks. Our learning architecture learns from a modified expectation–maximization (EM) algorithm where the tasks are loosely coupled [87]. In the E-like step, beliefs are updated and stored in the knowledge base (KB), and in the M-like step, this updated KB is used for retraining and inference as explained in Algorithm Section. This gives a coupled training system through a shared Knowledge Base (KB) and coupling constraints.

We have applied the above learning method for the inverse design of a metamaterial structure (in Fig 4.19) based on the desired set of frequency characteristics. However, achieving the desired frequency sweep can be difficult and time consuming. Therefore, we have developed an inverse design approach that searches appropriate geometric values of transmission lines based on the required transmission characteristics. Our inverse design model is trained with 101-dimensional input of transmission-characteristics data and 4-dimensional output geometry of structure length a, gap width c, substrate length g_x, and line thickness w [84–87, 91]

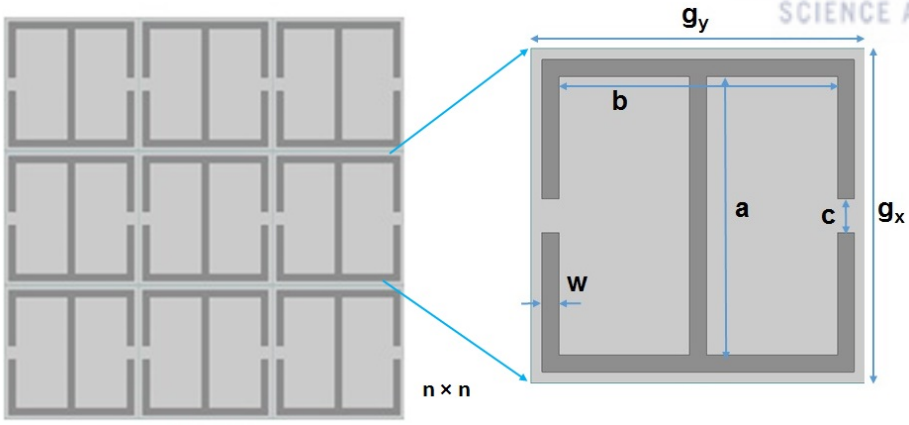

Figure 4.19: A schematic diagram of $n \times n$ MTM prototype with notations (a) structure length $a = b$ (b) gap width c (c) substrate length $g_x = g_y$ (d) line thickness w

We have used multi-tasking learning paradigm and train our deep learning model jointly for prediction (by regression) and classification Fig. 4.20. The classification problem is artificially induced, where we discretize the geometry parameters a, c, g_x and w in 10 different classes (class-0, ..., class-9). The distribution of geometry parameters are uniformly distributed between their minimum and maximum values such as $a \in [3.001, 5.7486], mm$, $c \in [0.100, 1.15], mm$, $g_x \in [6.0, 8.9], mm$ and $w \in [0.100, 0.45] mm$, respectively. We train our model with 3786 input samples of transmission-characteristics and output geometry. We have tested our Lifelong Learning model on 50 unseen samples of data.

Inverse design algorithm analysis

The Expectation-Maximization (EM) algorithm is a way to find maximum-likelihood estimates for model parameters when the data is incomplete, has hidden latent variables as shown in Fig. 4.21. The maximum likelihood estimation find the "best fit" model for a set of data points.

Some variants of complex Expectation-Maximisation algorithm find model parameters even from missing data. It works, first choosing random values for the missing data points, and using those guesses to estimate a second set of data. Then these new values are used to create a better guess for the first set, and the process continues until the algorithm converges on a fixed point.

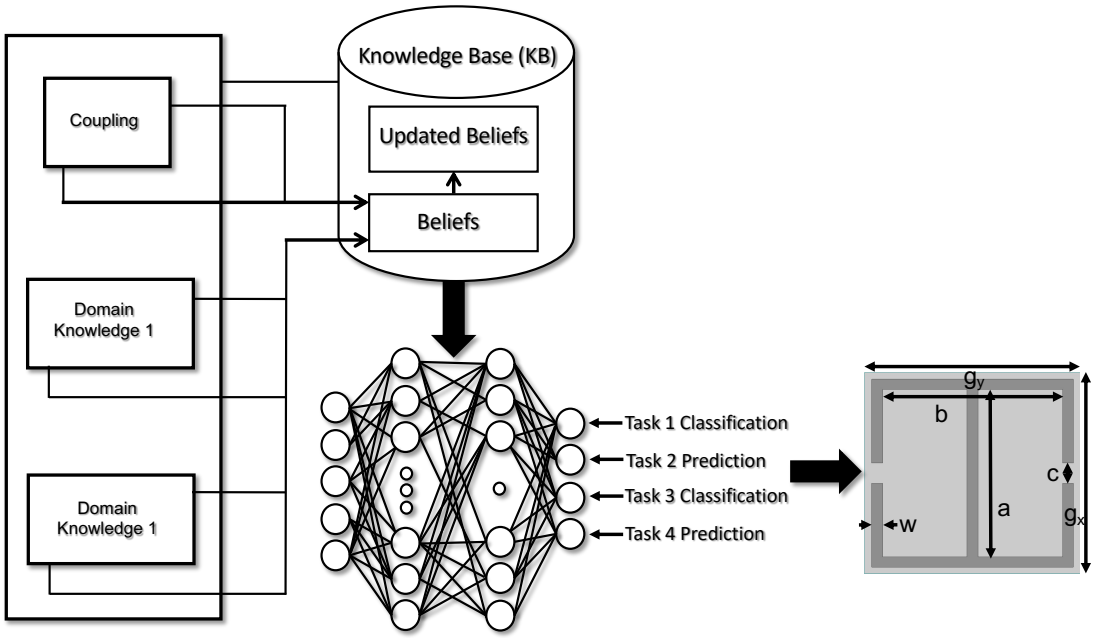

Figure 4.20: Multi-tasking neural network for inverse design.

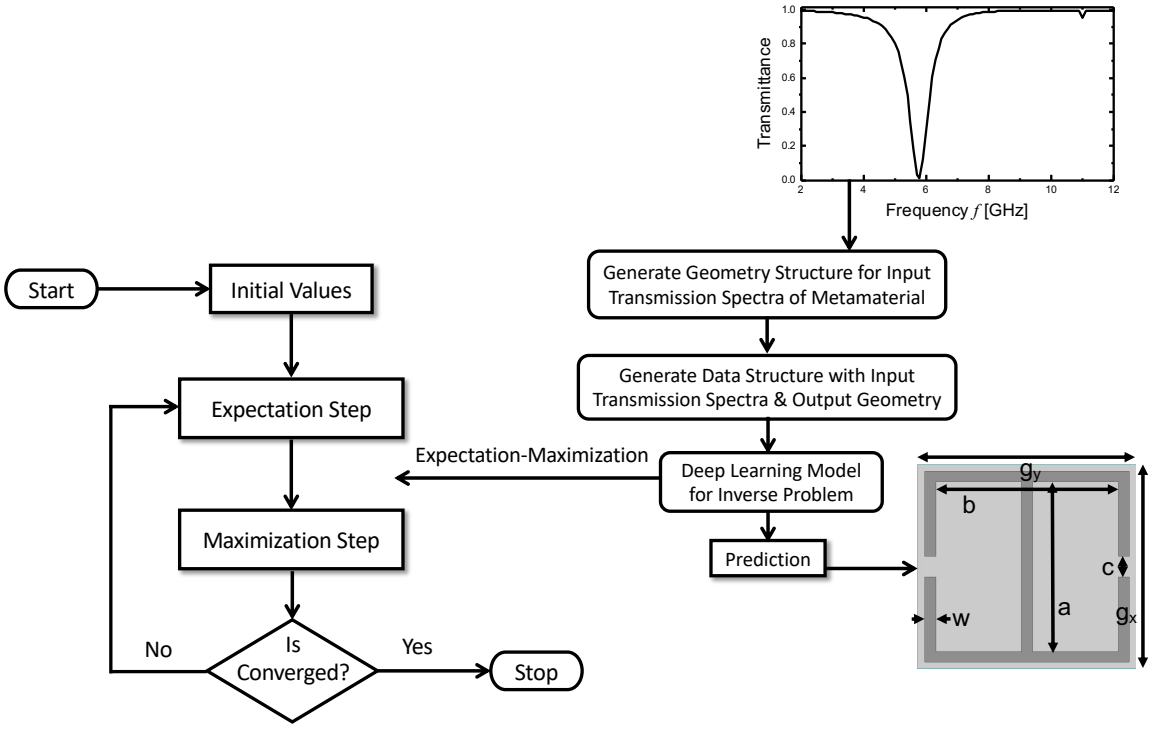

Figure 4.21: Expectation-Maximisation algorithm for inverse design.

Algorithm 2 Expectation-Maximisation algorithm for inverse design

```
belief b_i, i index, N constant
procedure E-STEP(b_i updated)
    while n <= N do
        Compute the likelihood of belief b_i
        Store the belief b_i in KB
        Retrain with updated belief
        i = i + 1
    M-step b_i for retraining
```

Results and analysis

To evaluate the proposed approach, we have considered a metamaterial structure. We have validated our inverse design via the scatter plots as shown in Fig. 4.23 and the system performance parameters are shown in Table 4.1. We have plotted the histograms of the transmission-characteristics as shown in Fig. 4.22. We plot our machine learning predicted geometry parameters versus experimental geometry of a, c, g_x and w used in the corresponding simulation of channel and we compute the root mean square error as shown in Table 4.1. The observed mismatch is partly due to the estimated function being *non-injective* (different geometry configurations map to the same transmission characteristics). The mismatch increases when the same output maps to several possible inputs.

Table 4.1: System performance parameters for inverse design

Geometry Parameter	Error	Epochs	Batch Size
Structure length a	0.153	900	25
Gap width c	0.164	900	25
Substrate length g_x	0.610	900	25
Line thickness w	0.078	900	25

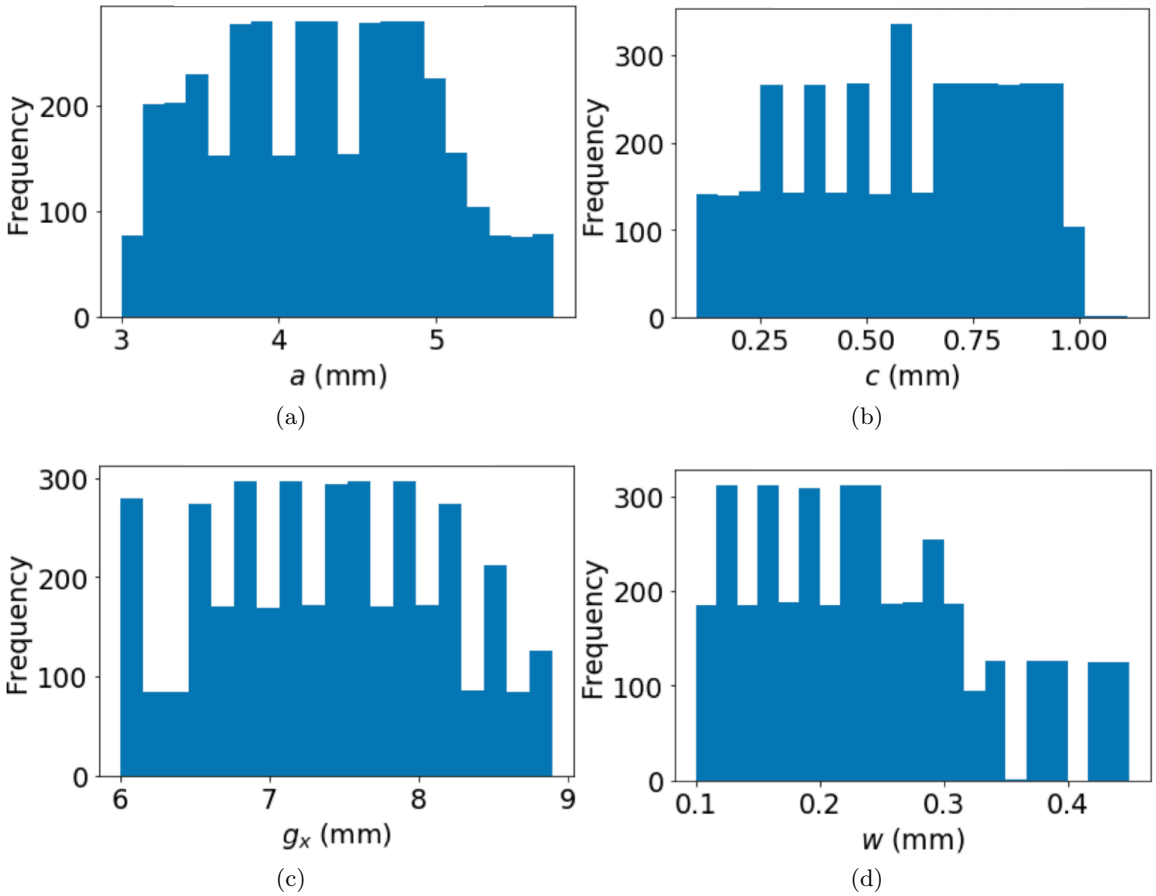

Figure 4.22: Histogram training geometry parameter plots of $n \times n$ metamaterial prototype structure. (a) structure length a (b) gap width c (c) substrate length g_x (d) line thickness w.

4.3 Inverse design of transistor-antenna through Deep Learning

We have applied the proposed approach given in 4.2 for the inverse design of $n \times n$ transistor-antenna structure (in Fig. 4.24) based on the desired set of absorptance characteristics. The inverse design model is trained with 151-dimensional input of absorptance-characteristics data and 3-dimensional output substrate and geometry parameter of substrate relative permittivity ϵ_r, dielectric thickness t_{Si}, and drain radius r_{dr}. The distribution of geometry parameters are uniformly distributed between their minimum and maximum values such as

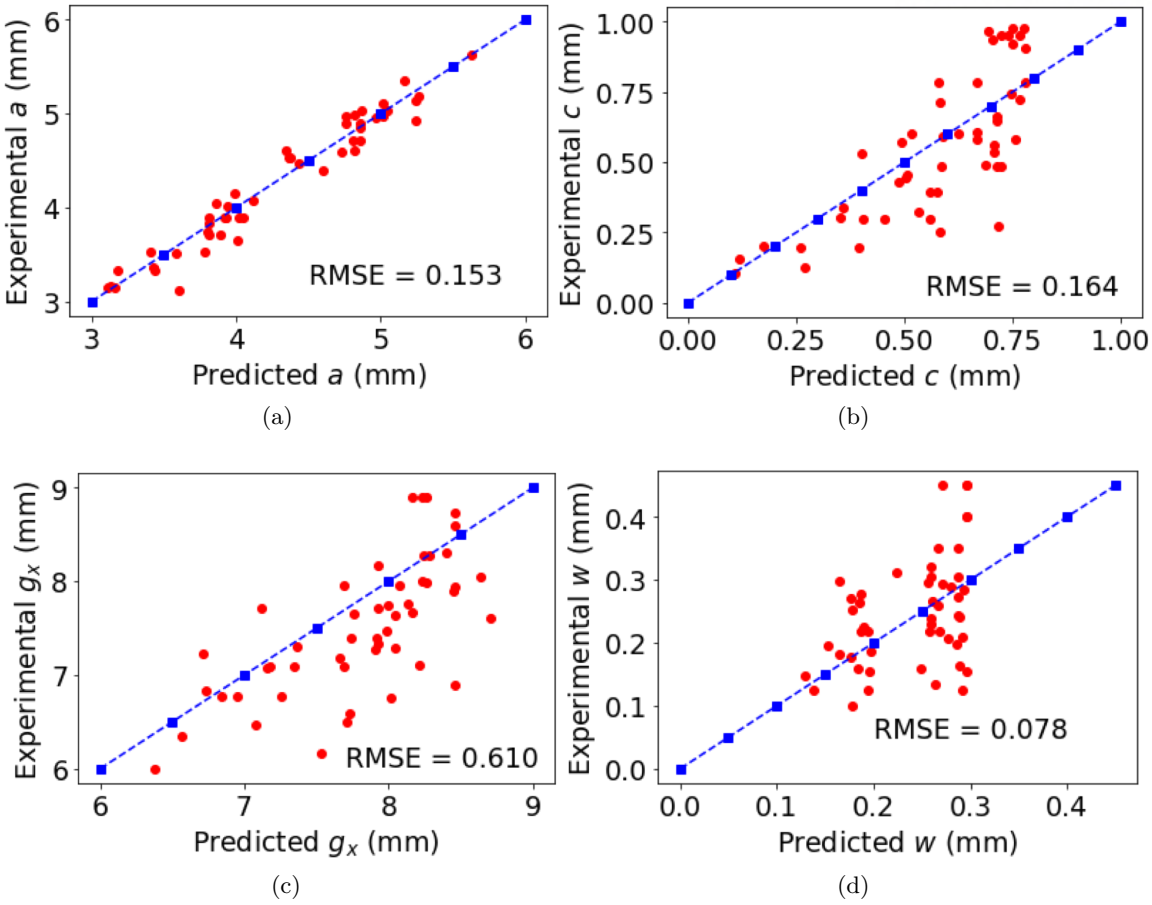

Figure 4.23: Experimental and predicted transmission spectra results of inverse design for $n \times n$ metamaterial prototype structure. (a) structure length a (b) gap width c (c) substrate length g_x (d) line thickness w.

$\epsilon_r \in [11, 17]$, $t_{Si} \in [200, 235], \mu m$, and $r_{dr} \in [90, 150], \mu m$, respectively. We train our model with 392 input samples of absorptance-characteristics and output geometry.

We have tested our Lifelong learning learning model on 50 unseen samples of data. We have validated our inverse design via scatter plots with root mean square error (RMSE) value in Fig. 4.26. Fig. 4.25 shows the histograms of the frequency-characteristics of absorptance. We plot our machine learning predicted parameters versus experimental parameters of substrate relative permittivity ϵ_r, dielectric thickness t_{Si}, drain radius r_{dr}, used in the corresponding simulation of channel and we compute the root mean square error as given in Fig. 4.26. The observed mismatch is majorly due to training of our model with less input samples of absorptance spectra and partly due to the estimated function being *non-injective*

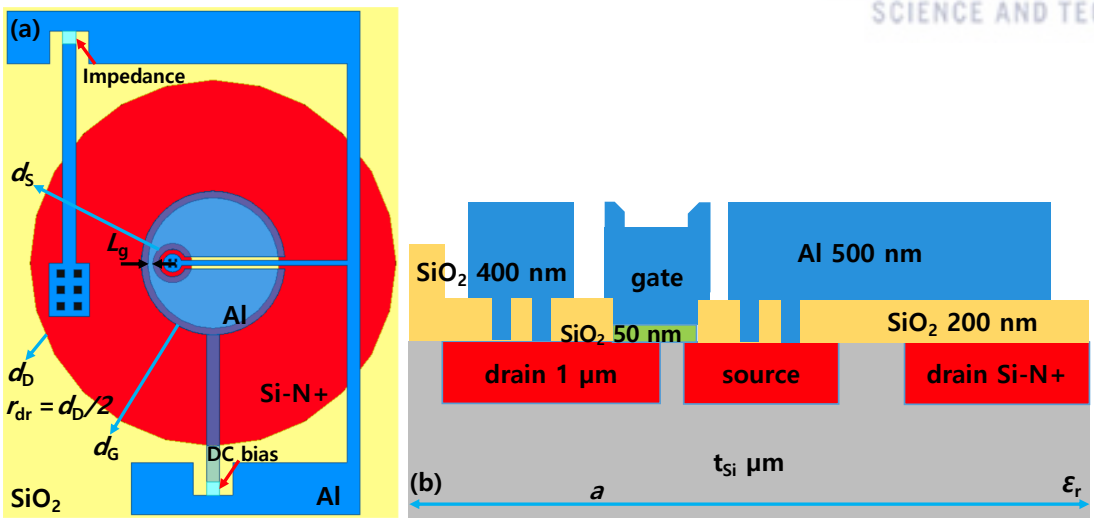

Figure 4.24: Unit cell transistor-antenna structure (a) Top view (b) Side view.

(different geometry parameter value configurations map to the same absorptance spectra). In future, we wish to train our model with more number of input dataset to improve root mean square error values.

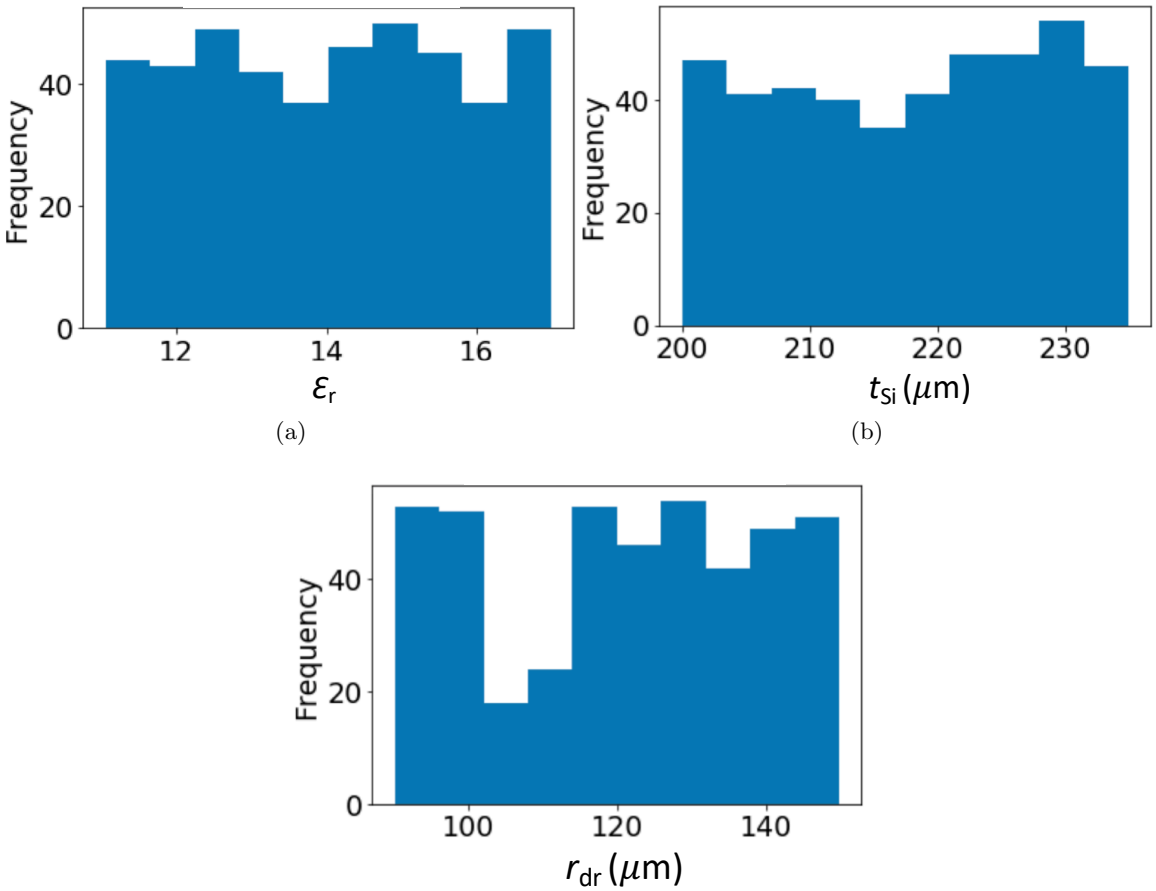

Figure 4.25: Histogram training geometry parameter plots of $n \times n$ transistor-antenna structure. (a) substrate relative permittivity ϵ_r (b) dielectric thickness t_{Si} (c) drain radius r_{dr}.

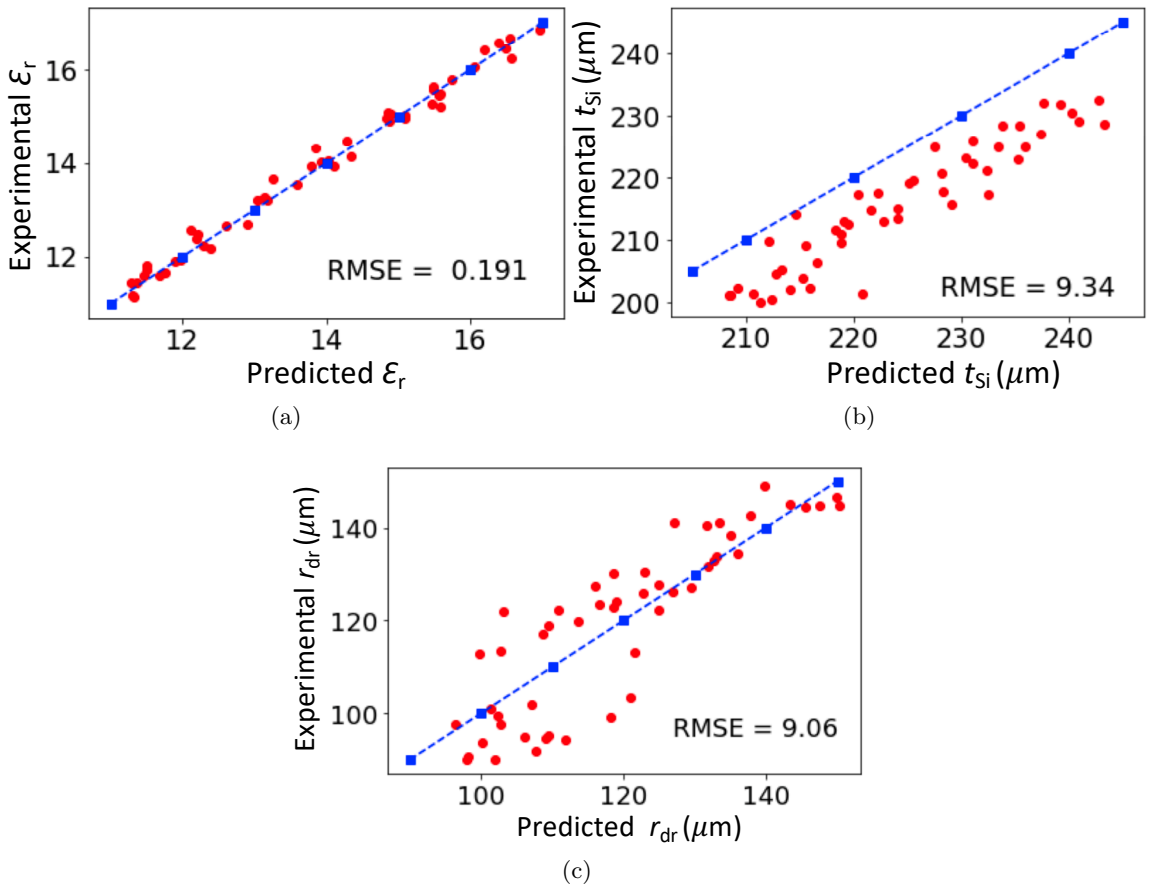

Figure 4.26: Experimental and predicted absorptance spectra results of inverse design for $n \times n$ transistor-antenna structure. (a) substrate relative permittivity ϵ_r (b) dielectric thickness t_{Si} (c) drain radius r_{dr}.

Chapter 5

Conclusion and future work

5.1 Conclusion

In first part of thesis, we presented the design and the verification of a novel monolithic circular patch antenna that utilizes the mmW characteristic of the ring-type asymmetric FET detector. Since the gate, drain, and source of the ring-type FET jointly behaves as a single monolithic patch, we can realize an integrated device without any interconnection between antenna and detector. To confirm the resonant frequency and the other design variables, a design procedure based on an approximate periodic bandgap model and parametric simulations has been established, focusing on the optimization of reflection and absorption characteristics. From the measurements of a fabricated device, we demonstrated the enhanced performances which are in comparable order with the reported results of state-of-the-art antenna integrated direct detectors. The improved performance of the proposed monolithic ring-type FET-based circular antenna pixel is expected to provide the possibility of a mega-pixel-level detector for large-scale real-time mmW imaging camera applications.

In second part of the thesis, we presented the generative and inverse design of metamaterial (MTM) electromagnetic structures through Bayesian Learning and Deep Learning respectively. For generative design of metamaterial structure, we propose a novel method of designing electromagnetic metamaterial structure, which usually consist of very large number of inhomogeneous micro structures, using bayesian clique learning (BCL). Our method constructs a new topological structure called statistical clique, that encodes EM informa-

tion, which reduces our search space by cutting down unnecessary data. We classify our data in three ranges and run our learning to find range specific parameters. Our learning algorithm is scalable, and works on any general electromagnetic structure for automated design. We have given a bound for the computational complexity of our method and discuss the trade off of the complexity with the uncertainty. The result of metamaterial prototype demonstrates that the proposed learning algorithm can facilitate the design of MTMs to a large extent with high accuracy. We also compared two EM structures dataset that has weakly linear negative correlation. Our BCL allows us to reuse learning parameters from trained EM dataset to new EM dataset with little modifications. While in another case, we have proposed an inverse design approach to find geometric parameters of EM structures from frequency characteristics. An advanced multi-task deep neural network is used to map the desired transmission or absorptance characteristics by obtaining the corresponding geometrical dimensions.

5.2 Future Work

5.2.1 Monolithic transistor-antenna design for real-time THz colour imaging

Until now, we experimentally demonstrate the concept of ring-type FET itself working as antenna. We verified the concept for 20×20 antenna pixels, but the actual power (P_a) impinging on unit cell pixel is very small for efficient real time imaging applications, therefore it is needed to work on 1000×1000 pixel design i.e. never-ever demonstrated on real time at room-temperature (based on Si). Apart from this, we wish to experimentally demonstrate multi-band frequency sensitivity antenna array design for simultaneously working in different frequency, due to incidence of THz wave at different active areas of same multi-pixel structure. The improved performance of the proposed frequency sensitive multi-band and multi-pixel structure is expected to provide the possibility of a mega-pixel-level detector for large-scale real-time THz colour imaging applications.

5.2.2 Inverse design for small dataset

In future, we intend to reduce the number of exploited transmission or absorptance characteristics, and provide all feasible combinatorial solutions for the desired frequency characteristics. We have achieved good results by training with transmission characteristics of the MTM structures; we plan to improve the inverse design so it only requires a small number of frequency characteristics parameters to provide the range of geometric parameters.

Bibliography

[1] Peter H. Siegel, "Terahertz technology," *IEEE Transactions on Microwave Theory and Techniques*, vol. 50, no. 3, pp. 910–928, 2002.

[2] S. Oka, H. Togo, N. Kukutsu, and T. Nagatsuma, "Latest Trends in Millimeter-Wave Imaging Technology," *Progress In Electromagnetics Research Letters*, vol. 1, pp. 197–204, Jan. 2008.

[3] Adrian Tang, Qun Jane Gu, and Mau-Chung Frank Chang, "CMOS Receivers for Active and Passive mm-Wave Imaging," *IEEE Communications Magazine*, vol. 49, no. 10, pp. 190–198, Oct. 2011.

[4] David M. Sheen, Douglas L. McMakin, and Thomas E. Hall, "Three-Dimensional Millimeter-Wave Imaging for Concealed Weapon Detection," *IEEE Transactions on Microwave Theory and Techniques*, vol. 49, no. 9, pp. 1581–1592, Sep. 2001.

[5] R. Appleby, and R. N. Anderson, "Millimeter-Wave and Submillimeter-Wave Imaging for Security and Surveillance," *Proceedings of the IEEE*, vol. 95, no. 8, pp. 1683–1690, Aug. 2007.

[6] B. Gonzales-Valdes et al., "Millimeter wave imaging architecture for on-the-move whole body imaging," *IEEE Transactions on Antennas and Propagation*, vol. 64, no. 6, pp. 2328–2338, Jun. 2016.

[7] R. Appleby, and H. B. Wallace, "Standoff Detection of Weapons and Contraband in the 100 GHz to 1 THz Region," *IEEE Transactions on Antennas and Propagation*, vol. 55, no. 11, pp. 2944–2956, Nov. 2007.

[8] I. V. Mikhelson et al., "Noncontact millimeter-wave real-time detection and tracking of heart rate on an ambulatory subject," *IEEE Transactions on Information Technology in Biomedicine*, vol. 16, no. 5, pp. 927–934, Sep. 2012.

[9] Nachappa (Sami) Gopalsami, and Apostolos (Paul) C. Raptis, "Millimeter-Wave Radar Sensing of Airborne Chemicals," *IEEE Transactions on Microwave Theory and Techniques*, vol. 49, no. 4, pp. 646–653, Apr. 2001.

[10] Charles L. Croskey et al., "The Millimeter Wave Atmospheric Sounder (MAS): A Shuttle-Based Remote Sensing Experiment," *IEEE Transactions on Microwave Theory and Techniques*, vol. 40, no. 6, pp. 1090–1100, Jun. 1992.

[11] Tyler C. Bowman, Magda El-Shenawee, and Lucas K. Campbell, "Terahertz Imaging of Excised Breast Tumor Tissue on Paraffin Sections," *IEEE Transactions on Antennas and Propagation*, vol. 63, no. 5, pp. 2088-2097, May. 2015.

[12] Michael J. Myers et al., "Antenna-Coupled Bolometers for Millimeter Waves," *IEEE Transactions on Applied Superconductivity*, vol. 15, no. 2, pp. 564–566, Jun. 2005.

[13] P. L. Richards, "Bolometers for Infrared and Millimeter Waves," *Journal of Applied Physics*, vol. 76, no. 1, pp. 1–24, Mar. 1994.

[14] Akram Hossain, and Muhammad H. Rashid, "Pyroelectric Detectors and Their Applications," *IEEE Transactions on Industry Applications*, vol. 27, no. 5, pp. 824–829, Sep. 1991.

[15] Douglas R. Denison et al., "Experimental characterization of mm-wave detection by a micro-array of Golay cells," *Proceedings of SPIE 7309, Passive Millimeter-Wave Imaging Technology XII*, 73090J, Apr. 2009.

[16] N. Nader Esfahani et al., "Millimeter-wave photoresponse due to excitation of two-dimensional plasmons in InGaAs/InP high-electron-mobility transistors," *Journal of Applied Physics*, vol. 114, no. 3, 033105, 2013.

[17] S. P. Voinigescu et al., "Silicon D-band wireless transceivers and applications," in 2010 Asia-Pacific Microwave Conference, Yokohama, Japan, 2010, pp. 1857-1864.

[18] E. Dacquay et al., "D-Band Total Power Radiometer Performance Optimization in an SiGe HBT Technology," *IEEE Transaction on Microwave Theory and Techniques*, vol. 60, no. 3, pp. 813-826, Mar. 2012.

[19] Kaushik Sengupta, Dongjin Seo, Lita Yang, and Ali Hajimiri, "Silicon Integrated 280 GHz Imaging Chipset with 44 SiGe Receiver Array and CMOS Source," *IEEE Transactions on Terahertz Science and Technology*, vol. 5, no. 3, pp. 427–437, May 2015.

[20] Marcel Andree, Janusz Grzyb, Ritesh Jain, Bernd Heinemann, and Ullrich R. Pfeiffer, "A Broadband Dual-Polarized Terahertz Direct Detector in a 0.13-μm SiGe HBT Technology," 2019 IEEE MTT-S International Microwave Symposium (IMS), Boston, MA, 2019, pp. 500–503.

[21] Janusz Grzyb, Marcel Andree, Ritesh Jain, Bernd Heinemann, and Ullrich R. Pfeiffer, "A Lens-Coupled On-Chip Antenna for Dual-Polarization SiGe HBT THz Direct Detector," *IEEE Antennas and Wireless Propagation Letters*, 2019 (Early Access).

[22] W. Knap et al., "Field Effect Transistors for Terahertz Detection: Physics and First Imaging Applications," *Journal of Infrared Millimeter Terahertz Waves*, 30, pp. 1319–1337, 2009.

[23] Richard Al Hadi et al., "A 1 k-pixel video camera for 0.7-1.1 terahertz imaging applications in 65-nm CMOS," *IEEE Journal of Solid-State Circuits*, vol. 47, no. 12, pp. 2999–3012, Dec 2012.

[24] Franz Schuster et al., "Broadband terahertz imaging with highly sensitive silicon CMOS detectors," *Optics Express*, vol. 19, no. 8, pp. 7827–7832, 2011.

[25] R. Han et al., "A 280-GHz Schottky diode detector in 130-nm digital CMOS," *IEEE Journal of Solid-State Circuits*, vol. 46, no. 11, pp. 2602–2612, Nov. 2011.

[26] R. Han et al., "Active terahertz imaging using Schottky diodes in CMOS: Array and 860-GHz pixel," *IEEE Journal of Solid-State Circuits*, vol. 48, no. 10, pp. 2296–2308, Oct. 2013.

[27] S. T. Nicolson et al., "A 1.2V, 140GHz receiver with on-die antenna in 65nm CMOS," in *2008 IEEE Radio Frequency Integrated Circuits Symposium*, Atlanta, GA, 2008, pp. 229–232.

[28] I. Sarkas, J. Hasch, A. Balteanu, and S. P. Voinigescu, "A Fundamental Frequency 120-GHz SiGe BiCMOS Distance Sensor With Integrated Antenna," *IEEE Transaction on Microwave Theory and Techniques*, vol. 60, no. 3, pp. 795–812, Mar. 2012.

[29] J. Grzyb et al., "Real-time video rate imaging with a 1k-pixel THz CMOS focal plane array," *Proc. of SPIE*, vol. 8362, 83620C-1, May 2012.

[30] J. Grzyb, and U. R. Pfeiffer, "THz Direct Detector and Heterodyne Receiver Arrays in Silicon Nanoscale Technologies," *J. Infrared Milli Terehz Waves*, vol. 36, pp. 998–1032, 2015.

[31] Dae Yeon Kim, Shinwoong Park, Ruonan Han, and Kenneth K. O., "Design and Demonstration of 820-GHz Array Using Diode-Connected NMOS Transistors in 130-nm CMOS for Active Imaging," *IEEE Transactions on Terahertz Science and Technology*, vol. 6, no. 2, pp. 306–317, Mar. 2016.

[32] Ritesh Jain, Robin Zatta, Janusz Grzyb, David Harame, and Ullrich R. Pfeiffer, "A Terahertz Direct Detector in 22nm FD-SOI CMOS," 2018 13th European Microwave Integrated Circuits Conference (EuMIC), Madrid, Spain, 2018, pp. 25–28.

[33] Mikhail Dyakonov, and Michael Shur, "Detection, Mixing, and Frequency Multiplication of Terahertz Radiation by Two-Dimensional Electronic Fluid," *IEEE Transactions on Electron Devices*, vol. 43, no. 3, pp. 380–387, Mar. 1996.

[34] V. Y. Kachorovskii, S. L. Rumyantsev, W. Knap, and M. Shur, "Performance limits for field effect transistors as terahertz detectors," *Applied Physics Letters*, vol. 102, no. 22, 223505 (2013).

[35] S.-P. Han et al., "Real-time continuous-wave terahertz line scanner based on a compact 1×240 InGaAs Schottky barrier diode array detector," *Optics Express*, vol. 22, no. 23, pp. 28977-28983, 2014.

[36] U. R. Pfeiffer and E. Ojefors, "A 600-GHz CMOS focal-plane array for terahertz imaging applications," in *Proc. 34th Eur. Solid-State Circuits Conf.*, Sep. 2008, pp. 110-114.

[37] G. C. Trichopoulos, L. Mosbacker, D. Burdette, and K. Sertel, "A Broadband Focal Plane Array Camera for Real-time THz Imaging Applications," *IEEE Transactions on Antennas and Propagation*, vol. 61, no. 4, pp. 1733–1740, Apr. 2013.

[38] D. B. Rutledge and M. S. Muha, "Imaging Antenna Arrays," *IEEE Transactions on Antennas and Propagation*, vol. 30, no. 4, pp. 535–540, Jul. 1982.

[39] E. Ojefors, U. R. Pfeiffer, A. Lisauskas, and H. G. Roskos, "A 0.65 THz Focal-Plane Array in a Quarter-Micron CMOS Process Technology," *IEEE Journal of Solid-State Circuits*, vol. 44, no. 7, pp. 1968–1976, July 2009.

[40] U. R. Pfeiffer, J. Grzyb, H. Sherry, A. Cathelin, and A. Kaiser, "Towards low-NEP room-temperature THz MOSFET direct detectors in CMOS technology," *Proc. 38th IRMMW-THz*, pp. 1–2, Sep. 2012.

[41] S. Nahar, A. Gutin, A. Muraviev, I. Wilke, M. Shur, and M. M. Hella, "Terahertz detection using on chip patch and dipole antenna-coupled GaAs high electron mobility transistors," in *IEEE MTT-S Int. Microw. Symp. Dig.*, Jun. 2014, pp. 1-4.

[42] M. Sakhno et al., "Modeling of the Substrate Influence on Multielement THz Detector Operation," *J. Infrared Milli Terahz Waves*, vol. 35, pp. 703–719, 2014.

[43] M. W. Ryu et al., "Performance enhancement of plasmonic sub-terahertz detector based on antenna integrated low-impedance silicon MOSFET," *IEEE Electron Device Letters*, vol. 36, no. 3, pp. 220–222, Mar. 2015.

[44] M. W. Ryu et al., "High-Performance Plasmonic THz Detector Based on Asymmetric FET With Vertically Integrated Antenna in CMOS Technology," *IEEE Transactions on Electron Devices*, vol. 63, no. 4, pp. 1742–1748, Apr. 2016.

[45] S. Boppel et al., "CMOS Integrated Antenna-Coupled Field-Effect Transistors for the Detection of Radiation From 0.2 to 4.3 THz," *IEEE Transactions on Microwave Theory and Techniques*, vol. 60, no. 12, pp. 3834–3843, Dec. 2012.

[46] Seungwan Chai et al., "THz Detector with an Antenna Coupled Stacked CMOS Plasma-Wave FET," *IEEE Microwave and Wireless Components Letters*, vol. 24, no. 12, pp. 869-871, Dec. 2014.

[47] M. Sakowicz Sakowicz "Polarization sensitive detection of 100 GHz radiation by high mobility field-effect transistors," *Journal of Applied Physics*, vol. 104, no. 2, 024519, May. 2008.

[48] Elham Mohammadi , Bahareh Behzadnezhad, and Nader Behdad,"An Angle-Sensing Infrared Detector Using a Two-Element Biomimetic Antenna Array," *IEEE Transactions on Antennas and Propagation*, pp. 1–8, 2018.

[49] Yan Li, Yong-Xin Guo, and Shaoqiu Xiao, "Orientation Insensitive Antenna With Polarization Diversity for Wireless Capsule Endoscope System," *IEEE Transactions on Antennas and Propagation*, vol. 65, no. 7, pp. 3738–3743, July 2017.

[50] Peter M. Krenz et al., "Response Increase of IR Antenna-Coupled Thermocouple Using Impedance Matching," *IEEE Journal of Quantum Electronics*, vol. 48, no. 5, pp. 659–664, 2012.

[51] A. Deutsch et al., "Frequency-Dependent Losses on High-Performance Interconnections," *IEEE Transactions on Electromagnetic Compatibility*, vol. 43, no. 4, pp. 446–465, Nov. 2001.

[52] Ofer Markish and Yehuda Leviatan, "Analysis and Optimization of Terahertz Bolometer Antennas," *IEEE Transactions on Antennas and Propagation*, vol. 64, no. 8, pp. 3302–3309, Aug. 2016.

[53] Mahmoud Nikoufard, Abbas Nourmohammadi, and Saeid Esmaeili, "Hybrid Plasmonic Nanoantenna With the Capability of Monolithic Integration With Laser and

Photodetector on InP Substrate," *IEEE Transactions on Antennas and Propagation*, vol. 66, no. 1, pp. 3–8, Jan. 2018.

[54] Y. P. Zhang and D. Liu, "Antenna-on-chip and antenna-in-package solutions to highly integrated millimeter-wave devices for wireless communications," *IEEE Transactions on Antennas and Propagation*, vol. 57, no. 10, pp. 2830–2841, Oct. 2009.

[55] J. Mou, Q. Xue, D. Guo, and X. Lv, "A THz Detector Chip With Printed Circular Cavity as Package and Enhancement of Antenna Gain," *IEEE Transactions on Antennas and Propagation*, vol. 64, no. 4, pp. 1242–1249, April 2016.

[56] T.-W. Koo, Y.-J. Hong, G.-K. Park, K. Shin, and J.-G. Yook, "Extremely Low-Profile Antenna for Attachable Bio-Sensors," *IEEE Transactions on Antennas and Propagation*, vol. 63, no. 4, pp. 1537–1545, April 2015.

[57] K. Topalli, G. C. Trichopoulos, and K. Sertel "An Indirect Impedance Characterization Method for Monolithic THz Antennas Using Coplanar Probe Measurements," *IEEE Antennas and Wireless Propagation Letters*, vol. 11, pp. 3–5, 2012.

[58] G. Gentile et al., "Silicon-Filled Rectangular Waveguides and Frequency Scanning Antennas for mm-Wave Integrated Systems," *IEEE Transactions on Antennas and Propagation*, vol. 61, no. 12, pp. 5893–5901, Dec. 2013.

[59] Y. P. Zhang et al.,"Antenna-in-Package Design for Wirebond Interconnection to Highly Integrated 60-GHz Radios," *IEEE Transactions on Antennas and Propagation*, vol. 57, no. 10, pp. 2842–2852, Oct. 2009.

[60] M. W. Ryu et al., "Trantenna: monolithic transistor-antenna device for real-time THz imaging system," Proc. 2017 Symposium on VLSI Technology, pp. T146–T147, Kyoto, Japan, Jun. 2017.

[61] W. Knap et al., "Plasma wave detection of sub-terahertz and terahertz radiation by silicon field-effect transistors," *Applied Physics Letters* vol. 85, no. 4, pp. 675–677, May. 2004.

[62] R. Tauk et al., "Plasma wave detection of terahertz radiation by silicon field effect transistors: Responsivity and noise equivalent power," *Applied Physics Letters*, vol. 89, no. 25, 253511, 2006.

[63] E. I. Smirnovaet et al., "Simulation of photonic band gaps in metal rod lattices for microwave applications," *Journal of Applied Physics*, vol. 91, no. 3, pp. 960-968, 2002.

[64] Constantine A. Balanis, *Antenna Theory: Analysis and Design*, A John Willey & Sons, INC., Publication, 2005.

[65] Constantine A. Balanis, *Advanced Engineering Electromagnetics*, A John Willey & Sons, INC., Publication, 2012.

[66] Dominique Coquillat et al., "Improvement of terahertz field effect transistor detectors by substrate thinning and radiation losses reduction," *Optics Express*, vol. 24, no. 1, pp. 272–281, Jan. 2016.

[67] Paul F. Goldsmith, *Quasioptical Systems: Gaussian Beam Quasioptical Propagation and Applications*, Wiley-IEEE Press, pp. 9–25, 1998.

[68] *HFSS Ver. 16.2*, Ansys, Inc., Canonsburg, PA, USA, 2015.

[69] M. W. Ryu et al., "Photoresponse enhancement of plasmonic terahertz wave detector based on asymmetric silicon MOSFETs with antenna integration," *Japanese Journal of Applied Physics*, vol. 53, 04EJ05 (2014).

[70] M. Bauer et al., "Antenna-coupled field-effect transistors for multi-spectral terahertz imaging up to 4.25 THz," *Optics Express*, vol. 22, no. 16, pp. 19235–19241 (2014).

[71] D. Schuriga et. al, "Electric-field-coupled resonators for negative permittivity metamaterials," *Appl. Phys. Lett.*, vol. 88, no. 4, Jan. 2006.

[72] C. Gianfagna et. al, "Enabling Antenna Design with Nano-Magnetic Materials using Machine Learning," *IEEE Nanotech. Mat. Device. Conf.*, Sep. 2015.

[73] S. J. Park et. al, "Preliminary application of machine-learning techniques for thermal-electrical parameter optimization in 3-D IC," *IEEE Int'l Symp. Electromagn. Compati.*, pp. 402-405, Jul. 2016.

[74] Z. Szabo et. al, "A Unique Extraction of Metamaterial Parameters Based on Kramers-Kronig Relationship," *IEEE Trans. Microw. Theory Tech.*, vol. 58, no. 10, pp. 2646-2653, Oct. 2010.

[75] Afra Zomorodian et. al, "Computing Persistent Homology," *Discrete Comput. Geom.*, vol. 33, pp. 249-274, Feb. 2005.

[76] Michael W. Reimann et. al, "Cliques of Neurons Bound into Cavities Provide a Missing Link between Structure and Function," *Front. Comput. Neurosci.*, vol. 11:48, pp. 1-16, Jun. 2017.

[77] Petri G. et. al, "Topological Strata of Weighted Complex Networks," *PLoS ONE* 8(6): e66506, 2013.

[78] Edgar Lobaton et. al, "A Distributed Topological Camera Network Representation for Tracking Applications" *IEEE Trans. Imag. Process.*, vol. 19, no. 10, pp. 2516-2529, Oct. 2010.

[79] Robert Ghrist, "Barcodes: The Persistent Topology of Data," *Bull. Amer. Math. Soc.*, vol. 45, pp. 61-75, 2008.

[80] Cetin Savkli et. al, "Bayesian Learning of Clique Tree Structure," arXiv:1708.07025v1 [cs.LG], Aug. 2017.

[81] Alistair P. Duffy et. al, "Objective Selection of Minimum Acceptable Mesh Refinement for EMC Simulations," *IEEE Trans. Electromagn. Compati.*, vol. 57, no. 5, pp. 1266-1269, Oct. 2015.

[82] Ihor Farmaga et. al, "Evaluation of Computational Complexity of Finite Element Analysis," *IEEE Int. Conf. on CADSM*, pp. 213-214, Feb. 2011.

[83] Larry J. Segerlind, "Applied Finite Element Analysis," *A John Willey & Sons, INC., Publication*, 1984.

[84] Kallol Roy, Hakki Torun Mert, and Madhavan Swaminathan, "Preliminary Application of Deep Learning to Design Space Exploration," 2018 IEEE Electrical Design of Advanced Packaging and Systems Symposium (EDAPS), pp. 1–2, Chandigarh, India, Dec. 2018.

[85] Kallol Roy, Majid Ahadi Dolastara, Hakki Mert Torun, Riccardo Trichero, and Madhavan Swaminathan, "Inverse Design of Transmission Lines with Deep Learning," 2019 IEEE Conference on Electrical Performance of Electronic Packaging and Systems (EPEPS), Montreal, Canada, Oct. 2019.

[86] R. Trinchero, M. Ahadi Dolatsara, K. Roy, M. Swaminathan, and F. G. Canavero, 2019 IEEE Electrical Design of Advanced Packaging and Systems Symposium (EDAPS), Kaohsiung, Taiwan, Dec. 2019.

[87] Tom M. Mitchell, and Sebastian B. Thrun, "Explanation-Based Neural Network Learning for Robot Control," *Advances in Neural Information Processing Systems*, vol. 5, pp. 287–294, Morgan Kaufmann, San Mateo, CA, 1992.

[88] Housen Li, Johannes Schwab, Stephan Antholzer, and Markus Haltmeier, "NETT: Solving Inverse Problems with Deep Neural Networks," arXiv:1803.00092v2, Jul. 2019.

[89] Zhaocheng Liu, Dayu Zhu, Sean P. Rodrigues, Kyu-Tae Lee, and Wenshan Cai, "Generative Model for Inverse Design of Metamaterials," *Nano Lett.*, vol. 18, no. 10, pp. 6570–6576, Sep. 2018.

[90] Jaweria Amjad, Zhaoyan Lyu, and Miguel R. D. Rodrigues, "Deep Learning for Inverse Problems: Bounds and Regularizers," arXiv:1901.11352v1 [cs.LG], Jan. 2019.

[91] Andrew Carlson et. al, "Toward an Architecture for Never-Ending Language Learning," Proceedings of the Twenty-Fourth AAAI Conference on Artificial Intelligence (AAAI-10), pp. 1306–1313, Atlanta, Georgia, Jul. 2010.

List of publications

2019 **Ramesh Patel**, Kallol Roy, Kyung-rok Kim, and Ki Jin Han, "Inverse Design of Metasurfaces through Deep Learning," in preparation for submission in IEEE Access, 2020.

2019 **Ramesh Patel**, Min Woo Ryu, Mun Seok Choe, Eunmi Choi, Kyung Rok Kim, and Ki Jin Han, "Monolithic Circular Transistor-Antenna Design for High Performance Plasmonic Millimeter-Wave Detectors," IEEE Transactions on Antennas and Propagation, pp. 1-1, 2019 (Early access).
(Media coverage by School of ECE, UNIST).

2019 Min Woo Ryu, E-San Jang, Sang Hyo Ahn, Jong Yul Park, **Ramesh Patel**, and Kyung Rok Kim, "High Uniformity of THz Detectors Based on Monolithic Trantenna for Multi-Pixel Array THz Imaging system," 27th Korean Conference on Semiconductors, Daejeon, South Korea (submitted).

2019 E-San Jang, M. W. Ryu, **R. Patel**, S. H. Ahn, H. J. Jeon, K. J. Han, and K. R. Kim, "Record-High Performance Trantenna based on Asymmetric Nano-Ring FET for Polarization-Independent Large-Scale/Real-Time THz Imaging," 2019 IEEE Symposium on VLSI Technology and Circuits, Kyoto, Japan, 2019, pp. T160-T161.
(Media coverage by School of ECE, UNIST).

2019 E-San Jang, **Ramesh Patel**, Sang Hyo Ahn, Hyeong Ju Jeon, "Monolithic active trantenna based on CMOS technology for ultimate high-performance terahertz wave detector," 25th Samsung Humantech Paper Award: Physical Device & Processes, Suwon, Korea, Feb. 2019.
(Won Silver Prize).

2018 **Ramesh Patel**, Kallol Roy, Jaesik Choi, Ki Jin Han, "Generative Design of Electromagnetic Structures through Bayesian Learning," IEEE Transactions on Magnetics, vol. 54, no. 3, Mar 2018.

2017 M. W. Ryu, **R. Patel**, S. H. Ahn, H. J. Jeon, M. S. Choe, E. Choi, K. J. Han, and K. R. Kim, "Trantenna: Monolithic transistor-antenna device for real-time THz imaging system," 2017 IEEE Symposium on VLSI Technology, Kyoto, Japan, 2017, pp. T146-T147.

(Media coverage by School of ECE, UNIST).

2017 Min Woo Ryu, **Ramesh Patel**, Esan Jang, Sang Hyo Ahn, Hyeong Ju Jeon, Mun Seok Choe, EunMi Choi, Ki Jin Han, and Kyung Rok Kim, "Highly-Sensitive Plasmonic Nano-Ring Transistor for Monolithic Terahertz Active Antenna," 2017 IEEE International Conference on Nanotechnology, Pittsburgh, USA, 2017, pp. 17-21.

(Finalist of Best Paper Award).

2017 **Ramesh Patel**, Kallol Roy, Jaesik Choi, Ki Jin Han, "Tractable Bayesian Learning for Automated Design of Electromagnetic Structures," 21st IEEE International Conference on the Computation of Electromagnetic Fields (Compumag2017), June 18-22, 2017, Daejeon, South Korea.

2016 **Ramesh Patel**, Franklin Bien, and Ki Jin Han, "A Modified Square Koch Curve Fractal Stent Antenna Design for Medical Implants," 2016 URSI Asia-Pacific Radio Science Conference (URSI AP-RASC), Seoul, South Korea, 2016, pp. 1628-1631.

2015 **Ramesh Patel**, and Ki Jin Han, "Utilization of higher-mode resonance in broadening the E-plane HPBW of printed antenna for Automotive Radar Application," 2015 IEEE International Workshop on Antenna Technology (iWAT), Seoul, South Korea, 2015, pp. 330-332.

2014 **Ramesh Patel**, and Ki Jin Han, "Broad E-plane HPBW using Mode Matching Technique for Automotive Radar Application," 2014 Korea-Japan Microwave Workshop (KJMW), Suwon, South Korea, 2014.